UNIVERSITY OF STRATHCLYDE

DEPARTMENT OF NAVAL ARCHITECTURE, OCEAN, AND MARINE ENGINEERING

Experimental and Numerical Analysis of a Falling Plate

A THESIS

SUBMITTED IN PARTIAL FULFILLMENT OF THE REQUIREMENTS FOR THE AWARD OF DEGREE

OF

DOCTOR OF PHILOSOPHY

IN

NAVAL ARCHITECTURE, OCEAN, AND MARINE ENGINEERING

Submitted by **MOHAMMED BABA SHEHU**

201659762

Under the supervision of

DR. ZHIMING YUAN

DR. LAIBING JIA

August, 2022

DEPARTMENT OF NAVAL ARCHITECTURE, OCEAN, AND MARINE ENGINEERING
UNIVERSITY OF STRATHCLYDE

CANDIDATE'S DECLARATION

This thesis is the result of the author's original research. It has been composed by the author and has not been previously submitted for examination which has led to the award of a degree. The copyright belongs to the author under the terms of the United Kingdom Copyright Acts as qualified by University of Strathclyde Regulation 3.50. Due acknowledgement must always be made of the use of any material contained in, or derived from, this thesis.

Signed: Date:

DEPARTMENT OF NAVAL ARCHITECTURE, OCEAN, AND MARINE ENGINEERING
UNIVERSITY OF STRATHCLYDE

CERTIFICATE

I hereby certify that the thesis titled "**Experimental and Numerical Analysis of a Falling Plate**" which is submitted by **Mohammed Baba Shehu**, Registration No's – **201659762**, **Department of Naval Architecture, Ocean, and Marine Engineering** , University of Strathclyde, UK in partial fulfilment of the requirement for the award of the degree of Doctor of Philosophy, is a record of the PhD work carried out by the students under my supervision. To the best of my knowledge this work has not been submitted in part or full for any Degree or Diploma to this University or elsewhere.

Supervisor Name: Dr. Zhiming Yuan

Date:

Signed:

Co-Supervisor Name: Dr. Laibing Jia

Date:

Signed:

DEPARTMENT OF NAVAL ARCHITECTURE, OCEAN, AND MARINE ENGINEERING
UNIVERSITY OF STRATHCLYDE

ACKNOWLEDGEMENT

I would like to express my deepest appreciation and thanks to almighty Allah and my late parents, my lovely wife and kids for their overwhelming support, advice, patience, commitment, and encouragement right from the start until the very end of my research at University of Strathclyde.

I also wish to appreciate and thank my first supervisor Dr Zhiming Yuan for his continuous guidance and encouragement from the beginning of my research to the end, special acknowledgement also goes to my second supervisor Dr. Lai Bing Jia for his valuable guidance, assistance, and cooperation without both your efforts any progress and improvement during the research would not have been achieved.

My special appreciation to Prof. Sandy Day and warm thanks to the lab technicians at Kelvin Hydrodynamic Laboratory for their guidance, assistance, and cooperation during my PhD experimental setup. I wish to extend my gratitude to my fellow postgraduate colleagues, Dr Momchil Terziev for the collaborative work on the uncertainty measurement research, Guangwei Zhao for his support in the lab and Marvin Wright, Salisu Uba, Yakubu Galadima, Abdullahi Daya, and Dr Jamila Audu for their words of encouragements and support.

I would like to express my heartfelt thanks to Petroleum Technology Development Fund for sponsoring both my Master's and PhD at University of Strathclyde.

Finally, I wish to sincerely thank my wife for her unconditional love, support, friendship, encouragement, motivation, understanding and patience throughout this journey.

Abstract

The study of the motion of solids in fluids has always triggered interest in the scientific and research communities. This rich, dynamic behaviour dates back to the foundations of modern mechanics. However, understanding the dynamic behaviour of falling or rising objects in a viscous fluid under the effects of gravity, buoyancy, and the hydrodynamic/aerodynamic force in the fluid has long been a major issue in both the engineering and scientific communities.

This research is subdivided into three categories: firstly, an experimental investigation of heavy plates freely falling in three-dimensional *(3D)* space by determining the transition between zigzag and tumbling. Secondly, the determination of numerical uncertainty and, finally, investigating the dynamics of a free-falling plate with initial speeds.

In the first part, the free-falling of heavy plates both in air and water was investigated experimentally to determine the transition from zigzag to tumbling motions with different ranges of Re and I^*, a state-of-the-art technique is used to reduce the errors and inaccuracies during measurements, where the motion of the falling trajectories is calculated in *3D* space using Qualisys. The *3D* falling kinematics of the rectangular plate during descent were quantified by tracking the real-time centre of mass on the body during descent and measuring trajectories, speed, and azimuthal rotation. In the same way, the mapping of heavy plates was expanded to learn more about how they fall with bistability. It was concluded that the motion is similar to the three-dimensional dynamics of freely-falling bubbles with erratically wobbling behaviour and zigzag motion, but the motion changes with different oscillations of both vertical and horizontal velocity depending on the initial angle of release, but the vertical velocity is stochastic and does not depend on the initial release angle. As the Re increases, the frequency and pattern of oscillation increase with a decrease in aspect ratio and a high lift compared to previous literature.

The second part investigated the tumbling motion of a freely falling plate numerically, where the measured trajectory and forces were validated using both the experimental and numerical data available in previous literature. Using the grid convergence index method, the numerical uncertainty of the plate in free fall is calculated at each point during the free fall. The numerical results adopted in this study provided realistic results of tumbling plate dynamics and correctly predicted the trajectories, forces, and torque but with phase shifts.

The third part investigates the dynamic motion of a tumbling plate with different initial speeds. All previous experimental and computational investigations of freely falling plates, such as the influence of aspect ratio, density ratio, turbulence, Reynolds number, or the aerodynamics of multiple free-falling plates, and shape optimization, were carried out. The freely falling plate with initial speed was never explored. In the last part, the effect of initial speed on the tumbling motion of the body under the influence of gravity, including the falling paths, speeds, and forces, was studied numerically for the first time. Thus, it was observed that trajectories move to the left or right with different initial speeds, but the movement is stochastic and not dependent on initial speed. It was also observed that the measured horizontal velocity is different as the oscillation moves to the left or right with the same vertical velocity. The phase movement to the left looks similar to the double period motion in previous literature, while the phase movement to the right is a single periodic tumbling. Furthermore, a new triple period oscillation was observed and reported for the first time with a high frequency and low decent angle, horizontal, and vertical velocities.

Contents

List of Tables

List of Figures

List of Symbols

$6D$	Six-Dimensional
$3D$	Three-Dimensional
$2D$	Two-Dimensional
Re	Reynolds Number
I^*	Non-Dimensional Moment of Inertia
CFD	Computational Fluid Dynamics
$DFBI$	Dynamic Fluid Body Interaction
CF	Correction Factor
$FSRE$	Factors of Safety for Richardson Extrapolation
GCI	Grid Convergence Index
RE	Richardson Extrapolation
PIV	Particle Image Velocimetry
Fr	Froude Number
e^*	Eccentricity
IBM	Immersed Boundary Methods
DLM	Distributed Lanrangian Methods
DNS	Direct Numerical Simulations
AMI	Arbitrary Mesh Interface
$RANS$	Reynolds Averaged Navier-Stokes
RBD	Rigid Body Dynamic
G^*	Galileo Number
QTM	Qualisys Track Manager
θ	Roll in *degrees*
ϕ	Pitch in *degrees*
ϑ	Yaw in *degrees*
X, Y, Z	Global Coordinate Systems
x, y, z	Local Coordinate Systems
m	Mass in g
F	Force
u	Velocity
t	Time
M	Moment
ω	Angular Velocity
FSI	Fluid Solid Interaction
$\rho_{\mathbf{f}}$	Fluid Density
$\rho_{\mathbf{s}}$	Solid Density
p	Static Pressure
v	Kinematic Viscosity

CFL	Courant-Friedrichs-Lewy
U	Mesh Flow Speed
$PDEs$	Partial Differential Equations
w	Span Length
c	Chord Length
h	Thickness
ν	Kinematic Viscosity
g	Acceleration Due to Gravity
β^*	Thickness Ratio
γ^*	Aspect Ratio
ϵ^*	Density Ratio
V^*	Non-Dimensional Velocity
ϕ	Descent Angle
$\bar{V}$	Average Translating Velocity
$\bar{\omega}$	Average Angular Velocity
$_{\mathbf{T}}$	Terminal Falling Velocity
$Re_{\mathbf{T}}$	Terminal Reynolds Velocity
T^*	Non-Dimensional Time
X^*	Non-Dimensional X coordinate
Y^*	Non-Dimensional Y coordinate
F^*	Non-Dimensional Force
T^*	Non-Dimensional Torque
M^*	Non-Dimensional Mass
l	Length
$C_{\mathbf{L}}$	Drag Coefficient
$C_{\mathbf{D}}$	Lift Coefficient
$C_{\mathbf{M}}$	Moment coefficient
$f_{\mathbf{ex}}$	Exact or Extrapolated Solution
$f_{\mathbf{1}}$	Fine Mesh solution
$f_{\mathbf{2}}$	Medium Mesh Solution
$f_{\mathbf{3}}$	Coarse Mesh Solution
$p_{\mathbf{f}}$	Formal Order of Accuracy
p	Observed Order of Accuracy
$h_{\mathbf{s}}$	Grid Size
$U_{\mathbf{GCI}}$	Uncertainty According to the Grid Convergence Method
$U_{\mathbf{CF}}$	Uncertainty According to the Correction Method
FS	Factor of Safety
s	Sample Standard Deviation
$\bar{x}$	Sample Mean
n	Number of Sample

Chapter 1

INTRODUCTION

This chapter will provide a brief overview of the issues of freely falling, free rising, and fixed plate autorotation and the topic this thesis aims to address. In addition, the research aims and objectives with regard to research gaps and novelty will be discussed in detail. Finally, the thesis structure will be described.

1.1 Background

The rich dynamics and origins of non-straight paths of free-falling (Andersen et al. (2005a,b); Wang et al. (2013); Vincent et al. (2016); Lau et al. (2018)), free rising (Fernandes et al. (2007); Zenit and Magnaudet (2008); Horowitz and Williamson (2010)), or fixed and free autorotating body (Smith (1971); Iversen (1979); Lugt (1980); Mittal et al. (2004)) through a viscous liquid have always piqued the scientific and research community's interest. The final motion is as a result of complicated natural phenomena that exhibit complex dynamics. This topic has many similarities with winged-seed dispersal (Var (2011)), meteorology (Augspurger (1986)), particle sedimentation (Allen (1984)), insect flapping flight (Wang (2004)), autorotation phenomena (Iversen (1979); Lugt (1983)), windborne-debris flight (Baker (2007)), Deepsea installation (Fernandes et al. (2011)), and freely falling or rising motion of other objects in quiescent fluids (Zenit and Magnaudet (2008); Ern et al. (2011); Filella et al. (2015); Zhou et al. (2017)). This rich, dynamic behaviour dates back to the foundation of modern mechanics, which honoured great scientists such as Sir Isaac Newton, Albert Einstein, Galileo Galilei, James Clerk Maxwell, Gustav

Kirchhoff, and others.

The study of the motion of solids in fluids was first studied by Sir Isaac Newton in 1726. In his novel publication in the same year, he proposed the classical law of motion, the law of universal gravitation, and Kepler's laws of planetary motion from his mathematical description of gravity, and then used the same principles to account for the trajectories of cornets, tides, the precession of equinoxes, and other classical phenomena. He also described many experimental works on the motion of solids in fluids, such as the measurement of the resistance of a ship and the release of hog bladders from the top of the cupola of St. Paul's church in London. He noticed that the bladders did not always fall straight down but instead flutter in the air. Also, James Maxwell, a famous Scottish scientist in 1853, pointed out that when a slip of paper is released in the air, its motion, although undecided and wavering at first, sometimes becomes regular; its general path is not in a vertical direction but inclined to it at an angle which remains nearly constant; and its fluttering appearance will be found to be due to a rapid rotation around a horizontal axis. The direction of deviation from the vertical depends on the direction of rotation. He attributed the effect to some accidental peculiarities in the form of paper, but with a few experiments on a rectangular slip of paper two inches long and one wide, the direction of rotation is determined not by the irregularities of the paper but by the initial circumstances of the projection and symmetry of the paper slip, which significantly increases the distinctness of the phenomenon. Kirchhoff (1869) theoretically considered the motion of a solid body in an inviscid fluid and demonstrated that a renormalized added mass tensor can quantify the inertial interaction of the liquid with the moving solid and that a set of ordinary differential equations can describe the motion of the body. In 1964, Willmarth et al. (1964) were the first to visualise the motion of a freely falling plate. Using the non-dimensional moment of inertia and Reynolds number, they set out a benchmark for the mapping of flight regimes. Smith (1971) investigated the trajectory modes of freely falling discs and plates experimentally and found that different regimes can distinguish the trajec-

tory. After that, a considerable amount of research studies was carried out. The majority of studies attempt to predict a falling object's trajectory modes as well as the transition between them (Field et al. (1997); Belmonte et al. (1998); Andersen et al. (2005a); Lee et al. (2013); Lau et al. (2018); Esteban et al. (2020); Zhou et al. (2021)).

Understanding the dynamic behaviour of falling or rising objects in a viscous fluid under the effect of acceleration due to gravity, buoyancy, and the hydrodynamic force in the fluid has been a major issue in both engineering and scientific communities for centuries. A thin circular disc or rectangular flat plate, for example, determined by the non-dimensional moment of inertia I^* and the Reynolds number Re, can fall in a variety of ways, including steadily, planar fluttering (zigzag), tumbling, spiraling, and chaotic. Phase maps on which regimes for different falling styles are divided have been built in some studies, as shown in Figure 1.1.

In summary, the trajectories of freely falling plates can be stable or unstable. The stable trajectory corresponds to vertically falling, while the unstable trajectory includes fluttering, tumbling, and chaotic motion. The dynamic behaviour of falling plates as a function of two parameters, I^* (dimensionless moment of inertia) and Re (Reynolds number), as seen in Figure 1.1, shows that at $Re < 10^2$ plates will typically fall steadily without any dominant secondary motion. However, when Re is increased, the plates will either have side-to-side oscillating motion or tumbling motion depending on the moment of inertia. The dashed lines represent the bifurcation between the different motion classifications; the boundary between the periodic oscillating motion regime and the tumbling motion regime is approximately constant at $I^* = 0.2$ for $Re < 10^3$.

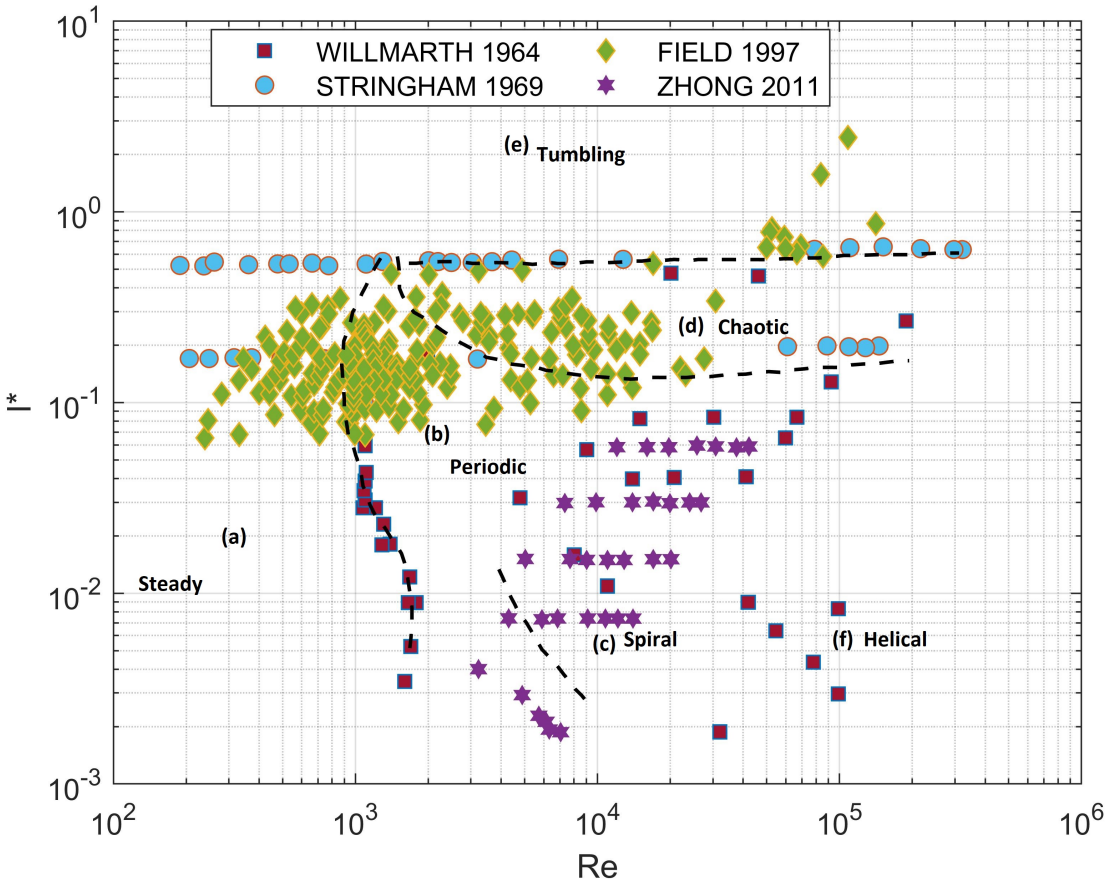

Figure 1.1: Phase diagram showing the dynamical behaviour of falling object as a function of the two parameters Re (Reynolds number) and I^* (dimensionless moment of inertia) (Lee et al. (2013))

.

1.2 Research Aims and Objectives

The free-falling of heavy plates in both air and water is investigated in this thesis by determining the transition from zigzag to tumbling motions and extending the mapping of descent with different Re and I^* ranges. Furthermore, validation of a thin rectangular plate freely falling in viscous fluid from previous literature is carried out using commercial software STAR-CCM+ to determine the effect of initial speed on the motion of the tumbling plate, and the uncertainty of the numerical measurement is analysed. This research work pursues the following objectives:

- Using the state-of-the-art techniques, the transitions from zigzag to tumbling motions of freely falling heavy plates in three-dimensional viscous fluid at the range of Reynolds number *270* to *23000*, dimensionless moment of inertia up to *23*, and aspect ratio *5-39* will be investigated experimentally, by extending the mapping of heavy plates from previous literature of Lau et al. (2018) to better understand the falling trajectories and bistability.

- Develop a numerical model to investigate the *2D/3D* motion of a falling plate by using *CFD* techniques to validate the experimental model of (Andersen et al. (2005a)) and numerical model of (Jin and Xu (2008)); and estimate the numerical uncertainty and errors of tumbling rectangular plate during free-fall.

- Develop a numerical model to investigate the motion of a free-falling plate numerically with an initial velocity.

1.3 Research Gap and Novelty

Several experimental and numerical studies using free-falling thin objects have been conducted over the last decades to establish that the transition from falling to flight are related to a variety of different plate densities and fluid viscosities (Auguste et al. (2013); Wang et al. (2013); Lau et al. (2018)). Different studies focused on recording the trajectories and determining the free-falling and freely rising body positions using high-speed digital video and PIV (Andersen et al. (2005a); Fernandes et al. (2007); Lee et al. (2013); Esteban et al. (2020)). Advances in experimental approaches have enabled the visual tracking of a moving object using digital cameras in recent years. Knowledge of the position and orientation's time history provides vital information on body movement, such as the instantaneous forces, velocities, and torques experienced by the falling or rising body. However, at high Reynolds numbers, it is critical to quantify the quasi-three-dimensional motion of a falling body because the rotation due to revolution can be considerable as the body rapidly moves back and forth due to the Magnus effect (Zhong et al. (2011)). In this research,

the motion of a freely falling heavy rectangular plate was investigated experimentally and determined the transition between zigzag falling and tumbling with a range of Reynolds numbers from *270* to *23000*, a dimensionless moment of inertia up to *23*, and an aspect ratio of *5-39*, to further understand the dependence of the initial angle of release on the bistability of the plate, the phase portraits of the mapped region across different regimes of I^* and Re at different aspect ratios were extended. Furthermore, errors and inaccuracies during measurement are reduced by capturing the motion of the freely falling trajectories in *3D* space, and the centre of mass is acquired at constant intervals by tracking the makers on the body during descent in real-time. The rectangular plate's three-dimensional *(3D)* falling kinematics were measured to calculate its speed, azimuthal rotation, and paths as it falls.

Furthermore, it is apparent that the dynamics of falling bodies have been studied using direct numerical simulation in a number of studies (Pan et al. (2002); Auguste et al. (2013); Wu and Lin (2015); Zorzi et al. (2015)), but mesh sensitivity studies have not been thoroughly investigated. The development of an efficient and reliable mesh sensitivity module with a special emphasis on the dynamics of falling body applications appears essential. Most literature looks at independence but not sensitivity. This research will investigate and show the estimation of the errors of the falling plate numerically based on the trajectory of the falling mode and velocities. It is, therefore, of great interest to investigate the motion of a freely falling plate and predict the motion and determine the numerical uncertainty at each point during the free fall by using the grid convergence index methodology based on the Richardson extrapolation *(RE)* method (Richardson and Glazebrook (1911)). However, the *CFD* community currently accepts no standard method for evaluating numerical uncertainty. The Richardson extrapolation method is chosen because of its wide recommendation for discretization error estimation, and the method has been investigated by many researchers (Celik et al. (2008)). The uncertainty analysis is centred on Richardson Extrapolation *(RE)* (Richardson (1927)). The *RE* gives a confidence level of only *50%*. For this reason, a variety of different methods are em-

ployed to predict the uncertainty with a *95%* confidence interval. Specifically, the Grid Convergence Index *(GCI)* method of Roache (1998), as well as the approaches of Xing and Stern (2010), and Stern et al. (2001), hereafter referred to as the *FSRE* (Factors of Safety for Richardson Extrapolation) and *CF* (Correction Factor) methods, respectively.

Finally, in all the previous experimental and numerical analysis of freely falling plates, a lot of parametric studies were carried out, such as the effect of aspect ratio (Wang et al. (2013)), density ratio (Wang et al. (2016)), turbulence (Esteban et al. (2020)), Reynolds number (Andersen et al. (2005a,b)), or aerodynamics of multiple free-falling plates (Kushwaha and De (2020)) and shape optimization (Vincent et al. (2020)). The dynamics of falling plate with initial speed was never investigated. This research investigated numerically for the first time to determine the effect of initial speed on the freely tumbling body under the influence of gravity. The whole trajectories of all the falling rectangular plates is analysed with their falling velocities, accelerations, and forces.

1.4 Thesis outline

This thesis has six chapters, including:

Chapter 2. (Critical Reviews) Presents different literature reviews that document important, relevant research on experimental, numerical, and theoretical studies on falling, rising, and fixed autorotation of plate problems challenges and research gap and finally, a summary of the approach to investigate the initial velocity problem.

Chapter 3. (Methodology) provides experimental, numerical, and uncertainty methodologies with a discussion of the approaches and laboratory set-up. The numerical simulation of falling bodies using the dynamic fluid body interaction *DFBI* model in Star-CCM+. This includes a description of the fluid domain and boundary conditions, the type of mesh and numerical discretisation schemes used, and the various sensitivity studies for spatial and temporal discretisation, solution schemes,

and turbulence modelling approaches. Finally, the method of determining the numerical uncertainty by using the Richarson extrapolation method is discussed.

Chapter 4. Presents experimental results with a phase diagram showing the transition between a zigzag motion to tumbling of the free-falling heavy rectangular plate in air and water with different initial angles of release.

Chapter 5. The verification and validation of the *CFD* model are presented with results against existing experimental and numerical measurements to show the tumbling case and to assess the accuracy of the simulation and determine the local uncertainty and errors during measurement. Both mesh and time study results were presented. The sensitivity to initial velocity results also presented with vortex shedding and wake structures.

Chapter 6. Summaries the main conclusions of the research and Future research.

Chapter 2

CRITICAL REVIEW

This chapter briefly describes the early discoveries of the falling body, narrowing down to the subject of this thesis. The existing literature review that documents relevant research on experimental, numerical, and theoretical studies on falling, rising, and fixed/free auto-rotation of plate problems challenges and research gap and finally a summary of the approach to investigate the initial velocity problem and numerical uncertainties of measurements.

2.1 The Historical Background of Falling, Rising and Fixed Plate Dynamics.

The rich dynamics phenomena of freely falling plates in air or water is a classical problem (Maxwell (1853)) and is also one of the central problems of fluid mechanics and aerodynamics, which have attracted a lot of research and have been studied for decades by the scientific community. In the mid-seventeenth century, Galileo Galilei dropped two metal balls from the leaning tower of Pisa and showed that they fall at the same rate despite the balls having different masses. In another version of the experimental determination of falling bodies, astronaut David Scott dropped a hammer and a feather on the moon and observed that they both hit the surface at the same time. Furthermore, Maxwell (1854) was the first to consider qualitatively the study of the motion of an object falling freely through air over *200*

years. Extensive experiments, numerical simulations, and theoretical analyses have been done to study how a body falls and how it changes between stable, fluttering, and tumbling, as well as critical conditions, flow structures, and dynamic behaviors.

In addition to free-falling bodies, fixed auto-rotating bodies have been extensively studied. Fixed-axis auto-rotation and freely falling tumbling plates have some similarities, but there are significant differences between the two phenomena. Riabouchinsky (1935) distinguished for the first time between auto-rotating plates with fixed axes and those with freely moving axes. The most important difference is that fixed-axis auto-rotation involves only the rotational degree of freedom of the plate, and thus the coupling between translation and rotation is absent. Therefore, it is not clear how results from the two different types of auto-rotation are related (Andersen et al. (2005a)).

The dynamics of a rising body in a fluid under the action of buoyancy, such as a bubble, is more complicated than that of solid bodies under the action of gravity because of the shape and coupling motion between the flow-induced stresses and surface tension and interfacial properties (Fernandes et al. (2007)). Leonardo Da Vinci *(1452 - 1519)* observed bubbles rising in water in a spiral motion about *500* years ago. The motion of a buoyant particle in a flow is a complex two-way coupled problem. The particle moves through the fluid in response to the flow fluctuations, and this motion, in turn, exerts a back-reaction on the flow (Mathai et al. (2018)).

2.2 Experimental study of Freely Falling Plates

Often due to the lack of accurate theoretical models to predict the dynamics of a falling object, as well as the fact that simulation of multi-particle flow is computationally expensive and can only be performed using high-performance computing, which explains why the dynamics of free-falling objects are investigated experimentally. Early experimental work on the *2D/3D* motion of rigid flat plates falling in a viscous fluid was mainly focused on the qualitative measurement and falling pattern of thin plates or discs in viscous fluid using sophisticated optical techniques

such as high-speed video cameras, particle image velocimetry *(PIV)* and the stereoscopic vision methods. Willmarth et al. (1964) investigated the freely falling motion of discs in a viscous fluid for the first time and reported three falling patterns as steady falling, fluttering, and tumbling, and constructed a phase diagram between the Reynolds number Re and dimensionless moment of inertia I^* showing the falling pattern. Smith (1971) also investigated the motion of a falling rectangular plate experimentally and constructed the phase diagram. Field et al. (1997) reported the experimental observations of falling discs in water and glycerol mixed and found four types of motion, mapping them out in a phase diagram. At the same time, the complex behaviour was reduced to a series of one-dimensional maps. Heisinger et al. (2014) dropped discs repeatedly in water to obtain the probability density functions of four falling motions as depicted by Field et al. (1997). Mahadevan et al. (1998) investigated the tumbling of rectangular cards dropped in still air with their long axis horizontal and observed a scaling law for the dependence of rotational speed. Xiang et al. (2018) investigated the *2D* trajectory mode of freely falling plates and visualised the corresponding wake patterns, and then compared them with the phase diagram of Smith (1971). They extended the phase diagram of Re and I^* to distinguished the transition between the regimes. Belmonte et al. (1998) conducted quasi-*2D* experiments with thin flat strips to examine the transition from fluttering to tumbling. In their research, the transition was determined by the Froude number Fr (similar to the non-dimensional moment of inertia), and the transition occurred at $Fr = 0.67 \pm 0.05$.

Andersen et al. (2005a,b) recorded the trajectory of a falling thin aluminium plates freely falling using high-speed digital video in a quasi-two-dimensional flow and obtained their instantaneous kinematics and aerodynamic forces and torque. Mahadevan et al. (1998) performed an experiment using long rectangular strips cut from reflective plastic shimstock to determine the average tumbling frequency. While Wang et al. (2013) experimentally measured the tumbling motion of a freely falling plate with an aspect ratio ranging from *2* to *10* using a high-speed video camera and

demonstrated the influence of aspect ratio on the tumbling motion, for some aspect ratio ranges, a double period rotation with period-doubling is observed. Yaginuma and Itō (2008) determined the drag coefficient of a freely falling cone with a vertex angle of *600* experimentally at an intermediate Reynolds number range from *90* to 8×10^3 the drag was determined based on the terminal velocity of the cone. The method was then used on the simple geometry of a flat plate to study the fall of a rigid card in a fluid initially at rest. The different forces and torques applied by the fluid on the card were analysed by broad-side on fall, where the plate falls in its horizontal position, and found to be unstable for small initial angles, and also a fluttering regime with growing amplitude was observed.

In addition to the *2D* dynamics of falling rectangular objects, the flow-visualization experiments for *3D* discs were performed together with the measurement of the Strouhal numbers. Veldhuis and Biesheuvel (2007) experimentally investigated the numerical work of Jenny et al. (2004) on the instability and the transition of the motion of solid spheres falling or ascending freely in a Newtonian fluid and verified some of the conclusions of the work. Apart from determining stable falling, fluttering, tumbling, and chaotic trajectories and mapping them, it is also essential to study the transition phase between the falling mode. Field et al. (1997) reported experimental observations of falling discs in water and glycerol mixed and found the instabilities of chaotic trajectories within the envelope of flight map between fluttering and tumbling. Bi et al. (2018) experimentally investigated freely falling annular discs and found an additional two falling modes and plotted a new phase diagram indicating the boundary between hula-hoop and helical motions. Zhong et al. (2011) experimentally investigated the falling pattern of thin discs using the stereoscopic vision method and identified a new falling pattern of spiral and transitional states. Zhong and Lee (2012) visualized the wake structure of circular discs falling vertically in quiescent water and found the evolution of the wake to be like the flow patterns behind a fixed disc of *Re 40-200*, a regular bifurcation occurs at critical Reynolds number. While Willmarth et al. (1964) investigated the motion of

steady and unsteady discs and found that the diverse motion of the discs exhibits a systematic dependance on the Re and I^*, in addition the relationship between Re and I^* along the boundary shows the separation between stable and unstable pitch oscillation of the discs. Ern et al. (2009) describes the dynamic model that predicts the zigzag motion of a disc and an oblate spheroid falling freely in a viscous liquid over a continuous range of aspect ratios and Reynolds numbers. By combining the findings and the scaling laws provided by a recent series of experiments. Ern et al. (2011) also reviewed and provided an overview on investigating the homogenous bodies with simple geometry bodies such as plates and circular cylinders whose span is much larger than any other characteristic dimension and axisymmetric bodies such as spheroids and discs of various thicknesses freely rising or falling. Zhong et al. (2013) experimentally studied the free-fall motion of a thin circular disc in still water and focused on the planar zigzag motion. The Reynolds number effects were studied by keeping the dimensionless moment of inertia and aspect ratio constant. By studying the flow pattern of the disc using dye visualisation and particle image velocimetry, they found the flow separation and vortex shedding to change with Reynolds number. Lee et al. (2013) investigated the free-fall motion of a thin disc with a small dimensionless moment of inertia experimentally and concluded the transition from two-dimensional zigzag motion to three-dimensional spiral motion occurs due to the growth of three-dimensional disturbance. The effect of the initial condition (release angle) was investigated. Two kinds of transition were observed: a zigzag-spiral and a zigzag-spiral-zigzag intermittence was reported. Zhong and Lee (2012) visualised the wake structure of circular discs falling in a quiescent fluid with a Reynolds number range from *40-200* and confirmed a regular bifurcation at the first critical Reynolds number, which leads to a transition from an axisymmetric wake structure to a plane symmetric one. Zhong et al. (2011) experimentally investigated the time evolution of a thin disc freely falling with six degrees of freedom motion and found that the dimensionless moment of inertia decreases. In addition, the trajectory of the falling disc transits from planar to nonplanar and new freely

falling motions such as spiral and transitional states were identified for small dimensionless moment of inertia values. And finally, the phase diagram corresponding to different flow regimes was plotted. Esteban et al. (2020) experimentally investigated the dynamics of freely falling thin discs settling through turbulence. The *3D* falling patten of the disc is studied using an orthogonal arrangement of two high-speed cameras while the turbulence is generated using a random jet array arrange in co-planar configuration. They observed a severe increase in the mean descent velocity with increasing magnitude of the turbulence velocity fluctuations up to *20%* of the velocity in quiescent flow for the disc with higher I^*. A new falling descent was reported as the disc fall through turbulence that didn't happen when they fall in still water.

Moffatt (2013) suggested investigations into disc falling in a viscous fluid by considering some factors such as roughness, wavy edge, and a hole on the disc, and the belief that having these factors may change the wake and thus influence the instabilities of the falling discs. Vincent et al. (2016) investigated the falling dynamics of a thin disc with a central hole experimentally and determined the effect of the central hole on the disc's motion for a wide range of Reynolds number, moment of inertia, and inner to outer diameter ratio. They found that by increasing the hole ratio, the disc transition changed from tumbling to chaotic and then fluttering at values of the moment of inertia not predicted by the falling mode of the whole disc. Blay Esteban et al. (2018) investigated the effect of edge geometry on the descent motion of freely falling planar particles such as discs and polygons with identical frontal area but different numbers of edges. Both disc and polygon parameters I^* and G^* are design to fall in the category of previous identified fluttering regime, but during the experimental studies several modes of secondary motion was observed for the same particle and conditions. The discs and heptagons are observed to display planar zigzag motion. Bi et al. (2018) experimentally investigated freely falling annular discs and found an additional two falling modes and plotted a new phase diagram indicating the boundary between hula-hoop and helical motion. Zhou et al.

(2021) experimentally investigated an eccentric annular disc with a hole falling in water with Re between *4000* and *21000* and found new dynamic behaviours and complex paths during the descent. They also classified the motion into fluttering, chaotic, tumbling, and transition motions, and also identified a new stable descending motion. The three descent modes of eccentric discs were mapped out in the *2*D phase space of e^* and I^*. In the end, it was decided that eccentricity is an important parameter to use when describing how eccentric discs fall.

2.3 Theoretical study of Freely Falling Plates

Most of the theoretical model is based on quasi-steady assumptions of Kirchhoff equations (Kirchhoff (1869)) for an incompressible, inviscid, irrotational fluid set of ordinary differential equations which generalise Euler's equation (Whittaker (1937)) that describes the motion of a solid body in a vacuum. Aref and Jones (1993) found chaotic behaviour in the Kirchhoff equations, while Tanabe and Kaneko (1994) investigated the behaviour of falling paper in a two-dimensional fluid by introducing a phenomenological model and including lift and friction terms. With the increase in friction coefficient, five falling patterns were discovered. At the same time, Belmonte et al. (1998) modified Tanabe and Kaneko (1994) model to include lift, gravity, and inertia drag to describe the tumbling and fluttering motions. Jones and Shelley (2005) investigated the characteristics of the frequency for a fluttering plate, and a linear relationship with the square root of the Froude number was derived.

Recently Vincent et al. (2020) investigated the two-dimensional effect of platform geometry on tumbling flight by designing wings of different platforms and length-to-width ratios, and drive theoretical prediction of the performance, which was tested experimentally, and they concluded the advantage and limitations of the theoretical approach on the design of efficient tumbling wings aerodynamically.

2.4 Numerical study of Freely Falling Plates

Theoretical progress is in part hindered by the lack of simultaneous measurements of instantaneous forces and flows around a falling object (Pesavento and Wang (2004)). An accurate and efficient simulation of freely falling, freely rising or fixed autorotation bodies is challenging, but nonetheless, numerical simulation due to control boundary conditions and initial conditions has an advantage over experiments but requires the development of specific mathematical algorithms to solve the coupling of body-fluid problems. A falling body exerts a complex dynamical interaction between the fluid and the body, which is governed by Navier Stokes and the equations for rigid body dynamics, determining the motion of the body, this problem being *2D* in the case of rectangular plates or *3D* in the case of planar particles such as discs. Recent advancements in computational fluid dynamics capabilities have allowed for better resolution of the flow field, which has led to a deeper understanding of the physics of bodies during free fall (Wu and Lin (2015)). However, the numerical simulation of freely falling objects is challenging since it requires simulating the moving solid boundaries with the flow. Haeri and Shrimpton (2012), in their review paper, introduced available methods based on the Navier Stokes equations for the simulation of particle flow and classified the methods into two general categories based on the treatment of the underlying mesh, namely fixed mesh methods and body conformal mesh methods. They further discussed the fixed mesh method into immersed boundary methods and fictitious domain methods. However, the fictious domain methods comprise of immersed boundary methods *(IBM)* and distributed Lagrangian methods *(DLM)*, which are used numerically to simulate falling/rising bodies of arbitrary shapes in a viscous fluid. While Maxey and Patel (2001) proposed a force coupling method as a simple and efficient *DNS* model for multi-particle flows, it was originally developed to simulate spherical particles but was later extended to simulate ellipsoid particles by Liu et al. (2009). Hu (1996) and Johnson and Tezduyar (1996, 1999) have developed a numerical procedure based on a finite element technique applied to moving unstructured grids to simulate the motion of

a large number of solid particles in a liquid flow. Hu (1996) used the generalised Galerkin finite element formulation to incorporate both the fluid and the particle equations of motion into a single variational equation of the Newtonian fluids. An arbitrary Lagrangian-Eulerian technique was adopted to deal with the motion of moving particles while eliminating the hydrodynamic forces and moments acting on the solid in the formulation. Johnson and Tezduyar (1996, 1999) investigated a new *3D* finite element flow simulation numerically for fluid-particle interaction and applied time-dependent behaviour for multiple falling spheres in a liquid-filled tube, and the capabilities are based on flow simulation of a stabilised space-time formulation of moving boundaries and interfaces, by automatically remeshing the structured layers of the elements around the sphere when needed. Uhlmann (2005) presented an improved method for computing incompressible viscous flow around a suspended rigid particle using a fixed and uniform computational grid. In addition, to avoid complicated interpolations and transformations of the force density on the boundary points, Wu and Lin (2015) developed a modified direct-forcing immersed-boundary pressure correction method to solve the freely falling behaviour of elliptical object with a small fixed aspect ratio of *0.125* in two-dimensional Navier Stokes equations, a phase diagram of the behaviour is established based on two-dimensional parameters i.e Re and I^*. They also found out that the initial inclination angle is likely to influence the falling speed especially in the chaos phase. Wang et al. (2016) investigated the *2D* rectangular plate falling freely in water numerically using an immersed boundary-lattice Boltzmann flux solver in a moving frame and constructed different phase diagrams using density ratio against aspect ratio and validated the numerical results. They also analysed the vortical structures in the modes and decomposed them into three typical stages of initial transient, deep gliding, and pitching up. Pan et al. (2002) numerically simulated an ellipsoid body moving in a narrow channel using a Lagrangian multiplier based fictitious domain method. They observed that during descent the ellipsoid moves to the centre of a channel and continues to move with its broad side perpendicular to the main stream direction. while Fonseca and

Herrmann (2005) used a constrained-force technique to study the settling motion of an oblate ellipsoid particle and attempted to reproduce the motion observed by Field et al. (1997). Andersen et al. (2005a) investigated a rectangular plate falling in water experimentally and validated the experiment results numerically. In their numerical simulation to avoid singularities at the edge of the rectangular plate, a plate with an elliptical cross-section was used. The instantaneous fluid forces and velocities were measured and compared. Discrepancies where found to be mainly due to a geometry difference. But later, Jin and Xu (2008) used an applied gas-kinetic scheme to study the trajectories and instantaneous forces of falling rectangular plates numerically and also shows that the inconsistency between the numerical and experimental results of Andersen et al. (2005a) is due to a numerical algorithm, not geometric shape. Jones (2003) modelled the separated flow of an inviscid fluid around a moving flat plate using an integral boundary representation for the complex-conjugate velocity field. In addition, they systematically derived a system of governing evolution equations for the problem, which ensured that all the necessary boundary conditions were automatically satisfied. Wang et al. (2016) numerically studied a two-dimensional falling rectangle plate with different solid-to-water density ratio and thickness-to-length ratio using the recently developed immersed boundary-lattice Boltzmann flux solver in a moving frame developed by Wang et al. (2015). A phase diagram documenting the different falling styles of the plates was constructed, and various instantaneous and mean kinematic properties of the plates and hydrodynamic forces were analyzed. Kolomenskiy and Schneider (2010) studied the dynamics of falling leaves numerically using a Fourier pseudo-spectral method with volume penalization to impose no-slip boundary conditions. Simulations were performed for different values of the Reynolds number, and comparisons with other numerical methods were made. Lau et al. (2018) also examines the transition of stable falling to tumbling for freely falling heavy plates in two dimensions using the immersed boundary method at a Reynolds number of up to 500 and dimensional moment of inertia up to 10. The study found that, depending on the initial angle of release, a plate may settle into

a stable falling or tumbling descent. Michelin and Llewellyn Smith (2009) proposed a *2D* vortex method coupled motion for a sharp-edge solid body in inviscid flow using the potential flow theory in high Reynolds flow. Zorzi et al. (2015) conducted a statistical analysis using the nonintrusive spectral projection method on the effect of fillet radii on the dynamics of a falling plate. In the stochastic simulations, the fillet radius of the plate was considered a random variable characterised by a uniform probability density function. In this way, some uncertainties in the plate's trajectory are determined and the mean trajectories and the error bar for the *95%* for both the fluttering and tumbling regimes are plotted.

More recently, Kushwaha and De (2020) numerically investigated the aerodynamics of multiple freely falling plates in a quiescent medium. The non-vertical descent motion of the plates shows a wide range of dynamical behaviour that depends not only on the shape but also on the relative initial orientation of the release. The collision between the plates and the subsequent movement through the vorticity field caused a significant difference with that of single plate trajectory behaviour. Rana et al. (2020) investigated the *2D* motion of a freely falling plate in water numerically using the diffuse interface immersed boundary method. The range of I^* For chaotic motion is found to extend with the increase in initial inclination angle. Also, fluttering and tumbling motions converge on a variety of initial states. They also found that the plate's solid-to-fluid density ratio changed how the chaotic motion changed into a flutter or a tumble.

3D planar bodies such as discs are investigated numerically. Chrust et al. (2013) numerically presented a comprehensive parametric investigation of freely falling homogenous thin disc and showed the problem to depend on two independent parameters, Galileo number G^* and non-dimensionless inertia of the disc. Dušek et al. (2016) numerically investigated the transition of freely falling homogenous and infinitely thin discs and mapped the regimes based on the Galileo number, which expresses the ratio between gravity and viscosity and the non-dimensionalized mass characteristic of the disc. Auguste et al. (2013) numerically investigated the dy-

namics of discs over a wide range of solid-to-fluid inertia ratios falling under gravity in a fluid medium at rest at infinity. By varying the density and thickness, the disc transition from a straight vertical path to a planar fluttering regime is found to exhibit complex dynamics. Jenny et al. (2004) numerically developed a spectral-spectral element method and investigated the transition of chaos of a sphere falling or ascending under the action of gravity in a Newtonian fluid. The results show that for all density ratios, the vertical fall or ascension becomes unstable via a regular axisymmetric breaking bifurcation. Shenoy and Kleinstreuer (2010) used a finite-volume method to determine the motion of a freely falling cylinder with a different aspect ratio in the zigzag regime, and the aspect ratio significantly changes the structure of the vortices shed by the disc and thus alters the fluid-induced forces. Deloze et al. (2010) studied the motion of a circular cylinder freely falling in a channel under the action of gravity using the automatic chimaera method implemented in the Navier-Stokes solver. Two parameters are considered for the descent of the cylinder diameter to the channel ratio and the fluid to particle density ratio, while the varying parameters are the initial position and the Galileo number. They found that the presence of the wall accelerates the oscillation motion while the initial position has no influence on the amplification of the transverse oscillations.

Finally, apart from the rigid body, flexible bodies falling freely are also studied numerically. Alben (2010) use inviscid simulation to analyse the dynamics of falling flexible sheets in two-parameter space while shedding vortex sheets according to the Kutta condition, using sheet density and bending rigidity. The sheet trajectories show persistent circling, quasiperiodic flapping, and more complex repeated patterns. For small bending rigidity, the motion becomes less regular. In contrast, at intermediate bending rigidity, trajectories show a well-defined falling angle relative to the vertical. Furthermore, at a larger sheet density and bending rigidity, the overall motion is more horizontal. Zhu (2007) simulated an inhomogeneous flexible filament freely falling in a viscous fluid with a low Reynolds number using the immersed boundary method. The work showed examples of filaments falling and

flexing and identified a sideways drifting motion. In addition, the results indicate unstable filament motion depends more firmly on the bending modulus than the mass density. A Hopf bifurcation takes place at the second critical Reynolds number as the wake structure becomes unsteady.

2.5 Dynamics of Freely Rising Object

In addition to the motion of free-falling objects, the motion of rising objects is also extensively studied. Fernandes et al. (2007) investigated the motion of freely rising axisymmetric rigid bodies under the action of buoyancy in a low-viscosity fluid. They found that beyond a critical Reynolds number, which depends on the aspect ratio, both the body velocity and the orientation start to oscillate periodically. Ellingsen and Risso (2001) investigated the rise of a bubble in still water and described the bubble shape, which was found to be similar to an oblate ellipsoid. In addition, they determined the trajectory of the bubble to start oscillating on an almost plane zigzag and then progressively transform into a helix, and the influence of surfactants to be negligible. Fernandes et al. (2005) investigated the zigzag path of a freely rising light-flat cylinder experimentally in water. They found that for thick bodies, both the axis and the velocity oscillate almost in phase, whereas for thin bodies, they are rather in quadrature. Zenit and Magnaudet (2008) experimentally studied the conditions at which the paths of freely rising bubbles of aspect ratio *2.36* to *2.0*, becoming oscillatory using silicon oil with viscosities ranging from *0.5* to *9.4* times that of water and Reynolds number *70* to *470*. It was found that the dominant parameter that triggers the instability is the bubble shape and not the Reynolds number since vorticity generated at the bubble surface is almost independent of the Reynolds number and mainly depends on the bubble aspect ratio. And finally, Saffman (1956) investigated a freely rising gas bubble in water and showed oscillatory behaviour when the bubble size exceeds a critical diameter. The rectilinear trajectory behaviour was becoming unstable with planar zigzag and helical motion.

2.6 Dynamics of Free and Fixed-axis Auto-Rotation

The dynamics of free/fixed plate tumbling or auto-rotating is complex. Studies on freely tumbling plates date back to Maxwell (1853), who described tumbling qualitatively. Dupleich (1949), in his well-known extensive experimental investigation, studied the rotation of an elongated rectangular paper cut out of pasteboard falling freely in the air and measured the descent angle and the average tumbling frequency. Smith (1971) performed an experimental study on the autorotation of a fixed-wing to uncover the mechanism and dynamics of the autorotation phenomenon with different Reynolds and Strouhal numbers. Lugt (1980) studied the autorotation of an elliptical cylinder numerically using Navier-Stokes equations and predicted angular velocity using potential flow theory. However, later, Iversen (1979) analysed the lift and drag coefficients for autorotating plates with different aspect ratio values and Reynolds numbers. Skews (1990) conducted a series of tests to determine the autorotation of a rectangular plate with a thickness to chord ratio varying from *0.1* to *1.0*. The plate spanned the entire width of the wind tunnel in two dimensions. The results show significant differences from predictions of infinite aspect ratio plates inferred from finite aspect ratio tests given by Iversen (1979). They found tip-speed ratios to be independent of thickness ratio, at approximately the Lugt (1980) value over the full range of thickness ratios. Also, drag coefficients were found to be independent of the thickness ratio. Also, there appears to be a critical thickness ratio above and below, in which the lift coefficients are constant but are of different magnitudes. Var (2011) studied falling maple seeds and characterised the falling flight as helical motion. Their investigation shows a seed with a torn wing that gyrates in a similar manner as a full-winged seed, and also a seed with only a sliver of leading-edge can gyrate, and thus the gyrating motion appears not to fully depend on the aerodynamic forces. Varshney et al. (2013) measured the three-dimensional falling kinematics of parallelograms and quantified their descent speed, azimuthal rotation, tumbling motion, and cone angle, and showed that parallelograms exhibit coupled motion of autogeneration and tumbling, similar to the

motion of tulip seeds. During the descent, the card has negligible horizontal drift and can maintains a steady cone angle. To extract the instantaneous forces and torques, they calculated the accelerations from the kinematic data and then applied the Newton-Euler equations, and the analyses show that regardless of the change of geometry angle of attack during tumbling, the magnitude and direction of the aerodynamic forces remain nearly steady.

2.7 Summary, Limitations and Conclusions

This study focuses on three different problems. The first experimentally investigates the transition from zigzag to tumbling of heavy plates falling in air and water at a range of Re and I^*, by introducing a new methodology of capturing the trajectories of the freely falling plate. In recent years, the measuring of falling plates using high-speed video cameras has been done using several methods. Some of the methods capture the difference in the number of image pixels of the moving plate and the homographic mapping of the motion vector from the image plane to the global coordinate plane. The systematic random errors produced by the existing methods lower the accuracy and convenience in determining the falling trajectory and velocities. Different errors can occur because of determining the falling time with a stopwatch and measuring the distance between measurements due to object sizes and shapes. In this research, we present a new method of capturing the motion of a freely falling plate using the Qualisys system, where the motion of the plate is measured in *3D* space by capturing the falling trajectories of the reflective maker attached to the plate. The cameras measure and reconstruct the cameras measures and reconstructs the *3D* motion in real-time at up to *1500-3000* frames per second. The cameras comprise industrial-grade components and combine with world-class highest pixels rate with low-latency output and sub-millimeter accuracy at distances of $\pm 35m$. In addition, we investigated the transitions from zigzag to tumbling motions of the freely falling heavy plates in the range of Reynolds number *270* to *23000*, dimensionless moment of inertia up to *23* and aspect ratio *5-39*. it

is desirable to extend the mapping of heavy plates from previous literature of Lau et al. (2018) to further understand the falling trajectories and bistability, since both experimental and numerical investigation of heavy plates at large Re, I^* and γ^* remain scarce.

The second problem is to validate the experimental model of previous literature and show the numerical uncertainty during the falling body. Predicting numerical models of fluid structural interaction has long been a significant interest in the research community, with great challenges posed by accuracy, stability, and computational cost. Since there is no overall best practice model universally applicable to select turbulence flows, this research will choose the best model to predict the instantaneous fluid forces and trajectories of falling plate numerically. Most of the research that has been studying the fluid-structure interaction of falling objects numerically and focusing on selecting the best method to predict the instantaneous fluid forces, trajectories, and vortex shedding, which play a vital role in the motion of the object, fails to show the errors and uncertainty of this numerical simulation. This research will investigate and show the error estimation of the falling plate numerically based on the trajectories and velocities of the falling mode. It is, therefore, of great interest to investigate the motion of a freely falling plate using a turbulence model to predict the motion and determine the numerical local uncertainty estimation of the falling mode at each point during the free-fall using the grid convergence index methodology based on the Richardson extrapolation *(RE)* method (Richardson and Glazebrook (1911)). However, the *CFD* community currently accepts no standard method for evaluating numerical uncertainty. The Richardson extrapolation method is chosen because of its wide recommendation for discretization error estimation, and the method has been investigated by many researchers (Celik et al. (2008)).

Finally, from the previous studies, it should be noted that the case of freely falling objects is very sensitive to perturbations or initial conditions. Therefore, investigating the effect of initial velocity on the trajectories and descent velocity of

freely falling bodies numerically or experimentally to our knowledge has not been studied in previous literature, despite the extensive research carried out on the motion of discs, plates, polygons, and wavy-edge particles falling freely or fixed in quiescent fluid and particles falling in background turbulence.

Chapter 3

METHODOLOGY

This chapter discusses the experimental, numerical, and uncertainty techniques, as well as the methodology and laboratory setup. Developed a numerical technique for solving the Navier-Stokes equations in the simulation of a falling body using *DFBI* in STAR-CCM. This includes a description of the fluid domain and boundary conditions, the type of mesh and numerical discretisation schemes used, as well as the various sensitivity studies for spatial and temporal discretisation, solution schemes, turbulence modelling approaches, and non-dimensional parameter determination discussed. Finally, the Richarson extrapolation approach for assessing numerical uncertainty is explained.

3.1 The Experimental Set-up, Apparatus, and Measurement Procedure

To capture the real-time dependent motion of a heavy plate falling with six degrees of freedom in air and water, the motion of the falling rectangular plate was recorded using a Qualisys camera with a marker attached to the falling rectangular plate. Figure 3.1 to Figure 3.4 show the experimental set-up and arrangement of the apparatus, which comprises a Qualisys camera (Oqus system), a stand with clamps and a release mechanism.

A calibration was performed to capture the motion of the body using a towing

tank of size *76m ×4.6m ×2.5m* and an in-air drop of size *15m ×7m ×3.5m* in the Kelvin hydrodynamic laboratory at the University of Strathclyde, Glasgow, United Kingdom. For both setups, first the Oqus cameras were connected, and the Qualisys *DHCP* server interface was connected to the power ports and data ports while running. However, before capturing the motion on the Qualisys systems, the computers were calibrated and prescribed precisely where the cameras were with respect to each other and the environment around them, including force plates, so that the maker data would be captured accurately. Reflection was cleared in the laboratory within the volume of interest to make sure the cameras are not picking up phantom markers caused by reflective surfaces or direct light sources. The L-frame device shown in Figure 3.3 was used to define the global coordinate systems X, Y and Z axes of the laboratory volume during the calibration, by using a calibration wand. The wand was twisted until it clicked into place, both shown in Figure 3.3. A project folder was created. Underwater makers of *14mm* diameter with a mass of *15g* shown in Figure 3.6 and retro-reflective sheet are placed on the rectangular plate with a bone length tolerance of *5mm*, and at least three cameras must capture the maker to create a *6Dof* rigid body of the local origin system of x,y and z of the rectangular plate as shown in Figure 3.7 and Figure 3.8. The measured separation between the two makers is kept in the range *95mm - 150mm* for the *QTM* tracking to accept the possibility that the calculated markers may be the pair specified for the rigid body by setting the exposure time at *200 - 300* microseconds with a maker threshold of *20*, with a capture rate of *100Hz*. The position of the centre of mass x,y and z and the three Euler angles $roll(\theta)$, $pitch(\phi)$ *and* $yaw(\vartheta)$ were tracked throughout the descent of the rectangular plate as shown in Figure 3.5. The experimental matrix used is presented in Table 3.1.

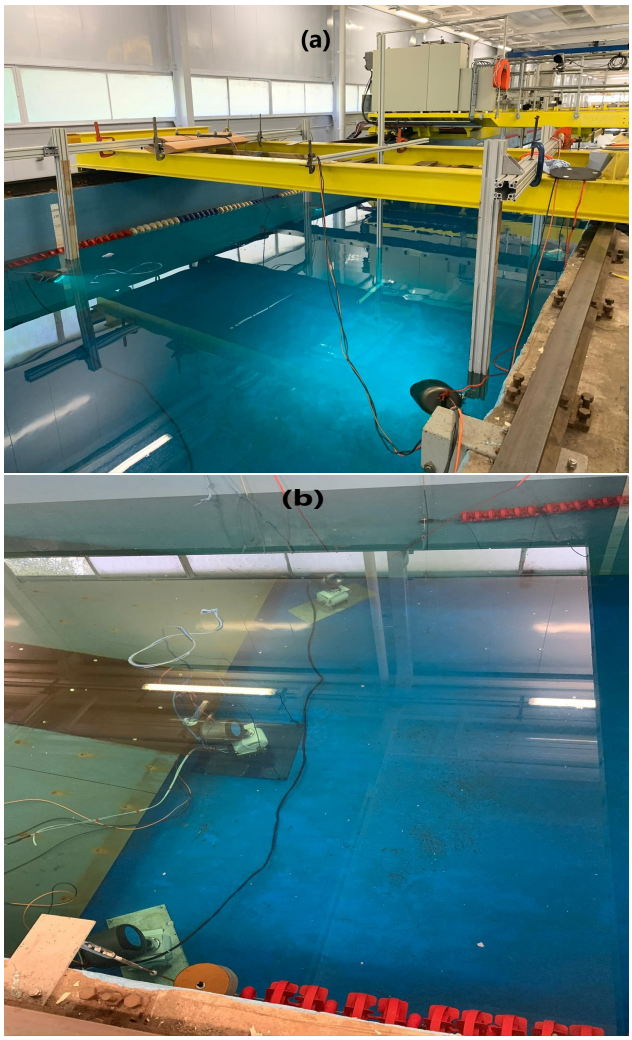

Figure 3.1: Schematic of the underwater experimental set-up with (a) qualisys camera above and (b) below the Water Surface

Figure 3.2: Schematic of the in-air experimental set-up with (a-b) qualisys camera above.

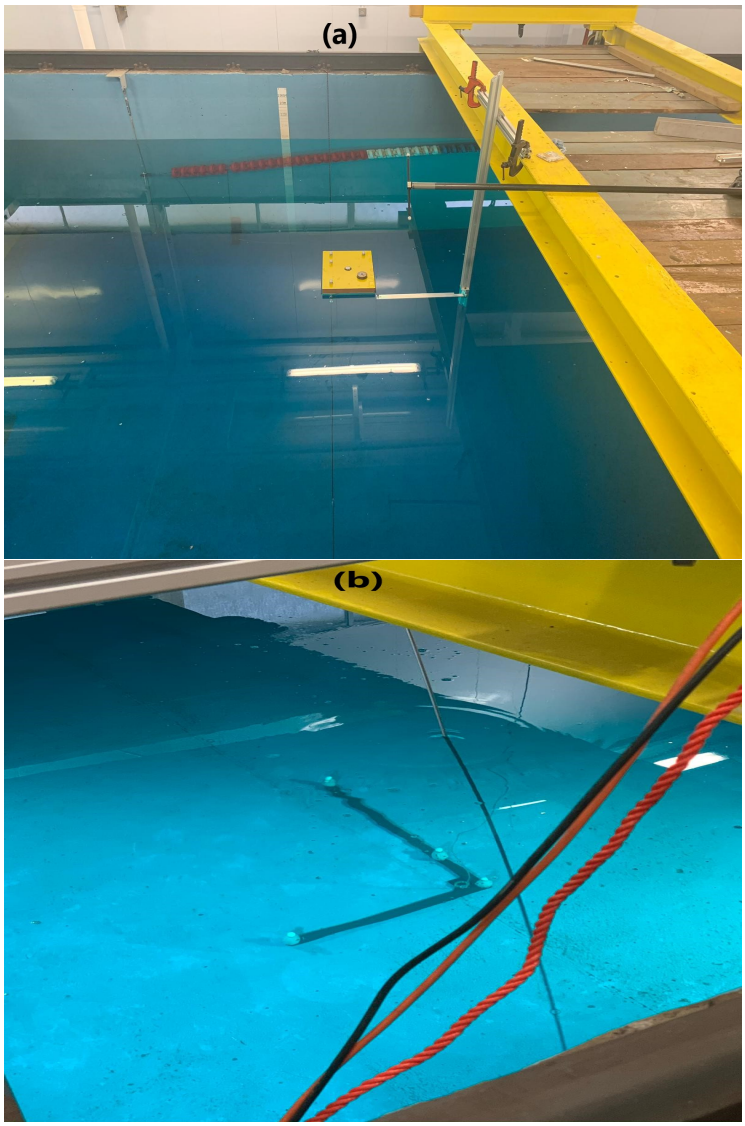

Figure 3.3: (a) Release mechanism clamped to the beam with wand and (b) L-frame for setting out the laboratory coordinate system.

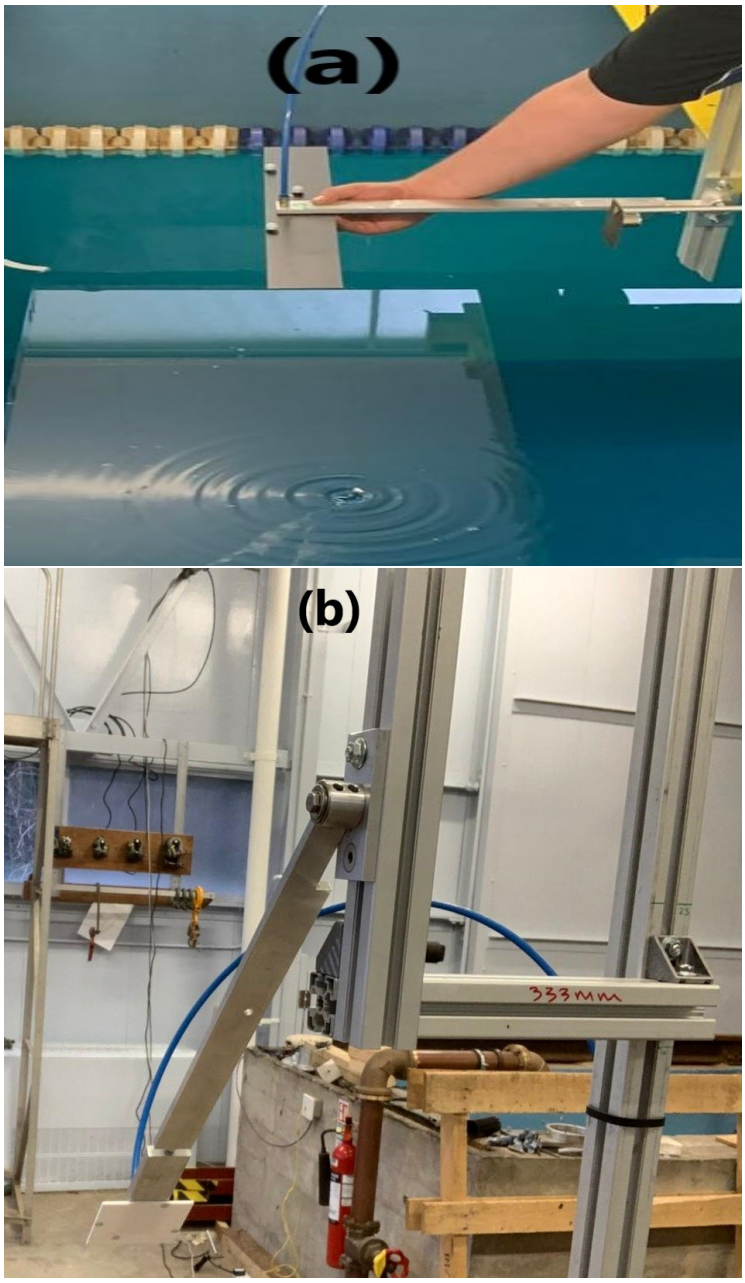

Figure 3.4: (a) Underwater and (b) in-air release mechanism with a plate attached.

The *6DOF* tracking function in Figure 3.5 uses the rigid body definition on the plate to compute the $\boldsymbol{P_{origin}}$ Equation (3.1) of the positional vector on the origin of the local coordinate system in the laboratory global coordinate system, and $\boldsymbol{R}$, the rotational matrix, which describes the rotation of the plate during descent.

The rotation matrix $\boldsymbol{(R)}$ can be used to transform a position $\boldsymbol{P_{local}}$ (x_1,y_1,z_1) in the local coordinate system, which can be translated and rotated to the global laboratory position as $\boldsymbol{P_{global}}$ $\boldsymbol{(X,Y,Z)}$. The following equation is used by the *QTM*

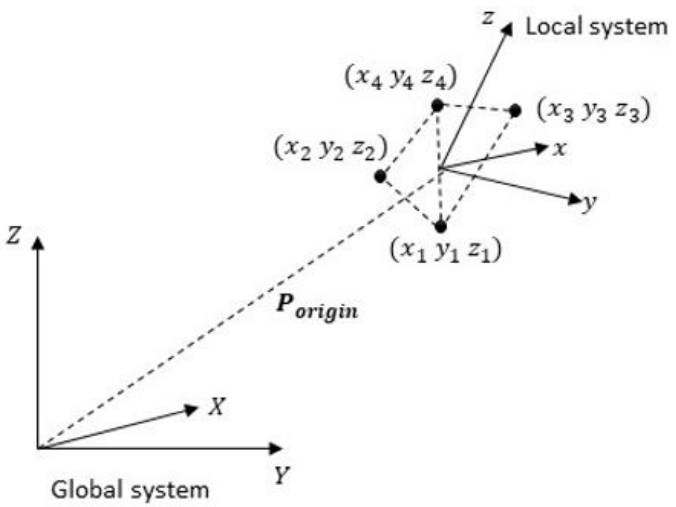

Figure 3.5: Global and local coordinate system of the rectangular plate.

to transform the position of the plate from the laboratory global coordinate system.

$$P_{\text{global}} = R \times P_{\text{local}} + P_{\text{origin}} \tag{3.1}$$

the plate rotational angle is calculated from the individual rotational matrix ***(R_x,R_y,R_z)*** by expressing in the three rotational angles of *roll*(θ), *pitch*(ϕ) and *yaw*(ϑ) Equation (3.2) to Equation (3.4). The rotation is around the ***X, Y, and Z-axis*** positive rotation is clockwise when looking in the direction of the axis. In addition, the three rotational matrixes are written as:

$$R_{\text{x}} = \begin{bmatrix} 1 & 0 & 0 \\ 0 & \cos\theta & -\sin\theta \\ 0 & \sin\theta & \cos\theta \end{bmatrix} \tag{3.2}$$

$$R_{\text{y}} = \begin{bmatrix} \cos\phi & 0 & \sin\phi \\ 0 & 1 & 0 \\ -\sin\phi & 0 & \cos\phi \end{bmatrix} \tag{3.3}$$

$$R_{\mathrm{z}} = \begin{bmatrix} \cos\vartheta & -\sin\vartheta & 0 \\ \sin\vartheta & \cos\vartheta & 0 \\ 0 & 0 & 1 \end{bmatrix} \tag{3.4}$$

The rotational matrix of the plate ***(R)*** is then calculated by multiplying the three rotational matrixes. The *roll* is applied first, followed by *pitch* and then finally *yaw*.

$$R_{\mathrm{x}}.R_{\mathrm{y}}.R_{\mathrm{z}} = \begin{bmatrix} r_{11} & r_{12} & r_{13} \\ r_{21} & r_{22} & r_{23} \\ r_{31} & r_{32} & r_{33} \end{bmatrix} \tag{3.5}$$

$$R_{\mathrm{x}}.R_{\mathrm{y}}.R_{\mathrm{z}} = \begin{bmatrix} \cos\phi.\cos\vartheta & -\cos\phi.\sin\vartheta & \sin\phi \\ \cos\theta.\sin\vartheta + \cos\vartheta.\sin\theta.\sin\phi & \cos\theta.\cos\vartheta - \sin\theta.\sin\vartheta.\sin\phi & -\cos\phi.\sin\theta \\ \sin\theta.\sin\vartheta - \cos\theta.\cos\vartheta.\sin\phi & \cos\vartheta.\sin\theta + \cos\theta.\sin\phi.\sin\vartheta & \cos\theta.\cos\phi \end{bmatrix} \tag{3.6}$$

The equation below calculates the rotational angles from the rotational matrix:

$$pitch(\phi) = \arcsin(r_{13}) \tag{3.7}$$

$$roll(\theta) = \frac{\arccos(r_{13})}{(\cos\theta)} \tag{3.8}$$

$$yaw(\vartheta) = \frac{\arccos(r_{11})}{(\cos\theta)} \tag{3.9}$$

The range of *pitch* angle is *-90^0* to *90^0* because of the *arcsin* function, while the range of the *arcos* function is *0^0* to *180^0*, but the range of *roll* and *yaw* are *-180^0* to *180^0* since r_{23} and r_{12} can be expanded with the element of the rotation matrix ***R***, since the *roll* and *yaw* will have the opposite sign compared to the elements and *cos*ϕ is always positive when ϕ is within $\pm 90^0$.

Table 3.1: Experimental test matrix

Experimental Set-up	Plate Name	Drop Angle (Degree)										Number of Drops	Dynamics
		0	5	10	15	20	25	30	35	40	45		
In - Air	A1	X	X	X	X	X	X	X	X	X	X	150	Fluttering
	A2	X	X	X	X	X	X	X	X	X		150	Fluttering
	C1	X	X	X	X	X						75	Fluttering
	C2	X	X	X	X	X	X	X	X	X	X	150	Fluttering
	D1	X	X	X	X	X	X	X	X			135	Fluttering
	D2	X	X	X	X	X	X	X	X			120	Fluttering
	D3	X	X	X	X	X	X	X				120	Fluttering
	D4	X	X	X	X	X	X	X				105	Fluttering
	D5	X	X	X	X	X	X	X				105	Fluttering
Underwater	A1		X	X	X	X	X	X				30	Fluttering
	A2	X										5	Tumbling

3.2 Under-water Drop Set-up and Kinematics

The first test was conducted in the Kelvin Hydrodynamic Laboratory towing tank filled with water of density $996kg/m^3$ with a kinematic viscosity of $1.02 \times 10^{-6}\ m^2\ s^{-1}$, a drop length of $2m$ as shown in Figure 3.1, a release mechanism clamped on the top of the towing tank, used in holding the plates and dropping the plates below the water surface with a well-controlled initial condition and with zero initial velocity to allow a couple of turning points with a room temperature of 20^0. Four cameras were used to capture the motion of the falling body, with each plate dropped five times and measurements recorded. The plate was fished out with a magnetic clamp, and the tank was kept undisturbed for at least 10 - $15mins$ for the water to be still. The plates were mounted on the release mechanism with vacuum, which can be seen in Figure 3.4. An aluminium plate with a density of $2700\ kg/m^3$, with the same thickness but a different aspect ratio, was used.

The experiments were recorded with four cameras mounted at the top of the

towing tank facing directly downward, located at a distance of $2m$, the plates X, Y and Z is the laboratory frame, in which $"X"$ and $"Y"$ form the horizontal plane and $"Z"$ corresponds to the vertical axis. $"xyz"$ is the rectangular plate frame with $"x"$ the diagonal axis, $"y"$ the chord direction, and $"z"$ normal to the plate plane as shown in Figure 3.7. The plate descent is measured by capturing the centre of mass of the plate throughout, and two different plates were tested to show fluttering and tumbling behaviour released at different angles of 5^0 - 45^0 for fluttering and 0^0 For the tumbling plate. Figure 3.5 shows the Euler angles and the frame of reference of X, Y and Z in the laboratory frame and x, y and z the local rectangular plate frame.

For the fluttering case above 30^0 The plate moves out of range of the four cameras. A total of 35 trajectories were recorded as shown in Table 3.1, where some were discarded. The $6DOF$ real-time output of the trajectories and orientations of the plates was extracted from the QTM system. The velocities were calculated based on the distance and time of the free-fall, while a low-pass filter was used to filter out high-frequency noise of the measured data to obtain smooth instantaneous velocities and angles, and the average translating and angular velocity were calculated from the smooth instantaneous velocities (Wang et al. (2013)). At the same time, a statistical method is applied to calculate the sample mean and 95% confidence interval.

To determine the motion of a heavy plate falling in water, each drop is kept consistent with a different initial angle and plate aspect ratio. To create a project folder, two plates were name $A1$ & $A2$ as shown in Table 3.2.

Table 3.2: Underwater experimental parameters with a different initial angle of release and number of drops.

SN	Dimension(mm)	Angle(Deg)	Number of Drop	Motion	Aspect Ratio γ^*
1	80 $\times$2.03 $\times$ 650	5 - 30	30	Fluttering	39.0
2	15 $\times$2.03 $\times$ 650	0	5	Tumbling	7.3
	Total		35		

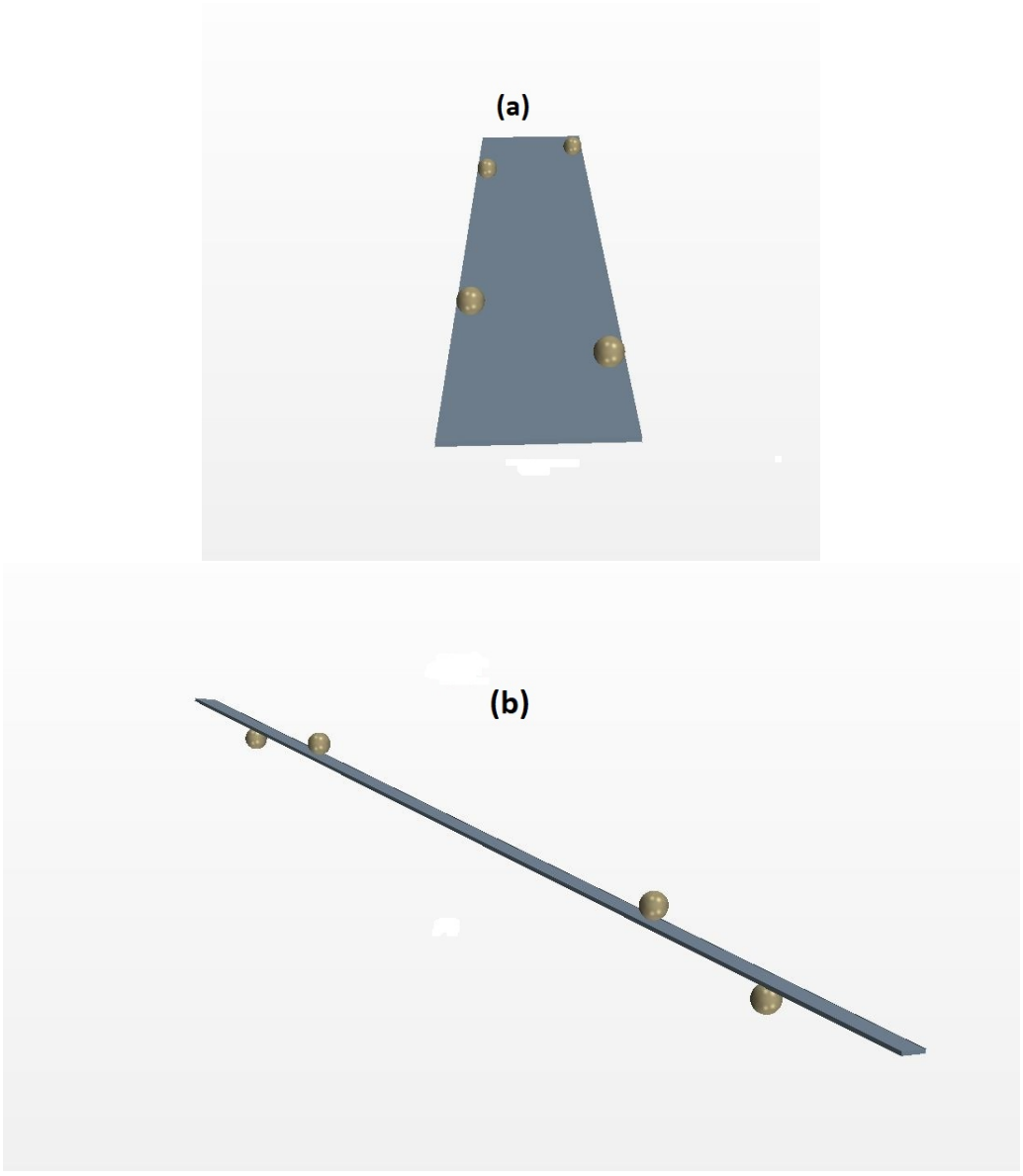

Figure 3.6: (a) Underwater fluttering, and (b) tumbling plates with makers attached.

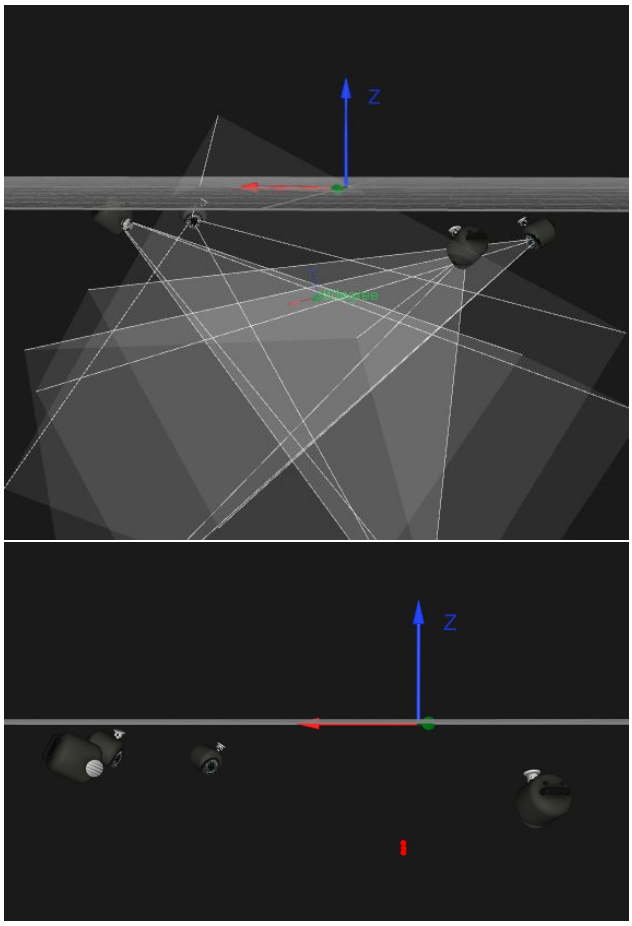

Figure 3.7: Schematic of qualisys cameras capturing the motion of falling plate underwater

3.3 In-Air Drop Set-up and Kinematics

To determine the bistability of falling cards in-air, an experiment was conducted to capture the real-time dependence of the freely falling cards with *6DOF*, record the trajectories, and check their dependence on the initial angle of release. Six cameras were used to capture the motion of the falling body with each plate drop *15* times, and the release was kept consistent by checking the position and orientation on the *QTM*. The different cards used for the experiment are machined into different sizes as shown in Table 3.3. Figure 3.2 shows a schematic of the experimental setup. The motions are captured with a Qualisys camera shown in Figure 3.8 at a frame rate of *1500 - 2500*.

The six cameras mounted at the top of the roof beam facing directly downward,

located at a distance of *3.5m* as shown in Figure 3.2, the cards X, Y and Z is the laboratory frame, in which *"X"* and *"Y"* form the horizontal plane and *"Z"* corresponds to the vertical axis. *"xyz"* is the cards frame with *"x"* the diagonal axis, *"y"* the chord direction, and *"z"* normal to the plate plane as shown in Figure 3.8. The cards descent is measured by capturing the centre of mass of the card throughout, and six different cards were tested to show bistability behaviour released at different angles, as shown in Table 3.1. The cards used in the present study are made up of cardboard with different chord lengths as well as different thicknesses. A card with sufficient stiffness was chosen to avoid bending.

The experiment was conducted in a closed room away from windows and ventilators to reduce the effect of wind. The cards were dropped from a releasing mechanism of the launching platform at a drop height of *2m*. The launching platform is designed at sufficient length to control initial conditions and with zero initial velocity to allow a couple of turning points and also eliminate the ground effects as much as possible. At the top of the platform, a releasing mechanism with a vacuum attached to hold the card. The release mechanism can move up and down by a motor at the top to change the initial angle of release from 0^0 - 90^0. To determine the motion of cards falling in air, each drop is kept consistent with a different initial angle and plate aspect ratio, as shown in Table 3.3.

Table 3.3: In-air experimental parameters with a different initial angle of release and number of drops.

Name	L(mm)	H(mm)	W(mm)	Mass(g)	Angle (Deg)	Number of Drops	Aspect Ratio γ^*
C1	595	3	15.0	4	0 - 20	75	5.0
C2	595	3	20.0	5	0 - 45	150	6.7
A1	595	3	45.0	13	0 - 45	150	15.0
A2	595	3	65.0	18	0 - 40	150	22.0
D1	539	3	87.3	22	0 - 35	135	29.1
D2	539	3	85.7	21	0 - 35	120	28.6
D3	539	3	90.0	22	0 - 30	120	30.0
D4	572	5	85.7	24	0 - 30	105	17.1
D5	542	5	90.0	24	0 - 30	105	18.0
Total = 1065							

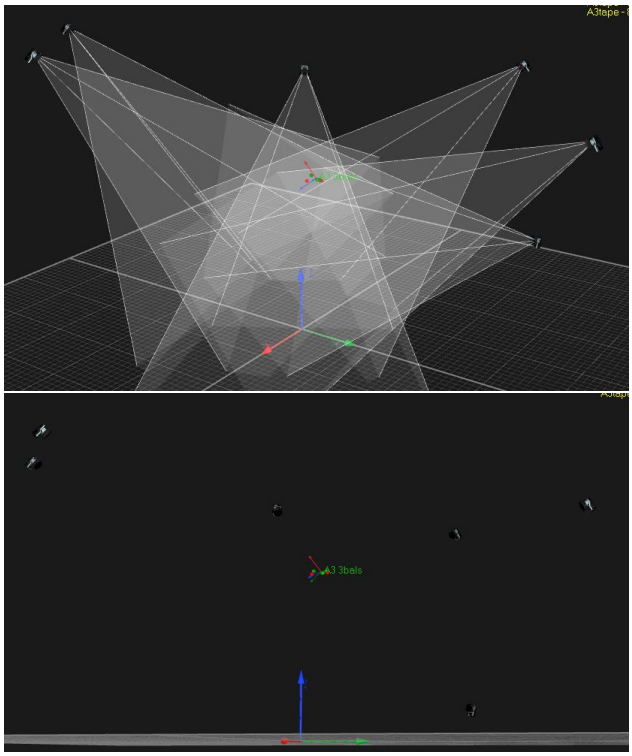

Figure 3.8: Schematic of qualisys cameras capturing the motion of falling plate in-air.

To create a project folder, different project names were created, as shown in Table 3.3, and a total of *1065* trajectories were recorded, where some were discarded. The *6DOF* real-time output of the trajectories and orientations of the cards were extracted from the *QTM* system, the velocities were calculated based on the distance and time of the free fall, and a low pass filter is used to filter out high-frequency noise of the measured data to obtained smooth instantaneous velocities and descent angles, while the average translating and angular velocity are calculated from the smooth instantaneous velocities (Wang et al. (2013)). At the same time, a statistical method is applied to calculate the sample mean and *95%* confidence interval.

3.4 Numerical Method Used for the Validation

The depth and scope of fluid dynamics research using *CFD* simulation are increasing due to the improvement of computational fluid dynamic theory and numerical methodology. The accuracy of the numerical simulation of the flow field is also improving (Li et al. (2019)).

Dynamic/morphing mesh, arbitrary mesh interface *(AMI)*, overset mesh and sliding grid interface are the four most common methods used in simulating moving bodies in engineering and research applications such as rotating turbine, floating and oscillatory bodies and falling plates in fluids (Zorzi et al. (2015); Verma and Hemmati (2020);). This analysis was carried out with commercial software Star-CCM+ , version 13.4.011. In the software, there are three ways to simulate a moving body: morphing/remeshing, overset mesh, and sliding grid interface methods. With the morphing mesh approach, due to the requirement of remeshing operation, a huge amount of computational time is needed, and because of mesh deformation, the approach becomes unstable (Casalone et al. (2020)). But by using an overset mesh, no remeshing operation is needed, nor does the quality of the mesh decrease since the body moves within the fluid domain unaltered. To model the tumbling mode with high accuracy,an overset meshes, also called Chimera or overlapping grids, are used to discretise the computation domain and idealise the motion of the plate

in an effective way. Two regions are created: a background region and an overset region, as shown in Figure 3.11, where the free surface refinement is also extended in the background grid. The overset grids are attached to the floating body and move with it freely depending on the motion response. The background region is fixed in space, and the overset mesh can move freely relative to the background region. The governing equations are discretised on the overset mesh boundaries and are solved simultaneously for all the cells in the overlapping region; that is, the coupling between the meshes are implicit.

The *2D* motion is modelled using a one-cell-thick *3D* mesh instead of *2D* mesh, and this choice is possible using Simcenter Star-CCM+ (Zorzi et al. (2015)). A Quad dominant surface remesher method with a trimmed cell was used for both the fluid and rotating domains to produce a high-quality grid mesh generation.

The fluid domain had a refined mesh size with a volumetric control custom size of *10%*, while the rotating domain had a volumetric control custom size of *50%*, to have better dimensional control of the cells. Both the fluid and the rotating domain are imposed with an absolute value so that if the base size value decreases, the number of the cells on the grid increases, which leads to better flow discretization and reduces minor numerical errors. Figure 3.11. shows the view of the mesh generated for both the rotating and fluid domains for different mesh sizes. To capture the near-wall flow accurately, the rotating domain with a plate no-slip boundary condition is used. By solving the coupled systems of Navier-Stokes equations with Newton's law, you can also figure out how the plate moves in a viscous fluid.

3.4.1 Numerical Setup

In this section, the relevant details regarding the numerical setup are discussed. The section will provide details of the numerical simulation; flow solvers; rigid body motion equation; computational domain and grid set up; boundary conditions; and time step selection for both the tumbling cases.

3.4.2 Rigid Body Motion Equation

For the rigid body dynamics, the unsteady fluid structural interaction behaviour of the plate is modelled in Simcenter Star-CCM+ by coupling the computational fluid dynamics with the rigid body dynamics. For the fluid part, the *2D* Reynolds Averaged Navier-Stokes (RANS) *CFD* models are used to simulate the unsteady and non-uniform sequential coupling with the *CFD* code. At the same time, the rigid body dynamic *(RBD)* solver allows more detailed modelling of the falling body. Using the applied body forces and moments, the translation and rotation of the plate were calculated based on the laws of linear and angular momentum conservation given as Equation (3.10).

$$F = m\frac{\delta v}{\delta t} \tag{3.10}$$

Where the mass of the plate is m, v is the velocity on the centre of mass, F the resultant force acting on the body, and t is the time.In addition, the body rotational velocity in the local coordinate system with the plate centre of mass can be written as Equation (3.11):

$$M = I\dot{\omega} + \omega \times I\omega \tag{3.11}$$

Since the falling plate case is in *2D*, the equation above can be written as Equation (3.12):

$$M = I_{zz}\dot{\omega} \tag{3.12}$$

Where M, I, ω are the resultant moment acting on the body due to fluid force, tensor of the moment of inertia, and the angular velocity of the rigid body.

3.4.3 Flow Solver

The motion of an object immersed in a fluid is governed by the mutual interaction of the fluid and solid phase, known as fluid-solid interaction *(FSI)*. The fluid exerts a hydrodynamic force on the object while, at the same time, the object disturbs the flow. In addition, the *2D* flow governing equations for the freely falling plates are considered in compressible. Also, the volumetric mass and the kinematic viscosity of the continuous phase are considered constant to simplify the mathematical formulation. Since these flow governing equations are based on the principles of continuity (mass conservation) and momentum conservation, the Navier-Stokes equations formula is given as Equation (3.13) and Equation (3.14):

$$\bigtriangledown.u = 0 \tag{3.13}$$

$$\frac{\sigma u}{\sigma t} + (u.\bigtriangledown)u = -\frac{1}{\rho_{\mathrm{f}}} \bigtriangledown .p + \nu \bigtriangledown^2 u \tag{3.14}$$

To also capture the dynamic forces on the plate, it is important to know the pressure field around the plate from the solved flow equations above. u is the velocity, t the time, p static pressure, ρ_f density of the fluid and v the kinematic viscosity.

3.4.4 Computational Domain and Boundary Conditions

In fluid dynamic simulations of a tank test, it is not advisable to use the real dimensions of the tank for a computational domain. Using the real tank size would be a waste of computational resources and bring no benefit to accuracy (Casalone et al. (2020)).

In addition, when solving the fluid governing equation, i.e. Navier-Stokes equation and continuity equations, suitable initial and boundary conditions need to be applied depending on the physics of the problem to be solved. Figure 3.9 and Figure 3.10 shows a view of the computational domain and boundary conditions. The

selection of the boundary is based on Hærvig et al. (2017) and Zorzi et al. (2015). But numerical boundary conditions can be put into two groups: Neumann (value is fixed) and Dirichlet (gradient is fixed).

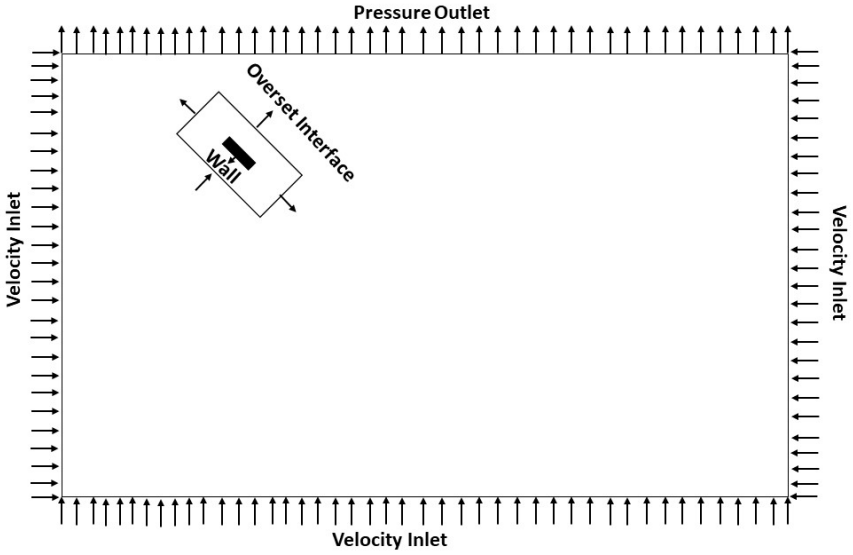

Figure 3.9: Computational domain with overset boundary conditions for tumbling case with 45^0 drop angle

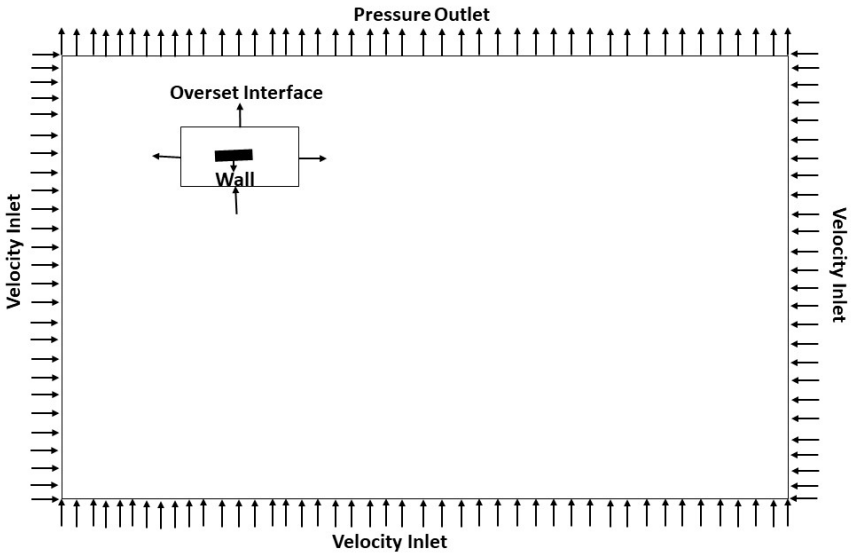

Figure 3.10: Computational domain with overset boundary conditions for tumbling case with 0^0 drop angle

As shown in Figure 3.9 and Figure 3.10 the top face of the domain has a pressure outlet Neumann condition. A pressure of *0 Pa* is imposed on on the domain's top face. The body-fluid interface, i.e., the plate, is specified with a wall condition and set as a no-slip condition due to the friction effect. In addition, velocity inlet is applied to the bottom and lateral faces of the computational domain as a Dirichlet condition. A symmetry plane was applied to the face of the fluid domain to put the imaginary plane of symmetry in the simulation. An overset interface was created between the fluid domain and the rotating domain, and this boundary condition allows mesh overlap.

3.4.5 Physical Modelling and Grid Generation

The numerical computation in this study was performed using the state-of-the-art commercial *CFD* software Simcenter Star-CCM+. In the software, the flow is solved accurately using the finite volume method *(FVM)* to discretize the integral form of the Navier-Stokes equation. In the finite volume method, the solution domain is subdivided into a finite number of small control volumes, which corresponds to the cells of the computational domain. At the same time, continuity and momentum are linked via a predictor-corrector scheme. Accuracy and expediency in *CFD* solutions depend not only on numerical methods but also on the grid generation process. In addition, uniform grids have many advantages over non-uniform grids in terms of accuracy and faster convergence (Ghoreyshi et al. (2015)). The *2D* motion is modelled using a one-cell-thick *3D* mesh instead of *2D* mesh, and this choice is possible using Simcenter Star-CCM+ (Zorzi et al. (2015)). A quad mesh with a dominant surface remesher method and trimmed cell mesher was used for both the fluid and rotating domains to produce a high-quality grid mesh generation. In order to simulate the motion of a freely falling plate numerically, the *DFBI* translation and rotation with the overset mesh boundary method is used. This approach is particularly suitable for freely falling objects because of the larger rotating angles, while a fine mesh restricted only in the object region is required (Zorzi et al. (2015)).

The *DFBI* method simulates the motion of the rigid body in response to the forces exerted by the physics continuum. Simcenter Star-CCM+ calculates the resultant force acting on the rigid body and solves the governing equations of motion to find a new position of the rigid body. The *6DOF/3DOF* body is required to interact with the physics continuum to calculate the fluid forces and moments acting on it. The geometric mesh model shown in Figure 3.11. consists of a fixed fluid region with an overset rotating region.

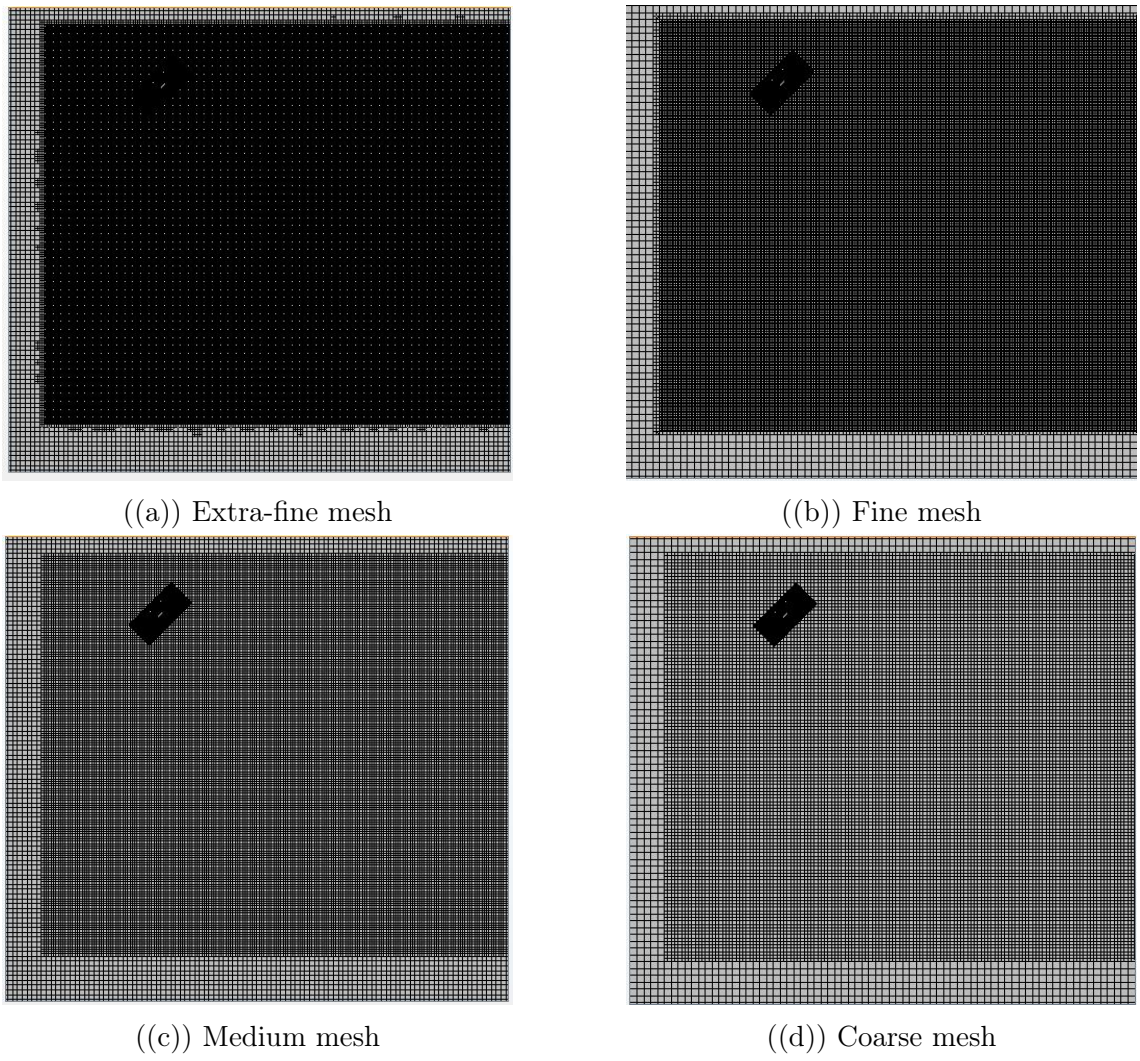

((a)) Extra-fine mesh

((b)) Fine mesh

((c)) Medium mesh

((d)) Coarse mesh

Figure 3.11: 45^0 drop angle Star CCM+ mesh configuration (a) extra-fine mesh (b) fine mesh (c) medium mesh (d) coarse mesh for tumbling case

A base size is selected as a parameter to set the mesh size for the surface mesh. Each cell size in the computational domain and rotating domain is set as a function of the percentage of the base size. If the base size value is decreased, the number of

cells on the grid increases and the grid becomes finer Table 3.4 shows the mesh size and the expansion ratio used.

Table 3.4: Number of cells, base size and mesh expansion ratio.

Mesh	Cells Number	Expansion Ratio	Base Size(m)
Extra-Fine	147896	$\sqrt{2}$	0.025
Fine	82052	$\sqrt{2}$	0.035
Medium	49468	$\sqrt{2}$	0.042
Coarse	32272	$\sqrt{2}$	0.07

3.4.6 Selection of Time Step

The Courant-Friedrichs-Lewy *(CFL)* number is sometimes used to determine the time step for time-accurate simulations as well as conditions to assess the convergence of the simulation flow in an explicit time integration scheme, and it should have an average value of *1* in all the cells to keep the flow movement by about one cell size per time step. If a second-order scheme is applied for time integration, then the average Courant number should be less than *0.5* (Tezdogan et al. (2016)).

The *CFL* number can be defined at the ratio of the physical time step *(t)* to the mesh convection time scale, relates to the mesh cell dimension *(x)* to the mesh flow speed *(U)* as shown in Equation (3.15) below:

$$CFL = \frac{U\Delta t}{\Delta x} \tag{3.15}$$

Generally, for implicit unsteady simulations, the time step is determined by the flow properties rather than the Courant number (Tezdogan et al. (2016)). But in this research, an implicit unsteady approach was used for the *CFD* simulation for better numerical stability (Rana et al. (2020)). A falling pate is an unsteady problem, and time-derivative terms must be discretized. In Star-CCM+, two different temporal schemes are used: first-order and second-order schemes. The second-order

scheme was used in the simulation with a convective term of the second-order upwind scheme, which calculates the face value by summing the upstream value found by the linear interpolation of the gradients. The Venkatakrishnan limiter is implemented (Venkatakrishnan (1995); Zorzi et al. (2015)). Also, the momentum and the continuity equations are linked by a predictor-corrector SIMPLE. While the pressure-velocity incompatibility for the collocated variable arrangement is solved by the Rhie-Chow interpolation. Table 3.5. shows the different time steps used for the validation and initial velocity cases.

Table 3.5: Time steps simulation for validation and initial velocity case.

	Time(s)	Study
Fine	7.50E-04	Validation
Medium	1.00E-03	
Coarse	2.00E-03	
Medium	2.50E-04	Initial Velocity

3.4.7 Studies on Turbulence Model

Presently, one of the biggest problems in *CFD* is the correct prediction of the boundary layer and the transition flow (Gamboa (2010)). There are four types of turbulence models used: Spalart-Allmaras (Spalart and Allmaras (1992)), k-epsilon (Jones and Launder (1972)), k-Omega (Menter (1994)), Reynolds Stress Turbulence (Sarkar and Lakshmanan (1991)). The first three models are eddy viscosity models, and all the models use wall laws to calculate the boundary layer characteristics. The semi-empiric wall laws were developed assuming the flow is fully turbulent. However, some flows have a low Reynolds number, and there is a significant part of the boundary layer that is in the laminar regime. Therefore, predicting the results numerically can fail (Gamboa (2010)).

Rumsey and Spalart (2009) investigated the behaviour of widely used Spalart-Allmaras and Menter shear-stress transport turbulence models k-omega (SST) at

low Reynolds numbers, and under the condition of relaminarization, they used a *2D* zero-pressure-gradient flow over a flat plate from subsonic to hypersonic Mach numbers, *2D* airfoil flow from subsonic to supersonic Mach number, *2D* subsonic sink flow, and *3D* subsonic flow over an infinite swept wing. They concluded that these models are intended for fully turbulent high Reynolds number computations, so using them for transitional low Reynolds number or relaminarizing flow is not appropriate. Jones and Launder (1972) presented a new model of turbulence in which the local turbulence viscosity is determined from the solution of transport equations for turbulence kinetic energy and energy dissipation rate. The model is developed for regions where the Reynolds number is low and is applied to predict the boundary layer partially becoming a laminar region as it flows to the wall, in which longitudinal accelerations are so strong. Eça and Hoekstra (2008) studied the numerical calculation of the resistance coefficient of an infinitely thin plate as a function of Reynolds number using seven eddy-viscosity models, the one-equation models of Menter and Spalart-Allmaras; the two-equation model proposed by Wilcox (1998) turbulent/non-turbulent, baseline and shear-stress transport variant two-equation model. The study compares the numerical results with the ITTC (1957) line, Schoenherr Karl (1932) lines, and the lines suggested by Martín (1999) and Fonseca and Herrmann (2005). They concluded that none of the turbulence models selected are able to model the transition from laminar to turbulence, but the k-omega model shows better results. Firooz and Gadami (2006) investigated a turbulence flow around a two-dimensional wing at a different angle of attack near and far from the ground for fixed and moving ground conditions with Reynolds averaged Navier-Stokes equations, using a realisable k-epsilon model with enhanced wall treatment and the Spalart-Allmaras model, and concluded that both turbulence models have good agreement with the experimental data. Sørensen (2008) predicted the laminar to turbulence transition flow over airfoil and rotor and offers an alternative to the conventionally fully turbulence models. Gamboa (2010) investigated flow around a wing sail airfoil numerically by determining the best turbulent and

discretization model for the flow, which includes laminar and turbulent transition and also determined the numerical uncertainty using the grid convergence index, and concluded k-omega Gamma-Re-Theta model agreed well with the experimental results to predict both lift and drag coefficients. Jin and Xu (2008);Wu and Lin (2015);Zorzi et al. (2015) investigated the dynamics of a free-falling plate numerically and predicted the flow to be laminar.

Despite this, industrial engineers and academic researchers needed ways to simulate turbulent fluid flow to optimise the design for the real world. Various empirical or semi-derived turbulence models have been created to find the best model to fit experimental results. Prandtl. (1925) introduced the first turbulence model using the mixing length concept to compute the eddy viscosity. However, the model did not contain any partial differential equations *(PDEs)* and is therefore known as zero-equation or algebraic Terziev et al. (2019). In practice, an n-equation model refers to the number of additional PDEs introduced to close the Reynolds Average Navier-Stokes *(RANS)* equation (Wilcox (2006)). In addition, Prandtl. (1925) also created the one equation model using *PDE* to express the turbulent kinetic energy, k, thereby creating the first conceptual leap one equation turbulence model (Terziev et al. (2019)). Primarily, this allowed the local flow properties to be dependent on antecedent events. Driest (1956) later devised viscous damping by modifying the mixing length model, which has been virtually applied to all the algebraic closures since (Wilcox (2008)). Another zero-equation model is that of Baldwin and Lomax (1978).

This study compared the numerical results with the experimental data using the *k-ω (SST Gamma-Re-Theta variants)* and compared the results with experimental data of Andersen et al. (2005a) and the numerical results of Jin and Xu (2008).

As stated previously, the three turbulence models are eddy viscosity models often used in *CFD's* studies, while the last model is known as second-moment closure models and is considered to be one of the complex turbulence models in Star-CCM+ (Gamboa (2010)).

3.4.8 *k*-ω, two-equation model

The *k*-ω model is a two-equation model that is an alternative to the *k*-ϵ model. The transport equation solves the turbulence kinetic energy *k*, as the *k*-ω model and a quantity called ω, which is defined as the specific dissipation rate, that is, the dissipative rate per unit turbulent kinetic energy *(ω α ϵ/k)* in order to determine the turbulence eddy viscosity.

One advantage of the *k*-ω model over *k*-ω is its improved performance for boundary layers under adverse pressure gradients. Perhaps the most significant advantage is that it may be applied throughout the boundary layer, including the viscous-dominated region,without further modification. Furthermore, the standard *k*-ω model can be without requiring the computation of the wall distance.

There are mainly four model variants in STAR-CCM+: Standard *k*-ω, *SST* (Shear Stress Turbulence) *k*-ω, *SST k*-ω detached eddy model and finally the Gamma-Re-Theta. In this research, the *SST k*-ω variant Gamma-Re-Theta with low y^+ range of *1.4*, which solve the viscous sublayer at a low Reynolds number, will be used. For the model variants, the two transport equations are the same (Gamboa (2010)).

$$U_{\mathrm{x}}\frac{\delta k}{\delta x} + U_{\mathrm{y}}\frac{\delta k}{\delta y} = \nu_{\mathrm{t}}S^2 + \bigtriangledown \times \left[\left(\nu + \frac{\nu_{\mathrm{t}}}{\delta_{\mathrm{k}}}\right)\right] - \beta^*\omega k \tag{3.16}$$

$$U_{\mathrm{x}}\frac{\delta \omega}{\delta x} + U_{\mathrm{y}}\frac{\delta \omega}{\delta y} = \alpha S^2 + \bigtriangledown \times \left[\left(\nu + \frac{\nu_{\mathrm{t}}}{\delta_{\omega} \times \bigtriangledown}\right)\right] - \beta^*\omega^2 + F_{\omega}\frac{1}{\omega} \bigtriangledown k \times \bigtriangledown$$

ω (3.17)

Thus, even though the transportation equations remain the same for all the *k*-ω variants, the eddy viscosity term of the computation for the *SST* is calculated differently. The term is obtained with the following expressions:

$$\nu_{\mathrm{t}} = \frac{a_1 k}{max(a_1 \omega F_2 \Omega)} \tag{3.18}$$

Where $a_1 = 0.31$

$$F_2 = \tanh arg_2^2 \tag{3.19}$$

$$\tanh arg_2^2 = max\left(\frac{2\sqrt{k}}{0.09\omega d^2}, \frac{500\nu}{wd^2}\right) \tag{3.20}$$

With this constant: $\beta^* = 0.09$, $\beta_1 = 0.075$, $\beta_{k1} = \frac{1}{0.85}$, $\delta_{w1} = 2$, $\alpha_2 = 0.4404$, $\beta_2 = 0.082$ and $\delta_{k2} = 1.17$

The Gamma-Re-Theta transition model is a correlation-based transition model that is specifically formulated for unstructured *CFD's* codes. Evaluation of momentum thickness Reynolds number is avoided by relating this quantity to vorticity-based Reynolds number. In addition, a correlation for the transition onset momentum thickness Reynolds number defined in the free stream is propagated into the boundary layer by a transport equation. Also, an intermittency transport equation is further used in such a way that the source terms attempt to mimic the behaviour of algebraic engineering correlations.

The Gamma-Re-Theta model, as originally published, is incomplete since two critical correlations were claimed to be proprietary and hence omitted. One justification for the omission is that the model provides a ''Framework" for users to implement their correlations.

For the Gamma-Re-Theta simulation, all the numerical results obtained with the model using the F_{length} default correlations; $C_{a1} = 1$, $C_{a2} = 0.03$, $C_{e2} = 50$, $C_{\theta t} = 0.03$, $\delta_{\theta t} = 2$

The model constant values used for this research are the constants set as default values in (Siemens (2020)) and the numerical analysis of wing sail aerodynamics (Gamboa (2010)).

3.5 Non-Dimensional Parameters

Freely falling objects are characterised by six in the case of *2D* and seven in the case of *3D* dimensional parameters (Andersen et al. (2005a); Wang et al. (2013)), such as span length w, chord length c, thickness h, density of object ρ_s, the density of fluid ρ_f, the kinematic viscosity of the fluid v, and acceleration due to gravity g. The non-dimensional parameters are form as; thickness ratio β^*, aspect ratio γ^*, density ratio ϵ^*, the dimensionless moment of inertia I^*, Reynolds number Re and then non-dimensional velocity V^*. However, the non-dimensional moment of inertia is related to the density ratio and thickness ratio. We use the dimensional and non-dimensional parameters found in (Willmarth et al. (1964); Smith (1971); Field et al. (1997); Mahadevan et al. (1998); Jones and Shelley (2005); Jin and Xu (2008); Hirata et al. (2009); Wang et al. (2013); Andersen et al. (2005a,b)). In addition, the kinematic parameters are the descent angle θ, average translating velocity $\bar{V}$ and the average angular velocity $\overline{\omega}$. From the above, the parameters of density ratio, aspect ratio, and thickness ratio can be determined as follows:

$$\epsilon^* = \frac{\rho_\mathrm{s}}{\rho_\mathrm{f}} \tag{3.21}$$

$$\gamma^* = \frac{w}{h} \tag{3.22}$$

$$\beta^* = \frac{h}{w} \tag{3.23}$$

The dimensionless moment of inertia and the non-dimensional moment of inertia is determined as:

$$I^* = \frac{32l}{\pi\rho_\mathrm{f} l^4 w} = \frac{8\epsilon\beta(1+\beta^2)}{3\pi} \tag{3.24}$$

The moment of inertia is of a rectangular object is determined as:

$$I = \frac{ms(l^2 + h^2)}{12} \tag{3.25}$$

Where the mass of the object is defined as *ms*. The non-dimensional moment of inertia under a very low thickness ratio *($\beta \ll 1$)* can be reduced to:

$$I \approx \frac{8\epsilon\beta}{3\pi}\alpha\epsilon\beta \tag{3.26}$$

The value $\epsilon\ \beta$ is the modified Froude number introduced by Jones and Shelley (2005) and the square of the Froude number proposed by Belmonte et al. (1998).

To determine the *2D* terminal falling velocity V_T of an object, at intermediate *Re* is defined in Equation (3.27):

$$V_{\mathrm{T}} = \sqrt{(\rho_{\mathrm{s}}/\rho_{\mathrm{f}} - 1)hg} \tag{3.27}$$

The above equation for the terminal velocity is estimated by balancing the buoyancy-corrected gravity given as $(\rho_s$ - $\rho_f)lhg$ with quadratic drag of $\rho_f \mathrm{wcV_T}^2$

However, Smith (1971), Willmarth et al. (1964) and Andersen et al. (2005a) used the measured values of the average descent speed from the experiment to determine the Reynolds number *Re*. While the *2D* terminal Reynolds number Re_T based on terminal velocity V_T is defined by Wang et al. (2013).

Therefore, the Reynolds number and the terminal Reynolds number is determined as:

$$\mathrm{Re} = \frac{\bar{V}l}{\nu} \tag{3.28}$$

$$\mathrm{Re_T} = \frac{V_{\mathrm{T}}l}{\nu} \tag{3.29}$$

The present research will also follow the convention of Willmarth et al. (1964); Smith (1971); Andersen et al. (2005a) to determine the Reynolds number by using measured values of the average descent speed from the experiment.

In addition, the non-dimensional velocity is determined as Equation (3.30):

$$V^* = \frac{\bar{V}}{V_{\mathrm{T}}} \tag{3.30}$$

While the non-dimensional rotating frequency is determined as Equation (3.31):

$$f^* = \frac{\overline{\omega} l}{2\pi \bar{V}} \tag{3.31}$$

The non-dimensional time, x and y coordinate, force and torque are determined as:

$$T^* = t\frac{V}{I} \tag{3.32}$$

$$X^* = \frac{x}{l} \tag{3.33}$$

$$Y^* = \frac{y}{l} \tag{3.34}$$

$$F_*^i = \frac{F_{\mathrm{i}}}{m^* g} \tag{3.35}$$

$$M_*^i = \frac{M_{\mathrm{i}}}{m^* g l} \tag{3.36}$$

$$m^* = (\rho_{\mathrm{s}} - \rho_{\mathrm{f}}) l h \tag{3.37}$$

The lift and drag coefficient C_L, the drag coefficient C_D and the moment coefficient is determined as C_M are defined as:

$$C_{\mathrm{L}} = \frac{L}{\frac{1}{2}\rho_{\mathrm{f}} \bar{V}^2 l w} \tag{3.38}$$

$$C_{\mathrm{D}} = \frac{D}{\frac{1}{2}\rho_{\mathrm{f}}\bar{V}^2 l w} \tag{3.39}$$

$$C_{\mathrm{M}} = \frac{M}{\frac{1}{2}\rho_{\mathrm{f}}\bar{V}^2 l^2 w} \tag{3.40}$$

3.6 Brief Background Studies on Numerical Uncertainties

Due to the significant advancements in computational fluid dynamics and a continued increase in publications numerically, it is important to detect, estimate, and control the numerical uncertainties and errors during simulations. ''As the famous scientist Albert Einstein stated, as far as the laws of mathematics refer to reality, they are not certain, and as far as they are certain, they do not refer to reality." Our ability to accurately simulate complex fluid flow is limited by our mathematical and numerical approximations" (Freitas (2002)). The first conference on the turbulence boundary layer was held at Stanford to address numerical uncertainty and to identify the fundamental, predictive capabilities of *CFD* codes, and the meeting was sponsored by the mechanic's division of the USA Air Force Scientific Research (Kline et al. (1969)). At the same time, quality-control measures were issued in 1986 by (Roache et al. (1986)) and the first journal was published. However, to be effective in the design and analysis of engineering systems or scientific research, it is important to know the level of accuracy in each simulation, but unfortunately, it is not uncommon practise in both the engineering and scientific communities to estimate errors in numerical simulation. The perception is that estimating numerical errors is time-consuming and difficult, and the trends are more important than the magnitude of the results. As a result, the implementation of large-scale results based on inaccurate simulation in the engineering and scientific communities can be far more expensive (Freitas (2002)).

Freitas (2002), in his research on the issue of numerical uncertainty, pointed out that there are inherent inaccuracies in any numerical simulation of any continuum problem. The inherent inaccuracies are as a result of approximating a continuous system by a finite-length, discrete approximation. At the same time, this process is based on the idea that the size of the grid and the assumptions are measured by the conditions of consistency and convergence.

3.6.1 GCI Studies

Despite the potential offered by computational fluid dynamics software, there are some problems associated with it. First, the discretization of the continuum introduces numerical error, while the numerical turbulence models that solve the Navier-Stokes equation require experimental data in order to validate the numerical results. The errors can be minimised but require extra computational effort and money (Gamboa (2010)).

In numerical computing, typically, three distinct sources of error are defined. The first of these, termed modelling error, represents the difference between the exact solution of the governing equations and real fluid flows. Secondly, the iterative error, which results from the nonlinearity of the governing equations and the manner in which they are treated (Eca and Hoekstra (2014)). Finally, the discretisation error, which results due to the mapping of the continuous governing equations onto discrete nodes in space and/or time. This study will focus on the latter category of error by examining the solution from three distinct viewpoints.

The numerical uncertainty of the solution is determined by employing a variety of methods on different aspects of the numerical solution. Firstly, numerical uncertainties in "local" quantities are assessed, following the standard approach taken by the vast majority of researchers. To elaborate, the uncertainty of the numerically computed values of the translation and rotational velocities with varying grid and time spacing are predicted. Following this, the trajectory of the plate is examined in detail, and the uncertainty associated with its prediction is computed. Both of

the above parameters are compared against experimental data. Following this, the global descent point from the centre of mass of the plate is extracted at each point in time, equally spaced between the time the plate is released and the time the plate collides with the bottom boundary. At each time interval, the global centre of mass point is sampled and extracted for uncertainty analysis. Different sampling densities used for the tumbling case from the validation of experimental results of Andersen et al. (2005a) and numerical results of Jin and Xu (2008) are used for this work. This data is processed via the method of Phillips and Roy (2017) to determine the proximity to the asymptotic range at each time interval. The above procedure is applied to the trajectories and velocities. This is done in view of the fact that Terziev et al. (2020) found that different parameters within the computational domain may behave in different manners in relation to the asymptotic range. It is therefore worthwhile to explore any potential differences between the aforementioned parameters by examining their convergence properties.

The uncertainty analysis is centred on the Richardson Extrapolation *(RE)* (Richardson (1927)). However, *RE* gives a confidence level of only *50%*. For this reason, a variety of different methods are employed to predict the uncertainty with a *95%* confidence interval. Specifically, the Grid Convergence Index *(GCI)* method Roache (1998), as well as the approaches of Xing and Stern (2010), and Stern et al. (2001), hereafter referred to as the *FSRE* (Factors of safety for Richardson Extrapolation) and *CF* (Correction Factor) methods, respectively.

The aforementioned procedures begin by expanding the discretisation error (ϵ) for a particular grid size h as a Taylor series Equation (3.41):

$$\varepsilon = f_{ex} - f_1 = \sum_{p=p_f}^{\infty} \alpha h_{pf} = \alpha_{pf} h_{pf} + Higherorderterms \tag{3.41}$$

where f_{ex} is the exact solution, i.e. the solution for a grid size of $h = 0$, f_1 is the solution obtained on the grid of size h, is a constant, while p_f is the formal order of accuracy, $p_f = 2$. Here, the discretisation error is the difference of the exact, or extrapolated solution (f_{ex}) and the fine solution (f_1). Assuming that higher-order

terms in the Taylor series may be neglected, one may write Equation (3.42):

$$\varepsilon \approx \alpha_{pf} h_{pf} \tag{3.42}$$

Alternatively, the formal order of accuracy may be replaced by the observed order of accuracy *(p)* Equation (3.43):

$$p = \ln\left(\frac{f_3 - f_2}{f_2 - f_1}\right) / \ln r \tag{3.43}$$

where f_2, f_3 are the medium and coarse solutions, obtained by magnifying the grid size h by some constant cator $r \gg 1$. Then, the discretisation error becomes Equation (3.44):

$$\varepsilon(p) = (f_2 - f_1)/(r_p - 1) \tag{3.44}$$

$$U_{\mathrm{GCI}} = FS \times |\varepsilon(p)|/(rp - 1) \tag{3.45}$$

where U_{GCI} Is the uncertainty according to the Grid Convergence method, above the value of FS is typically set as $FS = 1.25$ provided three solutions are available (f_1, f_2, f_3). Alternatively, Stern et al. (2001) developed the correction factor approach *(CF)*, which modifies the error as Equation (3.46):

$$\varepsilon_{\mathrm{CF}} p = C \times (f_2 - f_1)/(r^{\mathrm{p}} - 1) \tag{3.46}$$

where $C = ((r^p - 1) / (r^{pf} - 1))$. The uncertainty according to the correction factor method U_{CF} then becomes Equation (3.47):

$$H\ U_{\mathrm{CF}} = \begin{cases} [9.6(1-C)^2 + 1.1] \times \varepsilon_{\mathrm{CF}} & \text{when} |1 - C| < 0.125 \\ [2[|1-C|] + 1] \times \varepsilon_{\mathrm{CF}} & \text{when} |1 - C| \geqslant 0.125 \end{cases}$$

A third approach was devised by Xing and Stern (2010), which uses the ratio of the observed and formal orders of accuracy *($P = Pp_f$)*. Based on the value of P, a new uncertainty estimate is arrived at *(U_{FSRE})* Equation (3.48):

$$U_{\mathrm{CF}} = \begin{cases} (16.4P - 14.8) \times |\varepsilon_{\mathrm{p}}| & \text{when} P > 1 \\ (2.45 - 0.85P) \times |\varepsilon_{\mathrm{p}}| & \text{otherwise} \geqslant 0.125 \end{cases}$$

These methods will be used to assess the numerical uncertainty of the present solutions in local terms. The latter are also considered through the approach of Phillips and Roy (2012), who presented a modification of the method of Cadafalch et al. (2002). In essence, this approach uses the solution field to determine a new factor of safety, based on the average distance to the asymptotic range, broadly defined as the formal order of accuracy, $p_f = 2$. The first step is to modify the observed order of accuracy to admit oscillatory solutions Equation (3.49):

$$p = \ln\left(\left|\frac{f_3 - f_2}{f_2 - f_1}\right|\right) / \ln r \tag{3.49}$$

Then, the local deviation from the formal order of accuracy δp is given as Equation (3.50):

$$\triangle p = \left[\frac{1}{N}\sum_{i=1}^{N} min(|p_f - p_i|, 4pf), 0.95p_f\right] \tag{3.50}$$

Where *(p_i)* is the (modified) observed order of accuracy at the node i. The final step is to determine the distance between δp and p_f, p_* Equation (3.51) and Equation (3.52).

$$p^* = p_f - \triangle p \tag{3.51}$$

$$FS(p_*) = \left[F_0 - (F_0 - F_1)\left(\frac{p_*}{p_f}\right)\right] \tag{3.52}$$

Then, the factor of safety as a function of $p*$ maybe expressed by: where $F_0 = 3$, and $F_1 = 1.1$. The uncertainty may be estimated by replacing the observed order of accuracy, p, in the GCI form.

3.7 Summary and Conclusions

This chapter describes the experimental, numerical, and uncertainty techniques, as well as the methodology and laboratory setup. The trajectories and orientations of different plates were investigated to determine the transition from zigzag to tumbling motions of freely falling heavy plates in three-dimensional viscous fluid. The plates varied in dimensions and densities, which resulted in both periodic and tumbling motion. The procedure for setting up the experiment was described in detail, where Oqus Qualisys cameras with makers of negligible mass were used to locate the centre of mass of the plate by estimating the trajectories and orientation. Each plate was dropped multiple times to capture the real-time six degrees of freedom in air and water by using the Qualisys camera, where the data was processed in order to estimate the trajectory and orientation. This resulted in the estimation of a mean path for each drop, where statistical methods were applied to find the 95% confidence interval of the mean. The bistability of resulting trajectories was investigated for each plate, by changing the initial angle of release.

Different numerical models used in simulating the dynamics of a falling body were discussed. To model the tumbling mode with high accuracy, overset mesh, also called Chimera or overlapping grids, was chosen for implementation, as this approach did not require re-meshing , nor did the quality of the mesh decrease since the body moves within the fluid domain unaltered. The basic theory behind a CFD-simulation was covered, along with the Transition SST-model used for turbulence modelling. Mesh and time-step independence studies were carried out in order to ensure independent results of the numerical model. Non-dimensional parameters of a freely falling object such as span length , chord length, thickness, density of object, the density of fluid, the kinematic viscosity of the fluid, and acceleration due

to gravity are discussed.

A brief background study on numerical uncertainty in computational fluid dynamics is discussed, since the discretization of the continuum introduces numerical error, while the numerical turbulence models that solve the Navier-Stokes equation require experimental data in order to validate the numerical results. The numerical uncertainty of the solution is determined by employing a variety of methods on different aspects of the numerical solution. Firstly, numerical uncertainties in local quantities are assessed, following the standard approach taken by the vast majority of researchers. However, the uncertainty of the numerically computed values of the trajectories, translation, and rotational velocities with varying grid and time spacing is discussed.

Chapter 4

EXPERIMENTAL STUDY ON FALLING PLATE PROBLEM

This chapter experimentally examines the sensitivity of the initial angle of release, with experimental results and phase diagrams showing the transition and bistability between a zigzag motion to tumbling of the free-falling heavy rectangular plate in air and water.

4.1 Sensitivity to Initial Orientation

Initial conditions strongly affect the dynamic process of the transition from one state to another in the motion of a freely falling plate. However, transitions and instabilities are unresolved problems in fluid mechanics and are always directly related to the evolution of the disturbance (Lee et al. (2013)). In the case of a falling thin rectangular plate, Andersen et al. (2005a) show that initial conditions have significant importance in the case of apparent chaotic motion. While Lau et al. (2018) show the effect of initial conditions on the motion of a heavy rectangular plate freely falling, the motion changes from stable to tumbling as the angle of release changes. In the case of freely falling discs, initial conditions are important for the transition from zigzag to spiral (Lee et al. (2013)). Since experimental investigation on heavy plates at large, I^* remain sparse, the transition from stable falling to tumbling needs to be investigated. As a result, this study builds on the previous work of Lau et al.

(2018).

4.2 Trajectories

Flow instability is related to Re and I^* in the general problem of $2D$ freely falling rectangular plate (Andersen et al. (2005a)), or cylinder (Mathai et al. (2017)), and $3D$ disc (Auguste et al. (2013)). This research considers the dynamics of a heavy plate freely falling since the coupling interaction of a heavy plate freely falling appears to be wobbling (Lau et al. (2018)). Apart from the three dimensionless parameters Re, I^* and β^*, the initial release angle, translational velocity, and angular speed also influence the falling dynamic (Wu and Lin (2015)). From Table 4.1 to Table 4.9, various plates are shown with different Re, I^*, β^*, and θ.

4.2.1 Stable Falling Motion

When a heavy plate falls freely, wakes are formed at the tips and behind the plate. With lighter plates, the forces generated by the wakes begin to induce oscillation on the plate but will have negligible influence on the dynamics of the body (Lau et al. (2018)). Steady falling plates look like a needle falling in honey with small oscillation angles and almost fall straight downward, but sometimes it falls steadily with small oscillation due to vortex shedding and the dynamic occurs in smaller $Re \leq 50\sim 100$ (Wu and Lin (2015)).

4.2.2 Fluttering Motion

The periodic motion of fluttering freely-falling plate is complex, the motion usually occurs at large $Re > 200$ and small $I^* < 0.12$ (Wu and Lin (2015)). While Zigzag motion is common for freely falling bodies, in previous studies zigzag motion, occurred at $Re \sim 150$ and I^* range from 10^{-3} to 10^{-1}. Often, a vertical descending disc will periodically oscillate with altitude of variations, but there are still no detailed measurements of the six degrees of freedom(Lee et al. (2013)).

4.3 Phase Diagrams

The trajectories of falling objects can be represented in a phase diagram depending on *Re*, I^*, m^*, ρ^*, and β^*. Smith (1971) for the first time plotted a phase diagram for a rectangular plate with different β^* from *0.2* to *0.04* and confirmed with *Re* the plate falls steadily without any periodic motion, depending on I^* and at higher *Re* the plate flutters and tumble. However, at I^* less than *0.1* and even with higher *Re* exhibiting fluttering without any tumbling. Belmonte et al. (1998) found that at a critical value of $I^* = 0.4$ a transition will occur, and the plate motion will change from fluttering to tumbling. In a quasi-two-dimensional experiment by Andersen et al. (2005a) rectangular plates with different β^* and I^* exhibits different behaviour, from the experiment a plate will flutter at $I^* = 0.16$ and $\beta^* = 1/14$ and tumble at $I^* = 0.29$ and $\beta^* = 1/8$, in addition to tumbling and fluttering chaotic behaviour was added for the first time at $I^* = 0.39$ and $\beta^* = 1/6$, but confirmed the chaotic behavior due to laboratory noise. Wu and Lin (2015) numerically investigated the dynamics of a falling ellipse at a fixed aspect ratio and plotted the falling styles of steady, fluttering, tumbling, chaotic, and a transition between fluttering and tumbling using *Re and* I^*. For the first time Lau et al. (2018) investigated numerically the dynamics of heavy plates with *Re* up to *500* and I^* up to *10* and extended the phase plot from thin rectangular plates to heavy plates.

4.4 Experimental Uncertainty Determination

In most experiments, certain quantities are measured before determining other values based on the measured data. The first step in assessing an experiment's dependability is to assess the measurement uncertainties associated with each measured quantity. Measuring uncertainty is usually caused by the tools used, but it can also be caused by the experimenter's limitations or randomness in the effect being studied.

Figure 4.1 shows the fifteen experimental results of freely falling plates in-air to be very similar. There are, however, some trajectories that deviate significantly from the mean trajectory. Statistical measures can be used to quantify the difference between the different free falls.

In the dynamics of freely falling plates, the total uncertainty of the trajectory is projected to rise with time due to the time-dependent motion of the freely falling plate. Limits corresponding to *95%* confidence intervals are of importance for quantifying the variance between the recorded trajectories and the orientations. Equation (4.1) gives the limits to be calculated, where $\bar{x}$ is the sample mean value, n is the number of samples equal to *10* for an in-air drop and *5* for an underwater drop, s is the sample standard deviation, and $t/2$ is the critical value of the t-distribution. However, the t-distribution is used instead of the normal distribution because of the sample sizes.

$$\bar{x} - t_{\alpha/2}\frac{s}{\sqrt{n}} < x_0 < \bar{x} + t_{\alpha/2}\frac{s}{\sqrt{n}} \tag{4.1}$$

where:

$$\bar{x} = \frac{1}{N}\sum_{i=1}^{n} x_i \tag{4.2}$$

$$s = \sqrt{\frac{1}{n-1}\sum_{i=1}^{n}(x_i - \bar{x})^2} \tag{4.3}$$

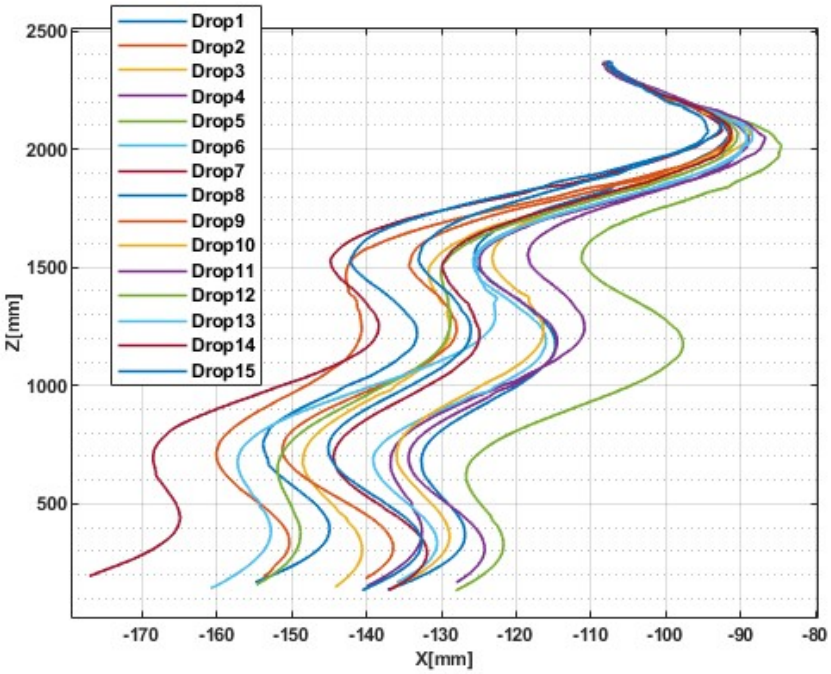

Figure 4.1: Experimental results showing trajectories

The results presented in Figure 4.2 and Figure 4.3 shows the calculated sample mean and the *95%* confidence interval of trajectory and orientation. The results show that the *95%* confidence interval increases with time as expected. Even though some of the trajectories presented in Figure 4.1 differ, the experiments generally show the same trajectory.

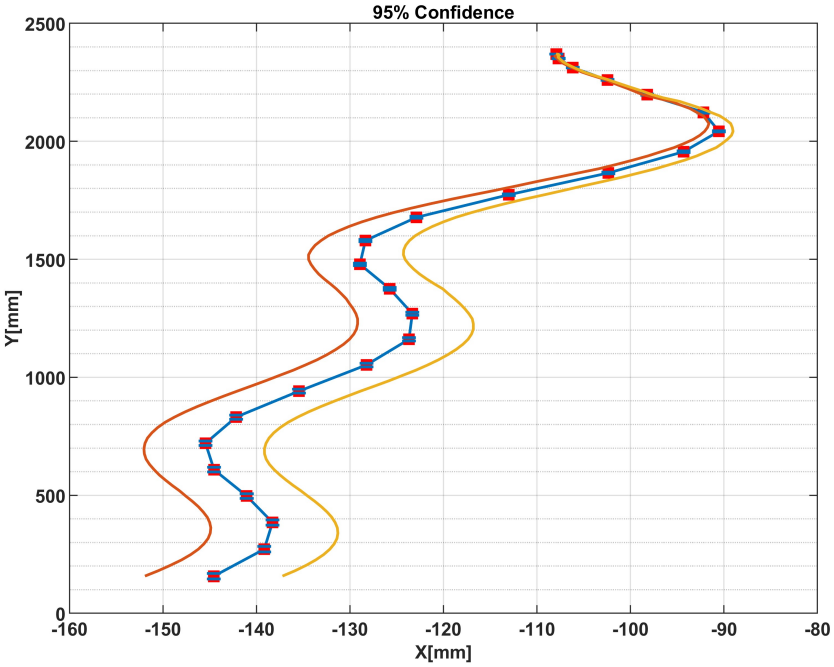

((a))

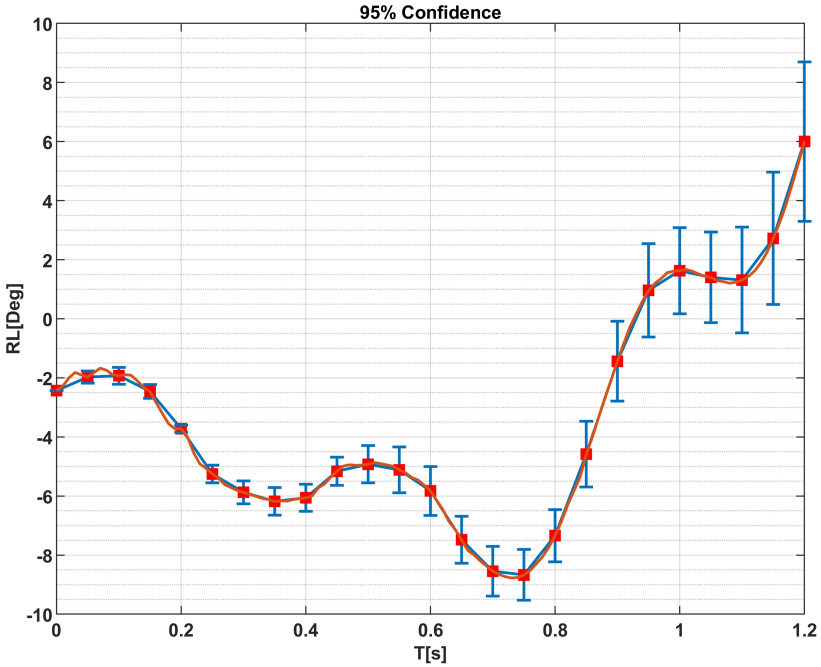

((b))

Figure 4.2: (a) Experimental results showing the *95%* confidence interval of (a) trajectories (b) orientation Roll

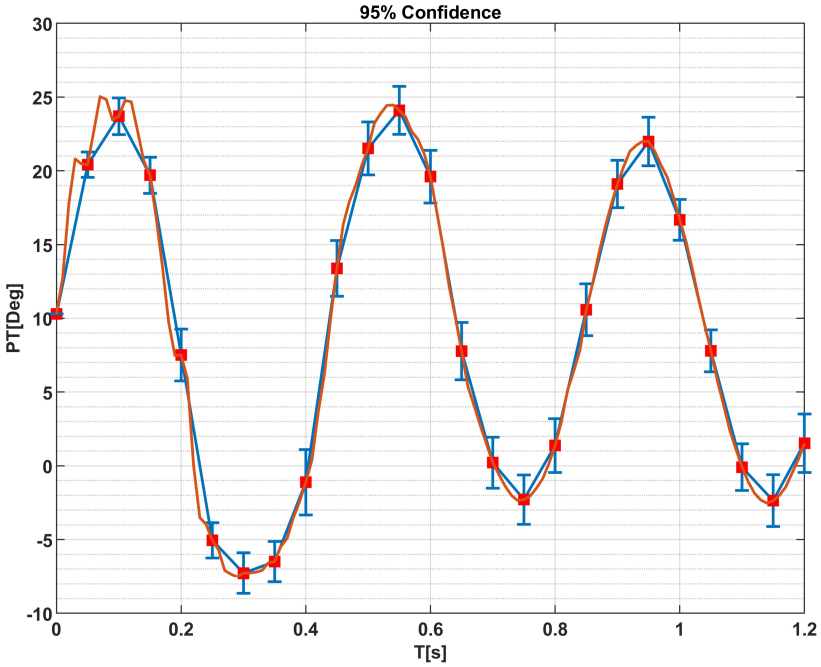

((a))

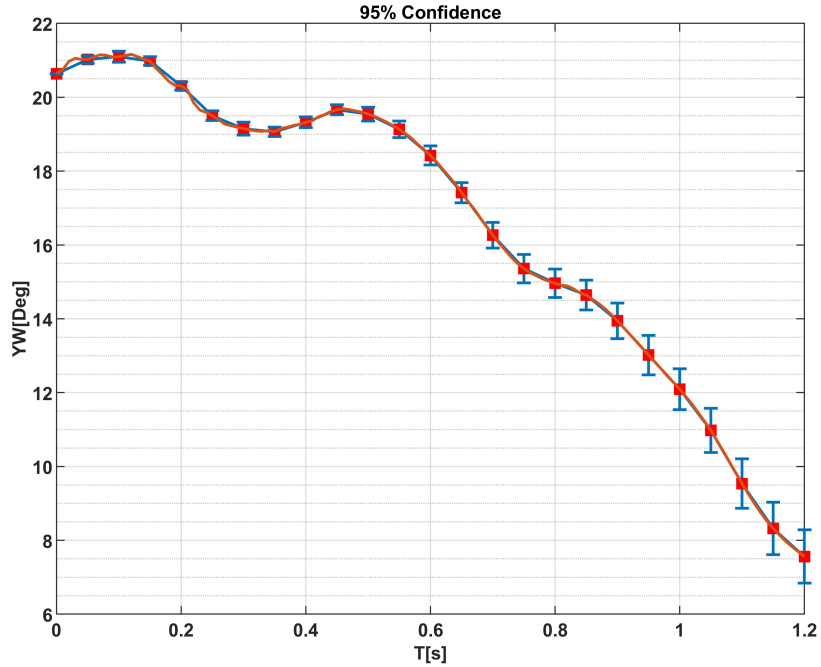

((b))

Figure 4.3: Experimental results showing the *95%* confidence interval of orientation (a) pitch (b) yaw

4.5 Results and Discussions

In this section, the experimental results are presented, showing the effect of release angle on the dynamics of a freely falling heavy plate in a three-dimensional viscous fluid. The experiment was performed with a range of Reynolds numbers $Re \sim 22000$ and a non-dimensionless moment of inertia up to 23 as shown in Table 4.1 to Table 4.9 with different release angles. The results show zigzag, fluttering and tumbling case as analysed with phase diagram from the different vertical falling velocities as shown.

4.5.1 Underwater Case

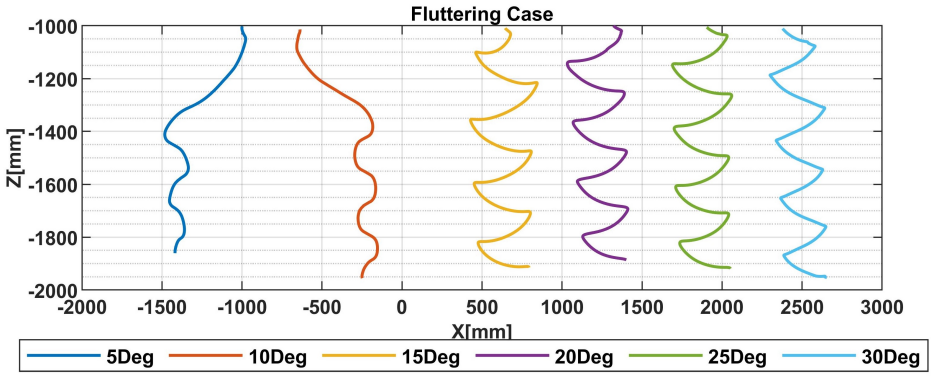

Figure 4.4: Trajectories of underwater fluttering plate at angles of 5^0 to 30^0 with different interval of 5^0 and show how oscillations vary with angle.

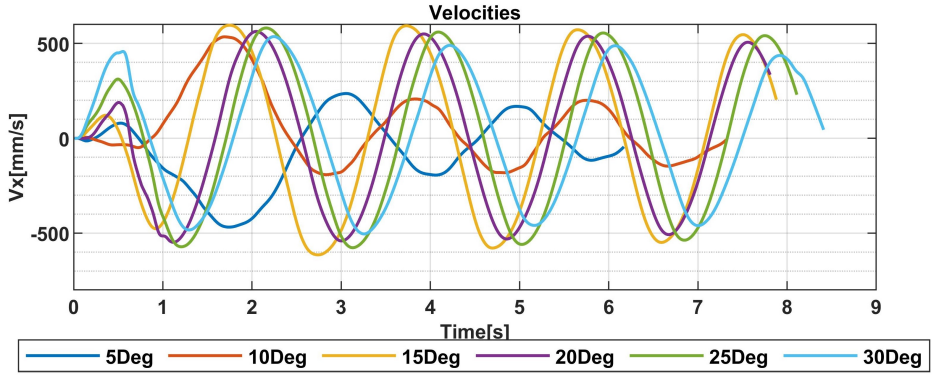

Figure 4.5: Horizontal velocity *(Vx)* of underwater fluttering plate at angles of 5^0 to 30^0 with different interval of 5^0 and show how oscillations vary with angle.

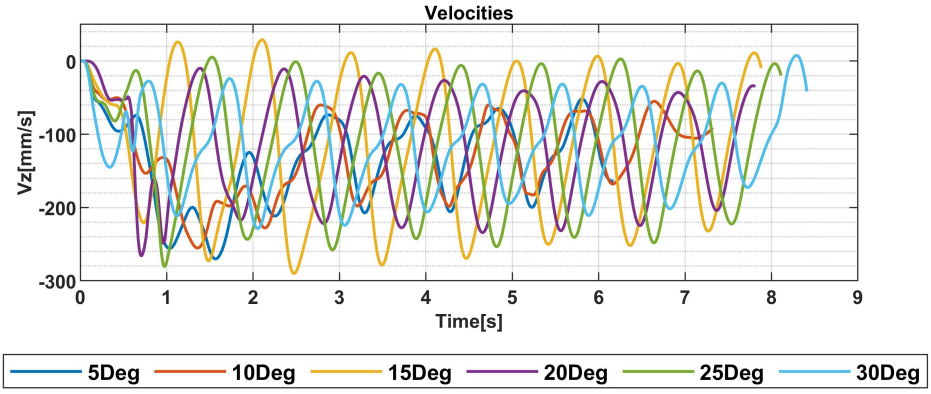

Figure 4.6: Vertical velocities (Vz) of underwater fluttering plate at angles of 5^0 to 30^0 with different interval of 5^0 and show how oscillations vary with angle.

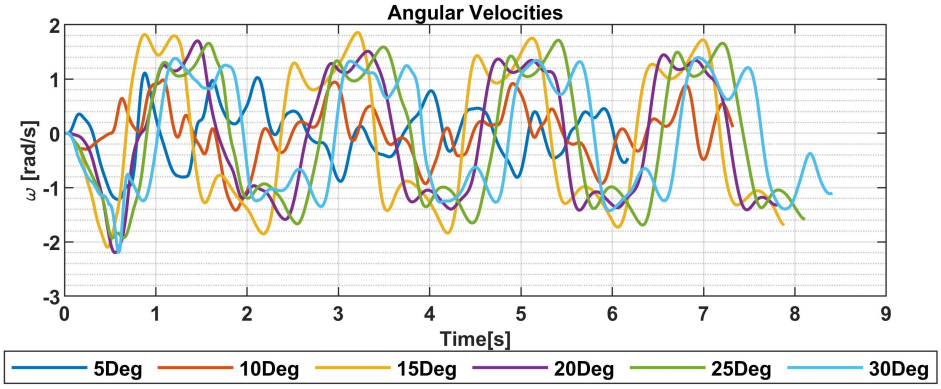

Figure 4.7: Rotational velocities *(ω)* of underwater fluttering plate at angles of 5^0 to 30^0 with different interval of 5^0 and show how oscillations vary with angle.

Table 4.1: A1 & A2 measured average horizontal velocities(Vx), vertical velocities (Vz), and angular velocity, (ω) underwater drop.

	Drop Angle (Deg)	Vx(mm/s)	Vz(mm/s)	$\omega(rad/s)$	I^*	Re
A1	5	153.19	-136.80	0.41	0.058	1230
	10	145.49	-127.60	0.36	0.058	1147
	15	350.62	-114.49	1.17	0.058	1029
	20	324.72	-113.17	1.02	0.058	1018
	25	344.72	-112.14	1.10	0.058	1010
	30	294.24	-111.60	0.96	0.058	1003
A2	0	189.13	-160.00	5.75	0.32	270

Figure 4.4 shows the trajectories of the fluttering behaviour of plates dropped at different initial angles, while Figure 4.5 to Figure 4.7 show the horizontal, vertical, and rotational velocities. The results above show a large oscillation angle, this type of motion often happens at a smaller dimensionless moment of inertia, $I^* < 0.12$ and a large Reynolds number, $Re > 200$ as shown in Table 4.1 and also reported by Wu and Lin (2015). When the plate release angle increases from 5^0 - 30^0 the periodic oscillation amplitude of the horizontal velocity increases nearly twice as much, as shown in Figure 4.5 and Table 4.1. However, the vertical velocity decreases as the initial angle of release increases and produces different average falling velocities, as shown in Figure 4.6 and Table 4.1. As the plate flutters side-to-side periodically when it descends, with alternating gliding at a low angle of attack and fast rotational motion at the turning point shown from Figure 4.7, the motion of the plate reaches its extreme maximum incline angle as the angular velocity equals zero; it was found that as the release angle increases, the Reynolds number Re reduces, showing a linear relationship between θ drop and Re shown in Table 4.1. A pure planar zigzag–fluttering motion was also observed from Figure 4.4 at 5^0 -

10^0 initial drop angle. The plate glides with an initial long gliding up to $1.4m$ drop length, before translating to a pure zigzag motion. The long gliding disappears as the angle of release increases above 10^0, a similar gliding was reported by Heisinger et al. (2014), as a coin falls in water. Furthermore, as the release angle increases from 30^0 bistability occurs and the fluttering motion changes to tumbling, but the tumbling motion was not reported as the motion of the plate moved out of the area of interest. Therefore, the experimental setup needed more cameras *6-8* to capture the tumbling motion above 30^0 release angles. Therefore the current results did not present the motion of tumbling plate for the above studies.

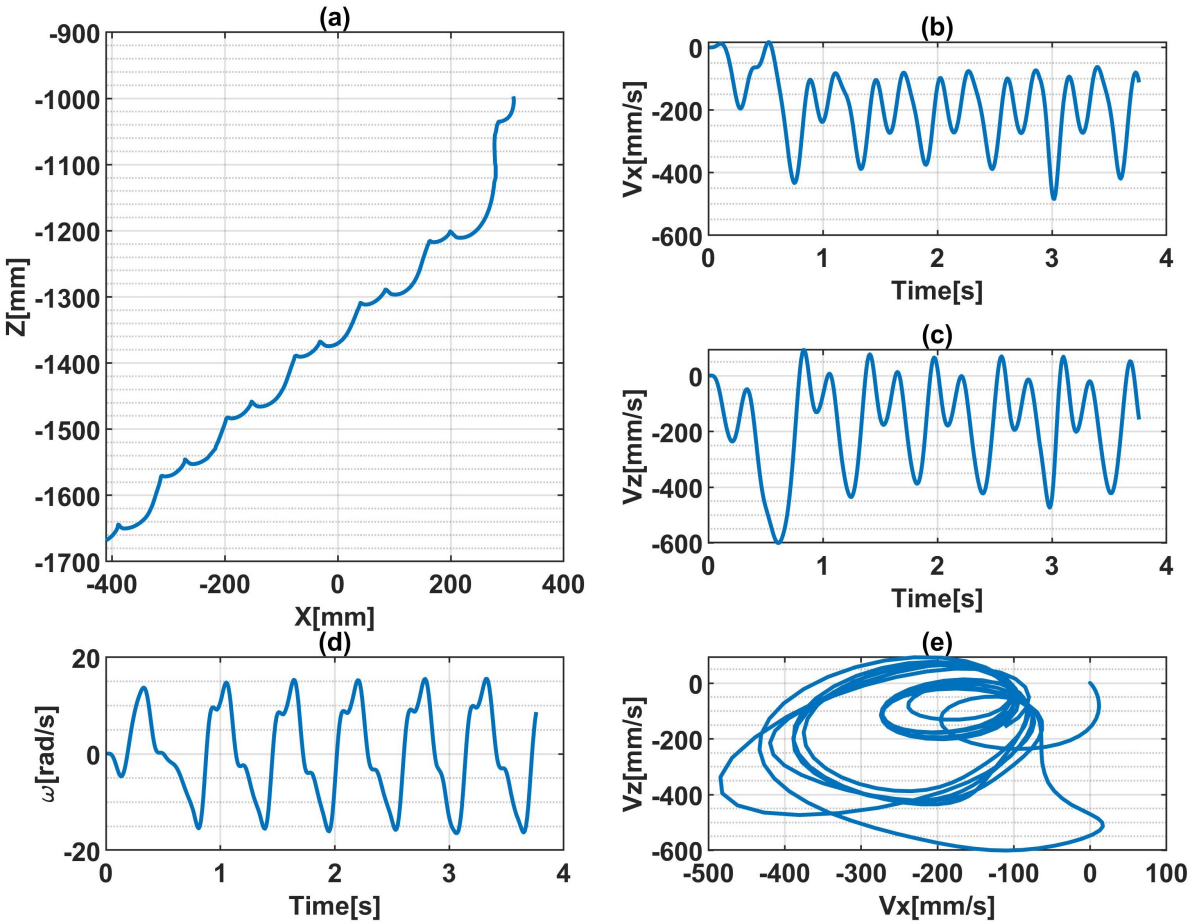

Figure 4.8: Measured plate trajectory:(a), horizontal velocity:(b), vertical velocity:(c), angular velocity:(d), and phase plot:(e) of underwater tumbling plate at angles of 0^0

Figure 4.8 shows the trajectory and velocity components as a function of time for the tumbling plate released at 0^0 angle with the horizontal. Tumbling motion

occurs at large dimensionless moments of inertia, $I^* \geq 0.35$ and large Reynolds numbers, $Re \geq 200$, and sometimes it occurs at the initial angle of release (Lau et al. (2018)) and chaotic regime (Wu and Lin (2015)). Experimental findings with falling discs suggest that tumbling motions are found at $I^* = 102$ (Heisinger et al. (2014)), whereas the results with fixed autorotating tumbling motion of flat plates at $I^* = 101$ (Smith (1971)). However, in this current research, a tumbling motion was observed at a dimensionless moment of inertia, $I^* \leq 0.35$ with Reynolds number $Re = 270$, as shown in Table 4.1. The periodic motion of the tumbling plate alternates between short and long gliding segments, with a more pronounced double tumbling period-two structure but with less angular velocity as compared to Andersen et al. (2005a) tumbling plate. The tumbling plate rotates slowly with angular velocity up to $15\ rad/s$ as shown in Figure 4.8 with the centre of mass elevating following long gliding, but it elevates with short gliding segments with the vertical velocity. The tumbling motion shows unequal translational distances between adjacent rotations as the plate tumbles down. Andersen et al. (2005a) and Wang et al. (2013) were the first to report the period-two tumble motion. Andersen et al. (2005a) reported the double period-tumble motion for large aspect ratio $\lambda > 15$, small dimensionless inertia $I^* < 0.5$ and Reynolds numbers $Re = 737$ which is composed of a sliding phase with a fast rotational phase. While Wang et al. (2013) reported period-tumble rotations for some range of aspect ratio and double frequency was observed from Fourier analysis. However, a period to tumble motion was observed at $I^* = 0.3$ and $Re = 270$ in the present research, which is less than what was reported by Andersen et al. (2005a) and Wang et al. (2013). Similarly, the difference between the two modes of fluttering Figure 4.4 and tumbling Figure 4.8 (a) are; fluttering plate periodically changes its rotational directions and has a cumulative rotational angle less than 180^0 while tumbling plate rotates 360^0 in whole period. Moreover, the influence of different initial release angles on the average descent horizontal, vertical, and rotational velocities with dimensionless moment inertia and Reynolds number is not recorded for angles above 0^0 due to the limitations of the experimental

setup.

4.5.2 In-Air Case

The trajectories of a falling plate in Figure 4.9 show a clear periodic zigzag motion, similar to the motion observed by Ellingsen and Risso (2001) for a rising air bubble in still water and Horowitz and Williamson (2010) motion of rising or falling spheres. Similarly, Horowitz and Williamson (2010) separated the motion of rising or falling spheres into vibration (flutter or wobble) and rectilinear (vertical) motion, while Lau et al. (2018) distinguished wobbling from flutter in terms of lift. However, when the vertical velocity *(Vy)* and the rotational velocity *(Pitch)* increase from different release angles as shown in Table 4.2 the wobbling motion also increases periodically and vigorously in a zigzag trajectory within a vertical plane with a large amplitude. Horowitz and Williamson (2010, 2008) linked these oscillatory motions to the periodic vortex shedding of the sphere as it rises.

Table 4.2: A1 measured average horizontal velocities(Vx), vertical velocities (Vy), and angular velocities (pitch) in-air drop.

	Drop Angle (Deg)	Vx(mm/s)	Vy(mm/s)	Pitch(rad/s)	I^*	Re
A1	0	71.32	-1659.72	2.03	7.51	6129
	5	68.56	-1716.35	1.82	7.51	6129
	10	61.39	-1598.76	1.69	7.51	6129
	15	143.31	-1674.43	2.94	7.51	6129
	20	172.24	-1707.34	3.59	7.51	6129
	25	27.07	-1814.45	5.68	7.51	6129
	30	230.62	-1752.32	4.87	7.51	6129
	35	259.28	-1766.99	5.64	7.51	6129
	40	232.05	-1776.28	4.80	7.51	6129
	45	277.05	-1836.63	6.27	7.51	6129

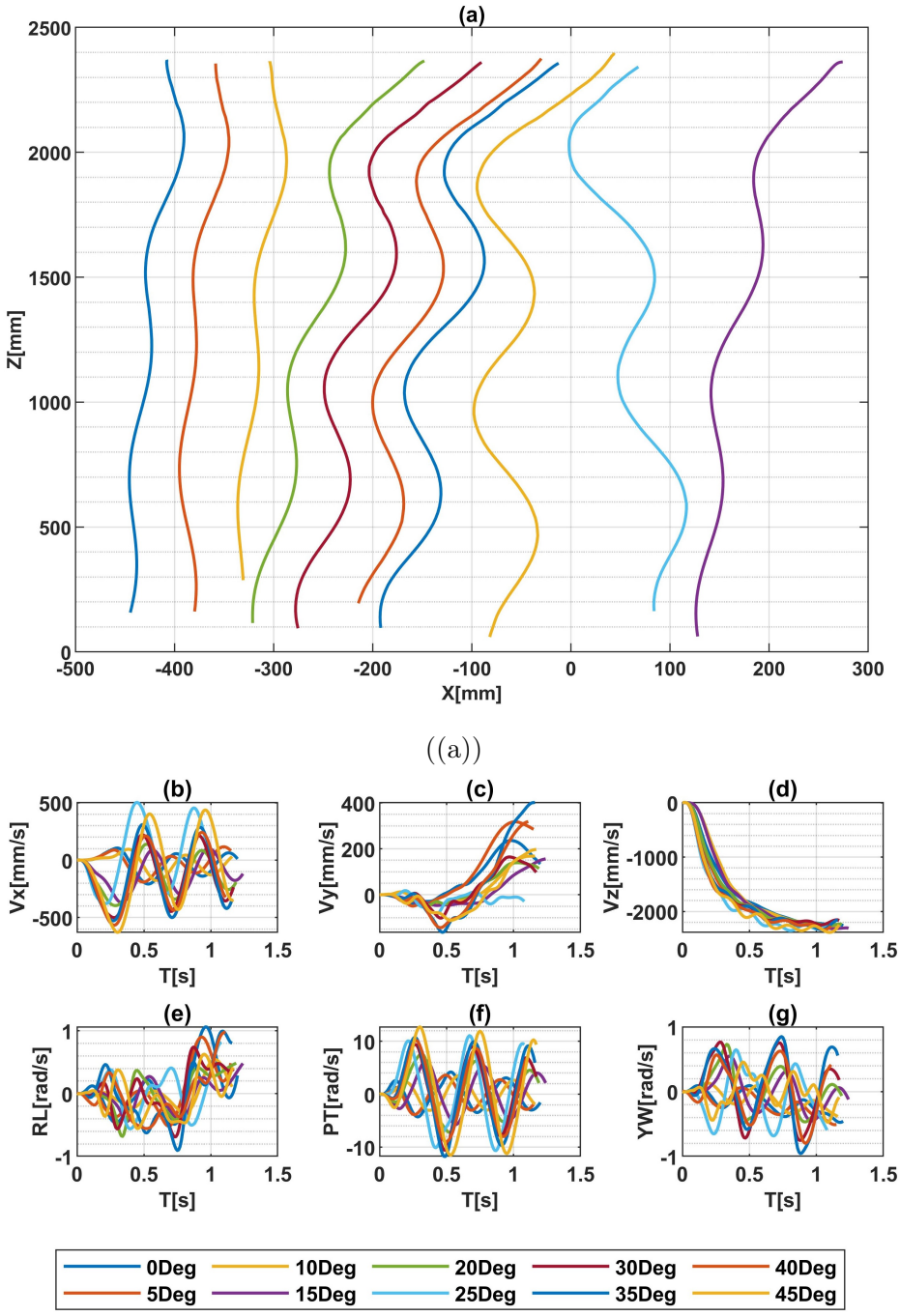

((a))

((b))

Figure 4.9: A1 Different measured plate trajectories:(a), Time histories of translational velocities:(b,c,d), rotational velocities:(e,f,g) of in-air zigzag plate at angles of 0^0 to 45^0 with different interval of 5^0 and showing how oscillations vary with different drop angle.

The trajectories shown in Figure 4.9 are for different release angle of 0^0 - 45^0 they all exhibit the same resulting zigzag motion but tumble as the angle increases above 45^0 showing the transition from zigzag to tumbling motion. Thus, tumbling motion

results are not reported in the current research. Both translational and rotational velocities in Figure 4.9 shows the motion to be extremely periodic as shown from the measured time histories but with slightly constant *Re and* I^*. The vertical velocity as shown in Table 4.2 to Table 4.9 changes but is not dependent on the angle of release, with horizontal velocity increasing but dropping at 25^0 release angles. Lau et al. (2018) reported a change in *Re and* I^* when the angle of release changes, with vertical velocity increasing as the angle of release increases.

Table 4.3: C1 measured average horizontal velocities (Vx), vertical velocities (Vy), and angular velocities (pitch) in-air drop.

	Drop Angle (Deg)	Vx(mm/s)	Vy(mm/s)	Pitch(rad/s)	I^*	Re
C1	0	47.00	-1701.87	3.37	23.33	2127
	5	53.37	-1706.10	3.27	23.33	2133
	10	69.00	-1700.71	4.82	23.33	2126
	15	78.46	-1659.26	4.98	23.33	2074
	20	117.95	-1711.37	7.75	23.33	2139

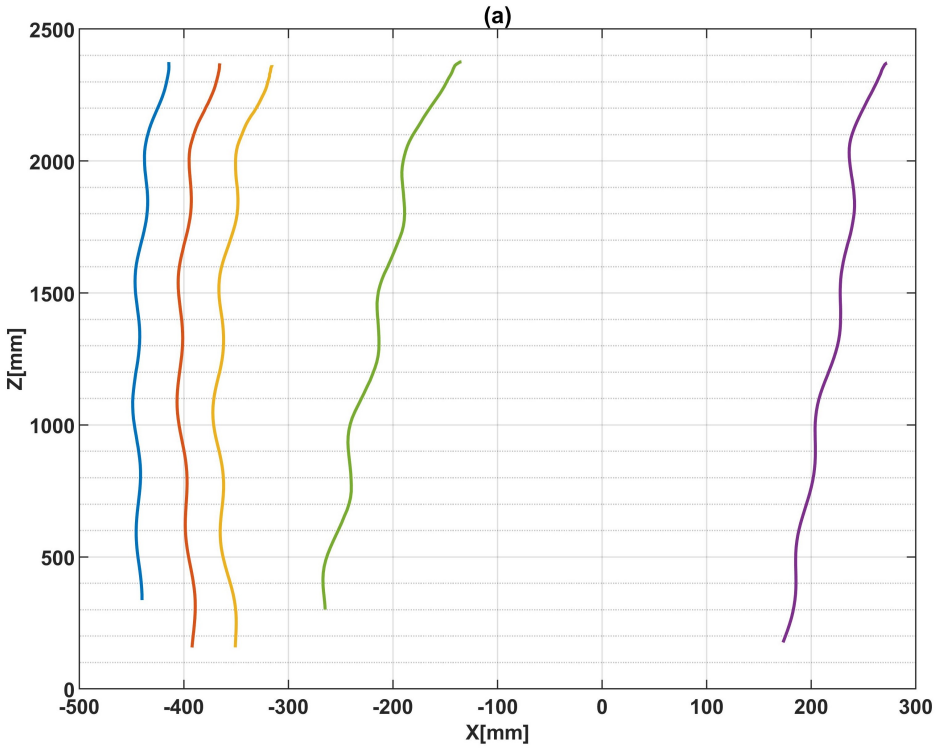

((a))

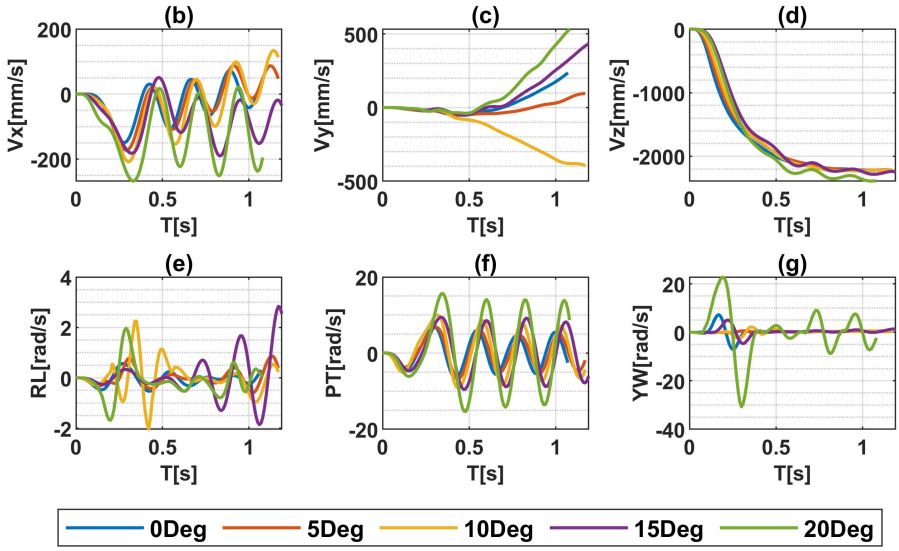

((b))

Figure 4.10: C1 Different Measured plate trajectories:(a), Time histories of translational velocities:(b,c,d), rotational velocities:(e,f,g) of in-air zigzag plate at angles of 0^0 to 20^0 with different interval of 5^0 and showing how oscillations vary with different drop angle.

Table 4.4: A2 measured average horizontal velocities (Vx), vertical velocities (Vy), and angular velocities (pitch) in-air drop.

	Drop Angle (Deg)	Vx(mm/s)	Vy(mm/s)	Pitch(rad/s)	I^*	Re
A2	0	89.57	-1634.45	1.80	5.19	8853
	5	72.23	-1637.54	1.65	5.19	8870
	10	90.40	-1638.53	1.82	5.19	8875
	15	93.39	-1521.46	1.84	5.19	8241
	20	89.27	-1613.73	1.72	5.19	8741
	25	131.10	-1633.00	2.63	5.19	8845
	30	135.33	-1540.32	2.40	5.19	8343

Zigzag motion is common for freely falling bodies. Previous studies showed that zigzagging occurs for thin discs when the Reynolds number $Re \quad 150$ and the dimensionless moment is in the range from $I^* = 10^{-3}$ - 10^{-1} (Zhong et al. (2013)). However, flat bodies are known to present far more spectacular path instabilities than spheres or discs; furthermore, path instabilities have much larger effects on the dynamics of flat bodies than spheres; in many experimental studies of disc or sphere, aspect ratios of approximately 10 are considered to represent flat bodies (Zhou et al. (2017)). Figure 4.13 and Figure 4.14 show a flat plate falling with different angles of release. The trajectories of the falling plate observed are periodic with oscillatory planar zigzag motion, I^* was same for same aspect ratio, but Re differs at different drop angles as shown in Table 4.1 to Table 4.9, the amplitude of the horizontal displacement increases with Re as shown in Table 4.7 to Table 4.9. After initial transient, the body's periodic trajectory is practically vertical, while the horizontal drift is less than 7 rad as shown in Figure 4.13 and Figure 4.14, and the angular velocity of the zigzag plane's in Figure 4.4 to Figure 4.14 showing a potential rotation that is more than 10 - 80 times lower than the major oscillation frequency. As the Reynolds number Re is increased to maximum in Figure 4.14 the frequency and pattern of oscillation increase, but with high lift as compared

to the stable motion of Lau et al. (2018) and Willmarth et al. (1964). They both classified the wobbling rectilinear motion as stable falling and distinguished it from flutter in terms of lift, however, due to the increase in lift as shown in Figure 4.10, Figure 4.13 and Figure 4.14. The research studies considered the trajectories as periodic zigzag motion, similar to motions reported by Fernandes et al. (2005); Horowitz and Williamson (2008, 2010); Filella et al. (2015) as the inclination of the axis and velocity of oscillation are almost in phase, but the results shown in Figure 4.11(a) and Figure 4.12(a) show the inclination of the axis and velocity of oscillation to be out of phase. At a higher Reynolds number, the amplitude of the transitional motion increased. These properties of zigzag motion are similar to those in the cases of Belmonte et al. (1998) and Andersen et al. (2005a) where the amplitude of oscillation increases as I^* becomes larger.

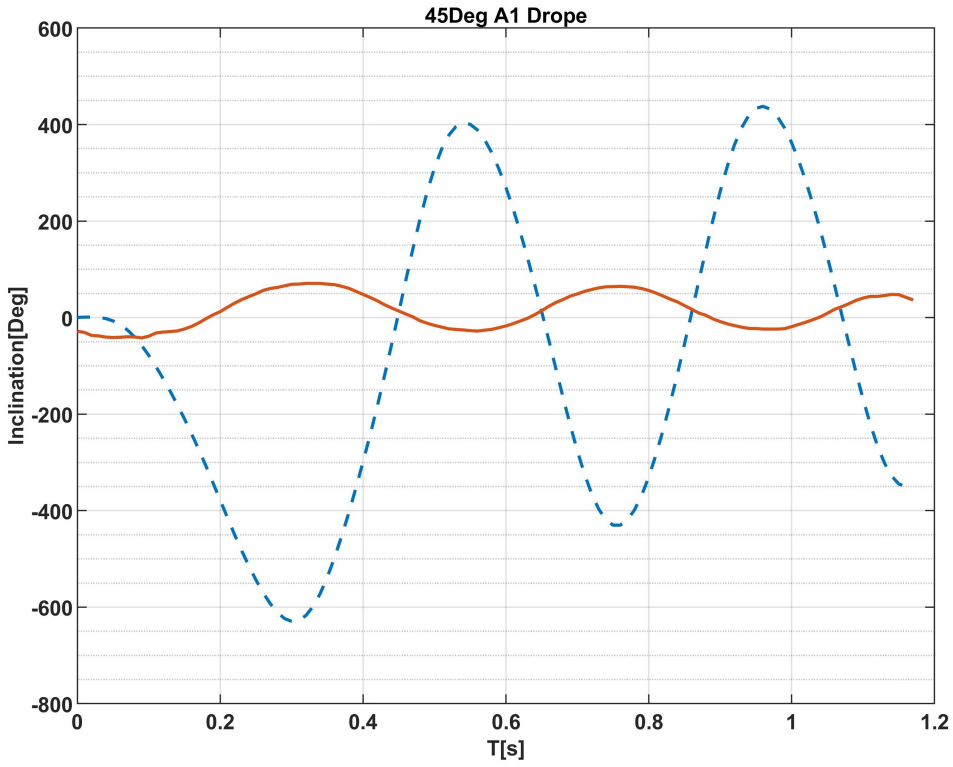

((a))

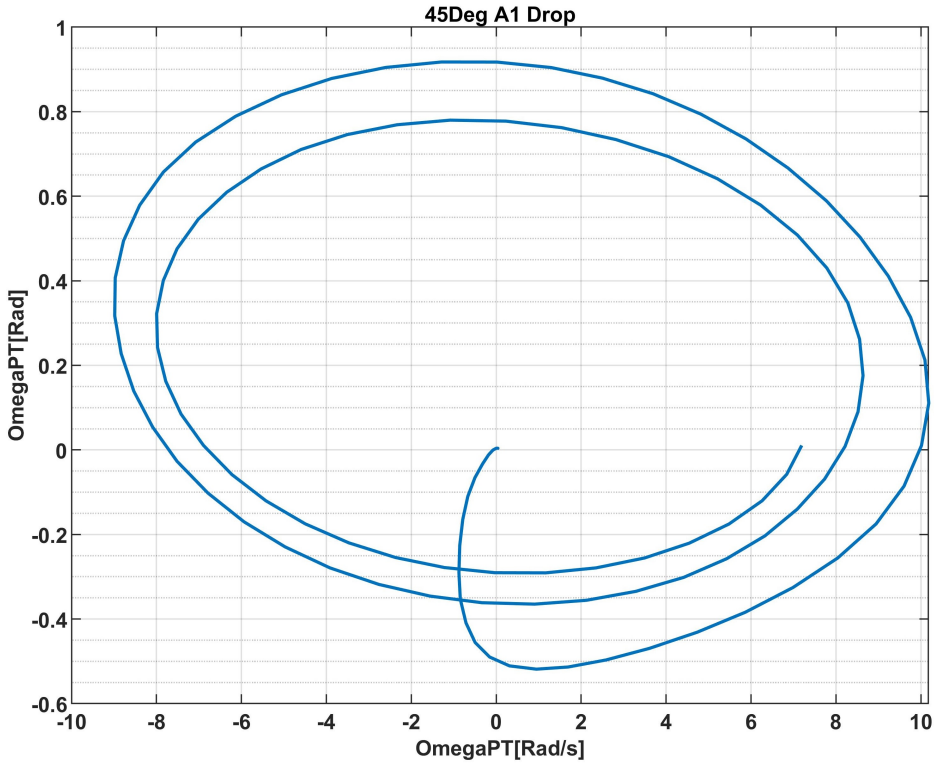

((b))

Figure 4.11: A1 (a) temporal evolutions of the inclination angles with respect to the Horizontal Velocity (b) phase portraits showing different trajectories

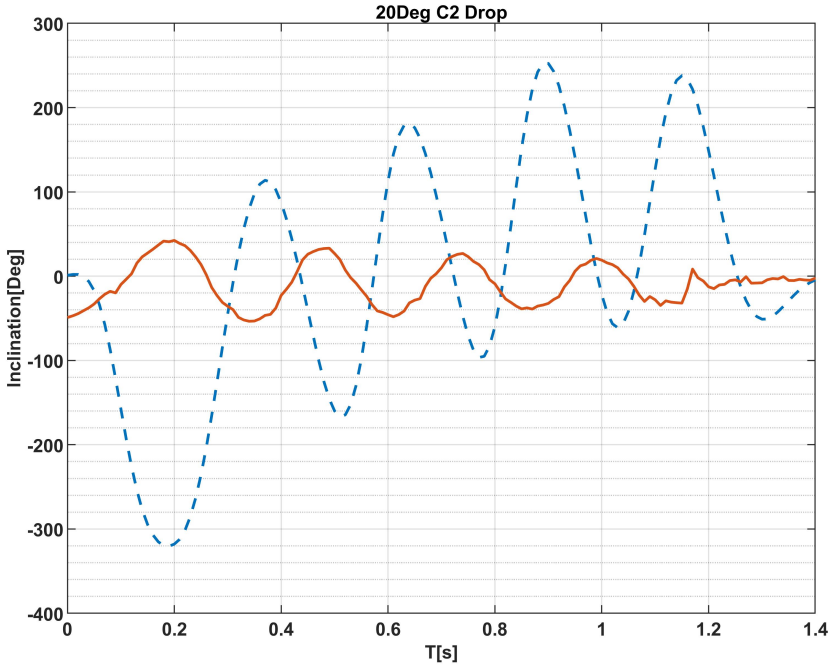

((a))

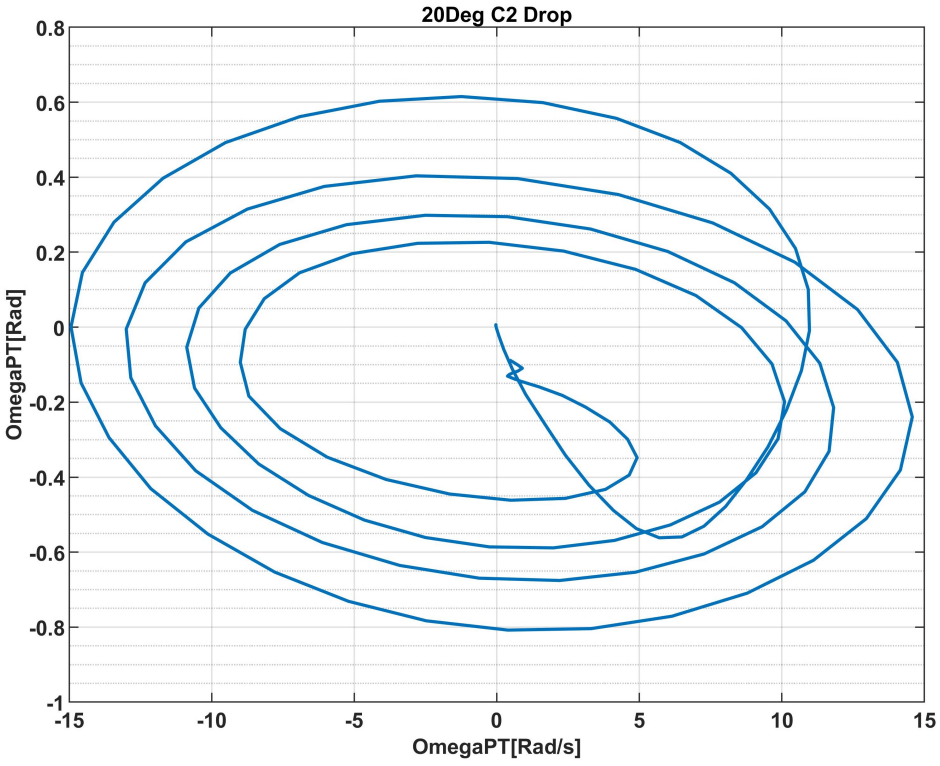

((b))

Figure 4.12: C2 (a) temporal evolution of the inclination angles with respect to the Horizontal Velocity (b) phase portraits showing different trajectories. showing how oscillations and Phase portraits vary with different Re and I^*

Table 4.5: C2 measured average horizontal velocities(Vx), vertical velocities (Vy), and angular velocities (pitch) in-air drop.

	Drop Angle (Deg)	Vx(mm/s)	Vz(mm/s)	Pitch(rad/s)	I^*	Re
C2	0	100.18	-1707.03	3.4	17.20	2845
	5	59.88	-1757.43	0.51	17.20	2929
	10	88.71	-1650.08	2.59	17.20	2750
	15	46.81	-1142.38	1.02	17.20	1904
	20	116.95	-1710.45	4.24	17.20	2851
	25	24.17	-523.64	0.78	17.20	873
	30	13.99	-206.77	0.66	17.20	345
	40	25.20	-339.69	1.19	17.20	566
	45	113.78	-1682.15	6.33	17.20	2804

Table 4.6: D1 measured average horizontal velocities (Vx), vertical velocities (Vy), and angular velocities (pitch) in-air drop.

	Drop Angle (Deg)	Vx(mm/s)	Vz(mm/s)	Pitch(rad/s)	I^*	Re
D1	0	111.51	-1700.32	1.57	3.86	12370
	5	112.07	-1707.02	1.40	3.86	12419
	10	162.12	-1682.43	2.37	3.86	12240
	15	222.79	-1661.68	2.93	3.86	12089
	30	241.05	-1880.75	2.85	3.86	13686
	35	314.58	-1960.72	4.07	3.86	14264

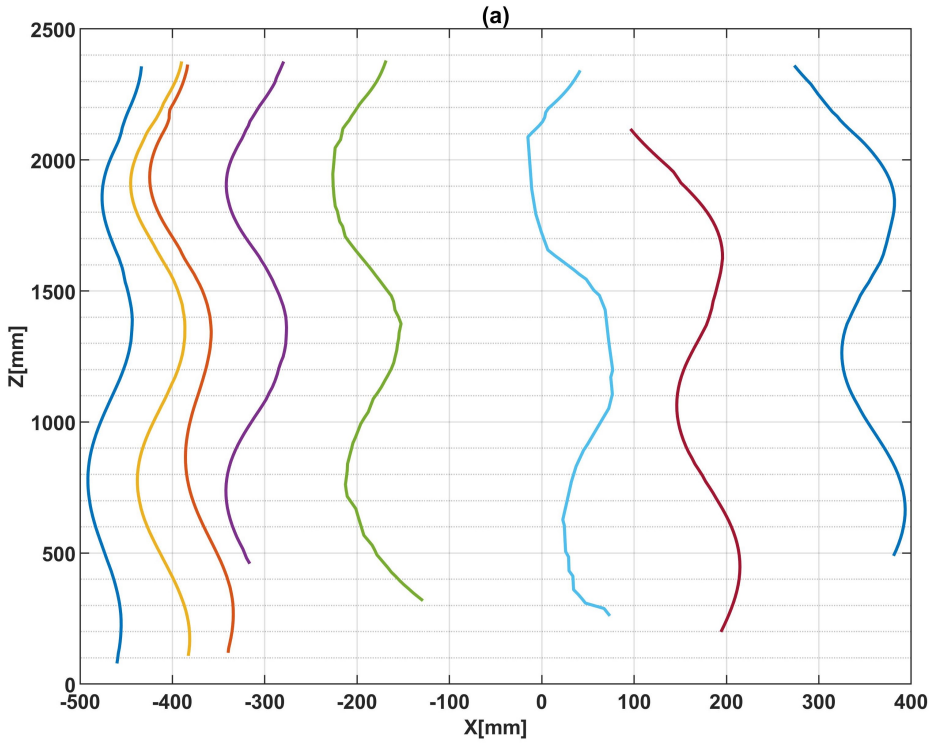

((a))

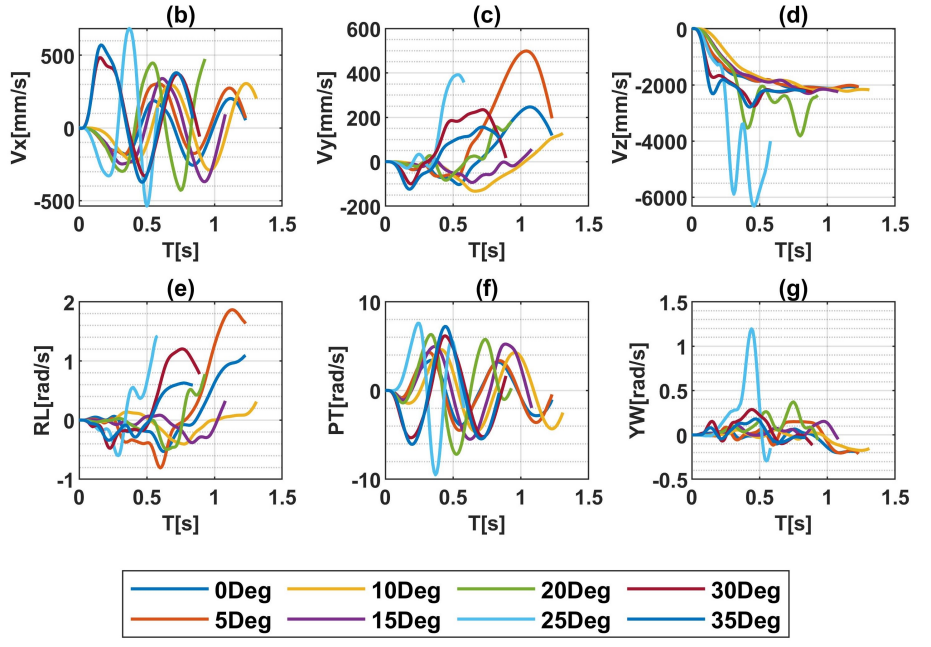

((b))

Figure 4.13: D3 different measured plate trajectories:(a), time histories of translational velocities:(b,c,d), rotational velocities:(e,f,g) of in-air zigzag plate at angles of 0^0 to 30^0 with different interval of 5^0 and showing how oscillations vary with different drop angle.

The body horizontal and vertical velocities at different initial angles of release show the velocity in the horizontal direction oscillates at more than three times the frequency of the vertical velocity, and the oscillation amplitude is smaller in the yaw angle of rotation. However, the motion exhibits periodic pitching and translational oscillations. Furthermore, an increase in I^* results in greater rotational oscillation, and above $7.75\ rad^s$ rotational velocity, the plate topples and exhibits a tumbling behavior. The duration of tumbling and fluttering is considered longer for heavy plates, as also reported by Lau et al. (2018).

Table 4.7: D3 measured average horizontal velocities(Vx), vertical velocities (Vy), and angular velocities (pitch) in-air drop.

	Drop Angle (Deg)	Vx(mm/s)	Vz(mm/s)	Pitch(rad/s)	I^*	Re
D3	0	140.26	-1693.19	1.75	3.74	12699
	5	140.10	-1657.97	2.02	3.74	12435
	10	172.76	-1682.13	2.52	3.74	12616
	15	239.63	-1709.00	3.36	3.74	12818
	20	305.98	-1697.28	4.12	3.74	12730
	30	214.37	-1787.81	3.10	3.74	13409

Table 4.8: D5 measured average horizontal velocities(Vx), vertical velocities (Vy), and angular velocities (pitch) in-air drop.

	Drop Angle (Deg)	Vx(mm/s)	Vz(mm/s)	Pitch(rad/s)	I^*	Re
D5	0	114.16	-1730.73	1.68	6.25	12980
	5	130.14	-1686.96	1.91	6.25	12652
	10	194.80	-1513.22	2.68	6.25	11349
	15	236.27	-1652.24	3.40	6.25	12392
	25	137.67	-1773.49	1.28	6.25	13301
	30	180.79	-1910.81	1.89	6.25	14331

Table 4.9: D4 measured average horizontal velocities(Vx), vertical velocities (Vy), and angular velocities (pitch) in-air drop.

	Drop Angle (Deg)	Vx(mm/s)	Vz(mm/s)	Pitch(rad/s)	I^*	Re
D4	0	91.59	-1761.02	1.54	6.56	12577
	5	141.90	-1717.47	2.00	6.56	12266
	10	137.27	-1595.49	2.13	6.56	11394
	15	226.90	-1693.14	3.53	6.56	12092
	30	230.88	-2006.70	3.12	6.56	14331

In the general falling problem of a *2D* flat plate (Andersen et al. (2005a); Lau et al. (2018)), cylinder (Chrust et al. (2010); Chrust (2012); Chrust et al. (2013)) or 3D disc (Zhong and Lee (2012); Auguste et al. (2013); Esteban et al. (2020)), flow instability is connected to Re and I^*. Similarly, early investigation on heavy plates leads to the findings of bistability, where stable falling and tumbling are both possible due to the initial angle of release (Lau et al. (2018)). An extendend Re and I^* phase diagram corresponding to different falling plates shown in Figure 4.15, the phase diagram represents different experimental results of steady falling, fluttering, tumbling, chaotic, helix, and spiral motions from different literature on light plates (a) and extension on the current heavy plate results showing a periodic zigzag regime (b).

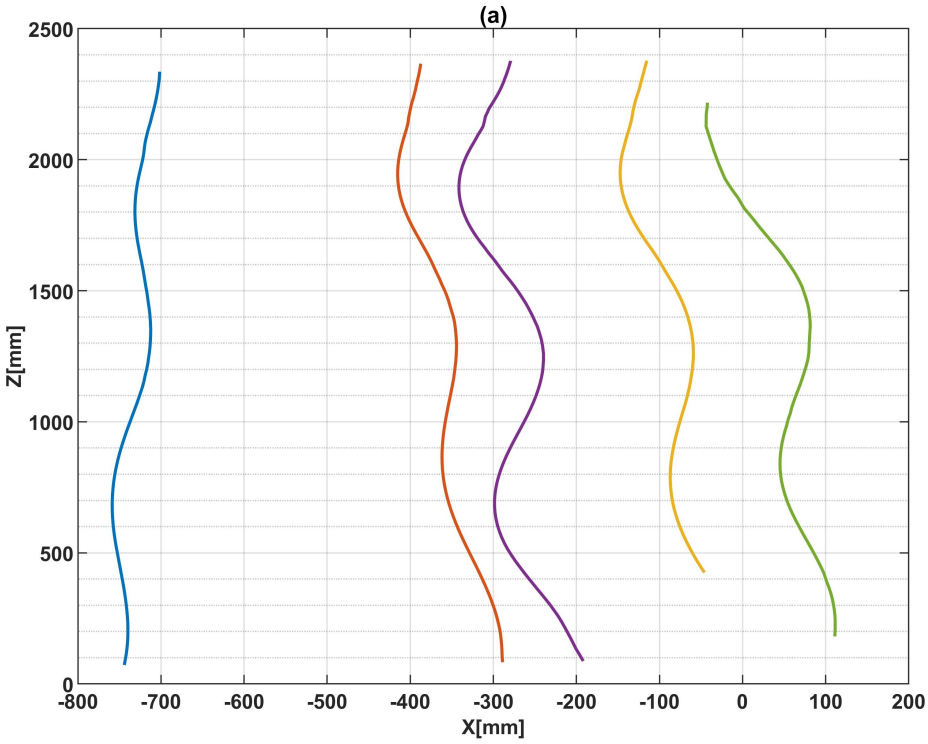

((a))

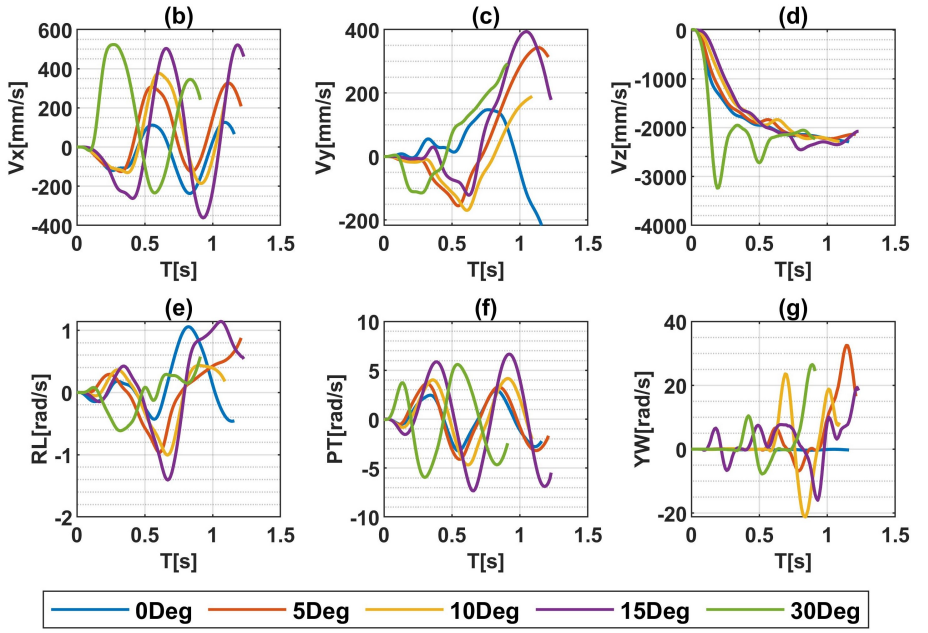

((b))

Figure 4.14: D4 different measured plate trajectories:(a), time histories of translational velocities:(b,c,d), rotational velocities:(e,f,g) of in-air zigzag plate at angles of 0^0 to 30^0 with different interval of 5^0 and showing how oscillations vary with different drop angle.

Furthermore, in the present findings both vertical, horizontal and rotation velocities are stochastic and they do not depend on the initial release angle. Similarly bistability depends on the initial angle of released from zigzag to tumbling motion, where trajectories on fluttering and tumbling are independent of initial angle of release as reported by (Andersen et al. (2005a); Wu and Lin (2015); Zorzi et al. (2015)) for thin rectangular plate but Lau et al. (2018) reported a changes with heavy plate from stable to tumbling depending on the initial angle of released.

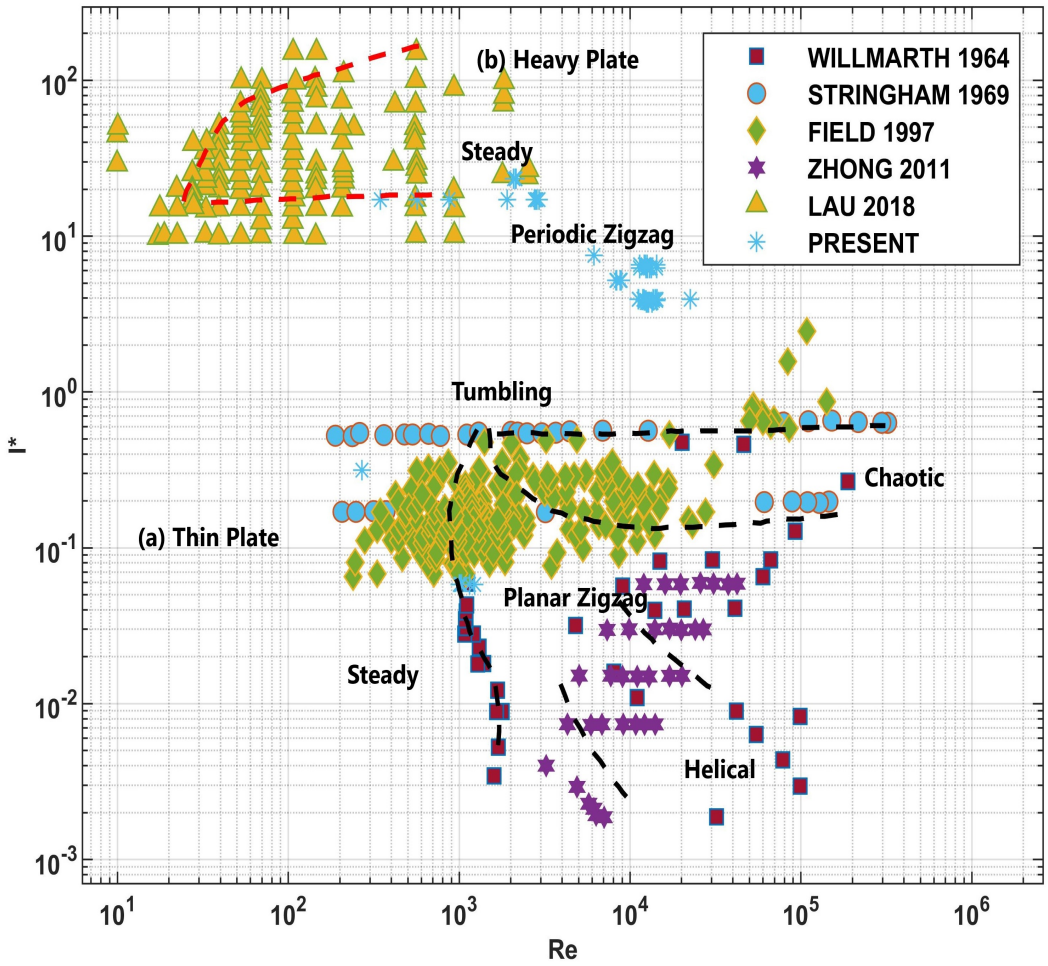

Figure 4.15: Phase diagram showing current and previous results of Re & I^* (b) regime map of light plate $I^* < 1$ and (a) heavy plate with $I^* > 1$ results are plotted together with current and previous reference results.

The phase portrait shown in Figure 4.15 looks similar to the stable vertical falling trajectory results of Lau et al. (2018) with small oscillation of Vx and $OmegaPT$. However, the results shown in Figure 4.13 and Figure 4.14 show nearly twice the results presented by Lau et al. (2018) with a high oscillation angle. As Re increases, because of the lower viscous effect, the frequency and pattern of oscillation become much more zigzag. Thus, as the motion cycles around the stationary point, at *(0,0)* in Figure 4.11(b) and Figure 4.12(b), the gravitational force restores the rectilinear paths, which look similar to what was reported by Lau et al. (2018). In comparison to the present results, the stable trajectories reported by Lau et al. (2018) produce relatively low lift with insignificant flight characteristics. Therefore, the current research concludes the wobbling motions as zigzag since the lift is higher as compared to the results of Lau et al. (2018).

Table 4.10: Summary of non-dimensional parameters from previous literature and present investigations.

Reference	I^*	Re	β^*
Dupleich (1949)	0.6 - 26	600 - 35000	0.8 - 6
Andersen et al. (2005a)	0.16 - 0.48	700 - 1800	15 - 30
Hirata et al. (2009)	3 - 150	1800 - 6400	2 - 20
Wang et al. (2013)	9.2 - 12.3	4500 - 6400	2 - 10
Lau et al. (2018)	0.10 - 20	80 - 12000	10 - 110
Present	0.058 - 23.33	270 - 22000	5 - 39

Table 4.10 provides a summary of non-dimensional parameters from previous literature and current research. The experimental results lie within the findings of Lau et al. (2018) as shown from Table 4.1 to Table 4.9. Lau et al. (2018) reported that when I^* increases with respect to the horizontal axis, the vertical velocity increases while horizontal and rotational velocities decrease, which is also similar to Dupleich (1949) and Wang et al. (2013) findings. However, in the present findings both vertical, horizontal, and rotational velocities are stochastic and are not dependent on the initial angle of release. Similarly, bistability is shown to depend on the

initial angle of release from zigzag to tumbling motion, whereas the trajectories of fluttering and tumbling are independent of the initial angle of release, as reported by Andersen et al. (2005a); Wu and Lin (2015); Zorzi et al. (2015) for light plates.

In addition Lau et al. (2018) reported that beyond the upper boundary (red dot), plates will never tumble at any release angle, and below the lower boundary (red dot), a plate will develop into tumbling and will not fall steadily. In the present research, as shown in Figure 4.15, some plates fall in zigzag motion without tumbling in the lower boundaries of the phase diagram.

Finally, Lau et al. (2018) shows the relationship between I^*, Re and θ^0 to determine the bistability and the critical angle that will set plates from stable falling to tumbling, and shows a steeper initial angle of 58^0, 75^0, and 51^0 is required for heavy plates to change it's trajectory from stable falling to tumbling, in the current study a critical initial angle of 20^0, 30^0, 35^0 and 45^0 as shown in Table 4.1 to Table 4.8 is required to make the plate to tumble.

Chapter 5

NUMERICAL MODELLING OF FALLING PLATE PROBLEM

This chapter presents preliminary studies carried out with the aim of developing and validating the numerical results with existing experimental and numerical results from Andersen et al. (2005a) and Jin and Xu (2008). The numerical setup presented in chapter 3 methodology is used for the model setup to determine the trajectories, translational and rotational velocities. A mesh and time independence analysis is carried out to show the sensitivity of a freely falling plate with measurement of uncertainty to estimate the solution error due to temporal discretization. Finally, this research extends this work to include the numerical investigation of a freely falling plate with an initial speed by using the validated results to investigate the falling trajectories, velocities, and forces.

5.1 Background

The accuracy of the numerical *CFD* method is of great interest in the academic community for several reasons. However, one issue that remains challenging is that of grid generation, on which the solution of the governing partial differential equations is to be obtained. To capture the physics of free falling plates numerically, the computational mesh must be refined. Although grid sensitivity studies are frequently analysed in academia but the outcomes are not always understood by researchers,

in industrial applications, on the other hand, a single mesh analysis is considered due to the perception that error estimation is difficult and time-consuming (Terziev et al. (2020)). Uncertainties in the physical properties appear to have lower relevance compared to the uncertainties in the turbulence modes used to estimate the Reynolds stresses (Fokken et al. (2019)).

Computational models play an ever-growing role in predicting the behaviour of real-world systems or physical phenomena (Groen et al. (2021)). In addition, scientific computing is based on a mathematical model in the form of coupled systems of nonlinear partial differential equations systems (Roy and Oberkampf (2011)). However, computational models have undergone an extraordinary increase in sophistication over the years, but often the models are simple representations of the real world and can behave differently for some reason. Another source of discrepancy between experimental and numerical data can exist due to assumptions and simplifications made in the numerical simulation to reduce the computational cost, but sometimes make them less accurate. Unfortunately, most numerical simulations of physical systems are rife with sources of uncertainty such as geometric, initial/boundary conditions, structural, and parametric. The main difference between an experimental and a numerical simulation is that numerical simulations are considered deterministic, while experiments are inherently affected by uncertainty (Salvadori (2019)).

In recent years, the estimation of *CFD* errors and uncertainties has reached a certain level of maturity. However, the decision to use *CFD* must be firmly based on a realistic expectation of its performance, cost, and effort required (Martín (1999)), note that using *CFD* does not necessarily ensure accurate results (Baker et al. (1997)) despite this, the use of numerical simulation is gaining more acceptance in the research and engineering community due to its growing accuracy and accessibility. Verification in *CFD* is needed to demonstrate that relevant physics of the problem are being properly addressed, while validation is needed to demonstrate successful model problems for which either experimental data or reliable semi-empirical

correlations are available (Chen and Srebric (2002)). Schwer (2009) provided a flow chart of verification and validation activities and outcomes, as shown in Figure 5.1 .

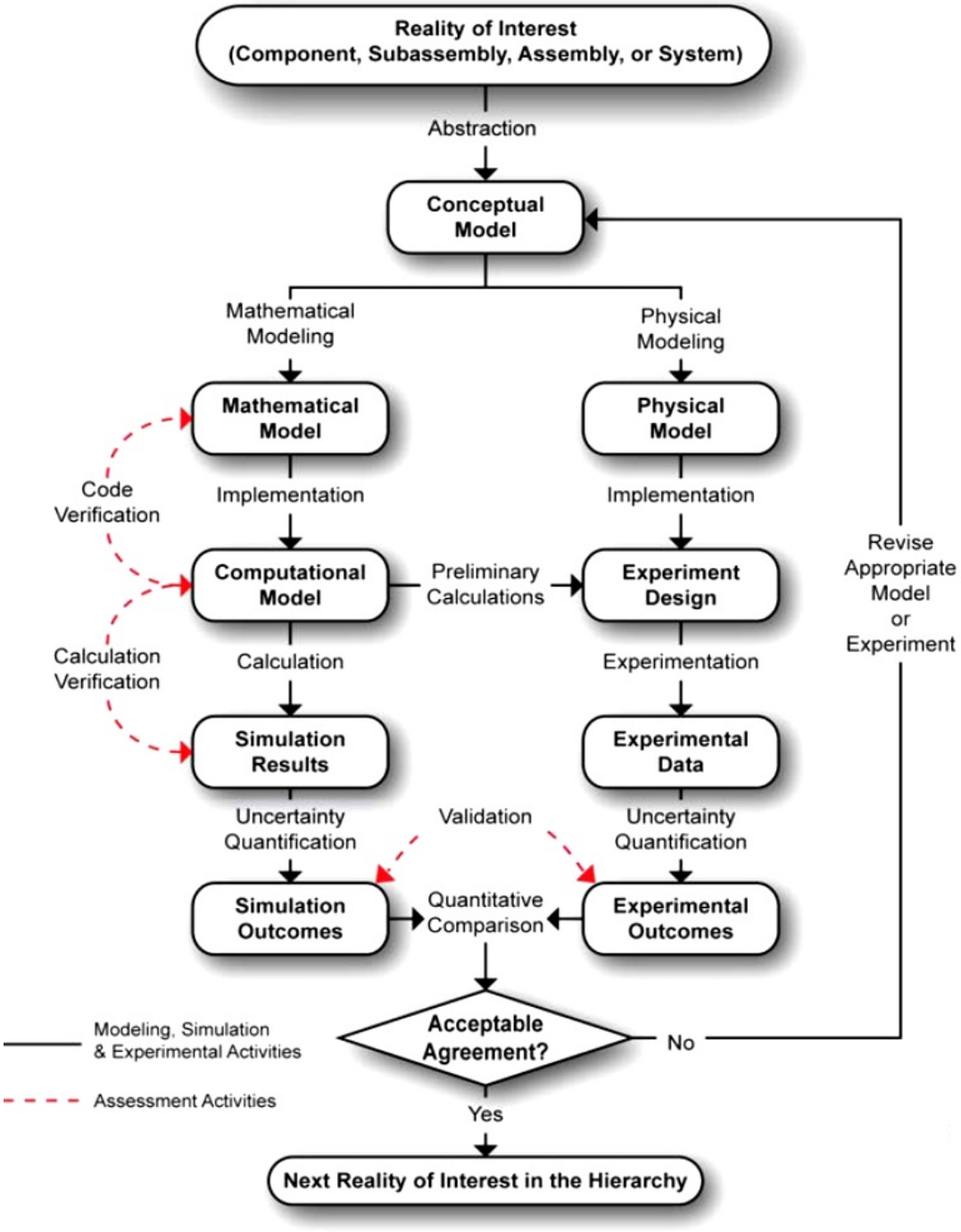

Figure 5.1: Verification and validation activities and outcomes. Guide figure)

When compared to analytical methods, computational methods have greater capability of addressing significant complex physical phenomena, and many processes

of immense practical importance such as the turbulent motion of a fluid cannot be described analytically (Terziev et al. (2020)). On the other hand, due to the equivalence between the continuum form of the governing partial differential equations and their discrete approximation in *CFD* simulation, errors and uncertainty can be classified into five categories.

1. Physical approximation errors are those due to uncertainty in the formulation of the model and deliberate simplifications of the model, which can be as a result of difference between the exact solution of the equation describing the fluid flow by satisfying the conservative laws and the actual flow. These errors deal with continuum model only, often modeling is required for turbulence quantities, transition, and boundary conditions. However, for a laminar flow the Navier Stokes equations are sufficiently accurate but to account for cases where turbulence modelling is important, additional models are required (Terziev et al. (2020)). Even when a physical process is known to a higher level of accuracy, a simplified model may be used within *CFD* code for convenience.

2. Iterative convergence error exists because of the iterative methods used in *CFD* simulations which have a stopping point eventually, that arises as a result of the nonlinearity of the governing equations.

3. Errors in Computer Programming: Programming errors are "bugs" and mistakes that occur during the programming or writing of code. They are the programmers' responsibility. These types of errors are discovered by performing verification studies on subprograms and the entire code, reviewing the lines of code, and performing validation studies on the code. Before releasing the code, the programming errors should be fixed.

4. Usage errors occur when the code is applied in an inefficient or incorrect manner. Usage errors can manifest as modelling and discretization errors. The user configures the models, grid, algorithm, and inputs used in a simulation, which determines the simulation's accuracy. There may be obvious errors,

such as attempting to compute a known turbulent flow using an inviscid flow assumption. A converged solution may be obtained; however, the simulation's conclusions may be incorrect. Errors may not be as obvious, such as incorrect selection of turbulence model parameters for separated flows with shocks. The number of options available in a *CFD* code increases the possibility of usage errors. The accumulation of experience and proper training reduces usage errors. In order to speed up the simulation at the expense of accuracy, the user may intentionally introduce modelling and discretization errors. This may be appropriate in the conceptual stage of a design study where more general information with less accuracy is required. Even in the later stages, there may be insufficient computational resources to simulate at the appropriate grid density. The level of accuracy associated with the results must be understood. Through proper training and analysis, usage errors should be manageable. In addition to the *CFD* code, usage errors can occur in the CAD, grid generation, and post-processing software.

5. Grid convergence study is effective way to determine amount of discretization error in a *CFD* solution. Discretization errors occur when governing flow equations are represented as algebraic expressions in a discrete domain of space. Grid or mesh is a discrete spatial domain; the time step demonstrates the temporal discreteness. As the number of grid points increases and the size of the grid spacing tends to zero, a consistent numerical method will approach the continuum representation of the equations and have zero discretizibility error. The level of discretization error is determined by the flow features as resolved by the grid. Errors may arise as a result of the grid's representation of discontinuities (shocks, slip surfaces, interfaces, etc.). Interpolation errors occur at zonal interfaces where one zone's solution is approximated on the boundary of another zone. The difference between the partial differential equation (PDE) and the finite equation is the truncation error.

The numerical validation used in this research is based on Richardson extrapola-

tion by expressing the error as an expanded power series with integer powers of grid spacing (Δx) or time step (Δt) as a finite sum, assuming the solutions lie within asymptotic range, it is admissible to take only the first term into account, leading to the so-called grid triplet study (Terziev et al. (2019)).

Four types of conditions that govern whether a numerical solution is convergent or divergent as both grids spacing, or time step are refined can be summarized as:

1. Monotonic convergence: $0<R<1$
2. Oscillatory convergence: $R<0;\ |R|>1$
3. Monotonic divergence: $R>1$
4. Oscillatory divergence: $R<0;\ |R|>1$

However, for conditions 3 and 4, neither error nor uncertainty can be estimated. Where R is the convergence ratio.the value of R can be defined as:

$$R_{\mathrm{k}} = \frac{\varepsilon_{21}}{\varepsilon_{32}} \tag{5.1}$$

Where ε_{21} is the difference between medium (f_2) and fine (f_1) solutions, and ε_{32} is the difference between the coarse (f_3) and medium (f_2) mesh solutions. The solutions of (f_1),(f_2) and (f_2) are obtained by systematically coarsening the mesh or time parameter with a refinement ratio of $r = \sqrt{2}$, recommended by Procedures (2008), while the validation is carried out against the experiment results and error is calculated using:

$$E = (EFD - CFD)/(EFD \times 100) \tag{5.2}$$

5.2 Determination of Local Error and Uncertainty

After describing the error and uncertainty estimation methods above, the local error and uncertainty is estimated using Terziev et al. (2019) by defining Richardson and oscillatory nodes as:

- Richardson nodes: (f_3 - f_2) × (f_2 - f_1) > 0
- Oscillatory nodes: (f_3 - f_2) × (f_2 - f_1) > 0

Also both convergence nodes and divergent nodes are computed. Terziev et al. (2019) use the local accuracy order to produce a global average. However, Phillips and Roy (2017) also provided a similar framework and modified first, as shown Equation (3.49). Absolute value of the numerator quotient is taken. The accuracy ranking at each location is not directly used. Phillips and Roy (2017) and Terziev et al. (2019) both defined the global deviation from formal accuracy *(p_f = 2)* in Equation (3.50), which can be interpreted as the mean local deviation of the observed and theoretical accuracy orders. To avoid skewing the average, the maximum deviation is restricted to *4p_f*, Phillips and Roy (2017) and Terziev et al. (2019) both considered p_f multiplicative factors of *2, 4, 6,* and *8* when deriving p, but the choice was unimportant. To avoid zero values, the observed order of accuracy is limited to *95%* of p_f, after calculating p, one can calculate the global distance from Equation (3.51) and estimate the uncertainty as:

$$Uncertainty = FS(p^*)\left|\frac{f_2 - f_1}{r^{p*} - 1}\right| \tag{5.3}$$

5.3 Reference Model of Tumbling Plate

This PhD research's numerical simulation considers an experimental model of a tumbling rigid plate developed by Andersen et al. (2005a) and Jin and Xu (2008). For the case of a freely-falling tumbling plate, the plate thickness is taken to be h = *8.1 × 10^{-4}m* , with the plate width-to-thickness ratio of $\beta = L/h$ =*1/8*. The density of the plate ρ_s = *2700 kgm^{-3}* and the density for the fluid ρ_f = *1000 kgm^{-3}*, the fluid viscosity is *v=0.00089 m^2 s^{-1}*. The centre of gravity of the plate is located at *(x_0,y_0) = (0,0)* with an initial release angle of *45^0* & *0^0* with respect to the horizontal axis with initial speed. A rectangular tumbling plate with a dimensionless moment of inertia I^* = 0.29 and *Re = 837* was used.

5.4 Initial Speed Effects of Freely Tumbling Plate

Numerically, the dynamics of the falling plate with an initial velocity were investigated, keeping the plate release angle at 0^0. Since there is no experimental data to validate the results, verification of the results is carried out using Richardson extrapolation. A number of research studies were conducted to determine the trajectory of projectile motion because moving projectiles through the air with an arbitrary initial velocity and slope has been a matter of debate over the past two decades. In addition to the study of projectile motion, the aerodynamics of windborne debris flight are also being studied.

However, experimental and numerical studies on the motions of freely falling plates in a viscous fluid with an initial speed have not been studied in detail. Lau et al. (2018) studied freely falling heavy plates and showed that the initial angle of release can influence the motion from steady falling to tumbling, while Andersen et al. (2005a) numerically studied free-falling thin rectangular plates and investigated the effect of initial conditions, showing changes in absolute velocities and trajectories. While Esteban et al. (2020) investigated experimentally discs falling in turbulence, the discs showed an increase in the mean descent velocity with new trajectories not discovered in previous studies. In this research, we investigated numerically the $2D$ freely falling motion of a rectangular plate with an initial velocity in the range I^* and Re of tumbling as shown in Table 5.5.

5.5 Mesh and Time Independence Analysis

The presence of complex flow regimes during the motion of a freely falling plate and the errors generated from the computational techniques make the numerical modelling of falling plates a challenging task. To achieve a desired level of accuracy during numerical simulation, mesh and time-step independence analyses need to be carried out. However, the computational power and numerical accuracy of the solution play a very important role in deciding the selection of a computational model,

including a suitable turbulence model. In addition, since a mesh-independent solution is entirely dependent on the type of mesh created to capture the fluid flow, therefore, mesh-independent solutions are produced by eliminating the effects of several factors, such as rounding, iterative, and discretization errors. Refining the mesh is considered as a remedy for reducing errors by many researchers (Almohammadi et al. (2013)). Once a solution is both mesh and time-independent, then it can be compared with available experimental data. In this research, both mesh and time independence analysis were carried out to investigate the sensitivity of the unsteady motion of a freely falling plate for different cell counts and time. The computational method that is widely used for solving the unsteady Reynolds average Navier-Stokes equations in computational fluid dynamics is the finite volume method, and the method has proven its superiority in many applications provided that the mesh independence solution is achieved (Almohammadi et al. (2013)). Rana et al. (2020) studied the effect of mesh and time resolution on the trajectory of fluttering and tumbling plates. It was confirmed that time resolution is strongly sensitive to the unsteady dynamic while the mesh is weakly dependent on perious literature.

The step towards achieving a mesh and time-independent solution is to first obtain a mesh convergence solution with an iterative convergence solution. The former can be obtained by monitoring the plots of the trajectories and the velocities as shown in Figure 5.2 to Figure 5.7. While the latter is obtained by the set tolerance in the residuals as shown in Figure 5.8 to Figure 5.11. However, the mesh converged solution and the iterative converged solutions are performed using the same mesh, and when the solutions do not change as the mesh is refined, then the mesh independent solution is considered to be achieved. The same applies to time-independent.

5.6 Results and Discussions

In this section, the obtained results are presented and compared against experiment and numerical measurements of previous literature. The uncertainty of numerical

measurement is presented to show the accuracy and efficiency of the numerical method used for both mesh and time studies, and finally initial velocity case of tumbling plate with initial speed presented. The discussions of the findings are also presented.

5.7 Comparison Between Experiment and Numerical Simulations

The first step taken in this chapter is to present the mesh and time studies results and compare the results with measured experimental and numerical results from previous literature, error is determined using Equation (5.2) which is used in validating the results. In order to determine the discretization errors, numerical simulations using overset grids have been performed with different grid sizes, refined systematically by increasing the number of cells as shown in Table 3.4 and also time step in Table 3.5. However, in unsteady simulation deciding on an adequate choice of time-step is of critical important, since if the time step is large the numerical simulation becomes unstable or gives an unrealistic results in the case of freely falling plates, in addition, numerical noise may manifest as seen in numerical simulation of Jin and Xu (2008) if time-step is not selected correctly. The numerical result is compared with quasi-two-dimensional experiment and numerical study of rectangular falling plate Andersen et al. (2005a), Jin and Xu (2008), Kolomenskiy and Schneider (2010) and Wu and Lin (2015).

5.7.1 Mesh Convergence Study

Figure 5.2 to Figure 5.7 shows the result of the trajectory, horizontal velocity, vertical velocity, angular velocity and phase plot performed with different grid seizes, one can see from these results that mesh used is sufficient to obtained grid independent studies with good convergence since the results of fine mesh with cells number *82052* did not change with coarse mesh with cells number *32272* as shown. Furthermore,

the results shows that fine mesh with *82052* cells is grid independent, since the results obtained with an extra-fine mesh with cells number *147896* did not change with mesh expansion.

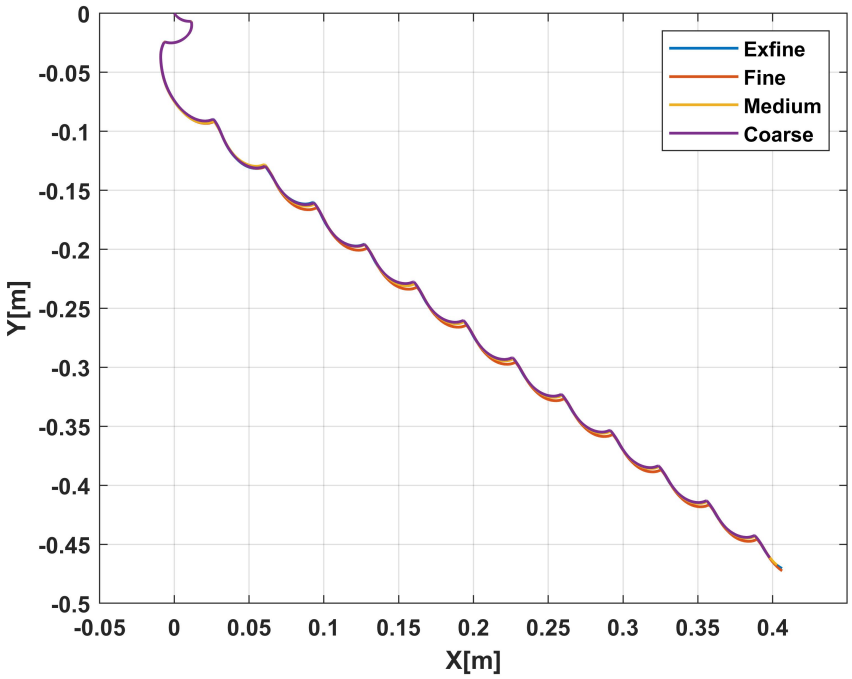

Figure 5.2: CFD mesh study simulation at 45^0 drop showing trajectories of tumbling plate at $\beta = 1/8$

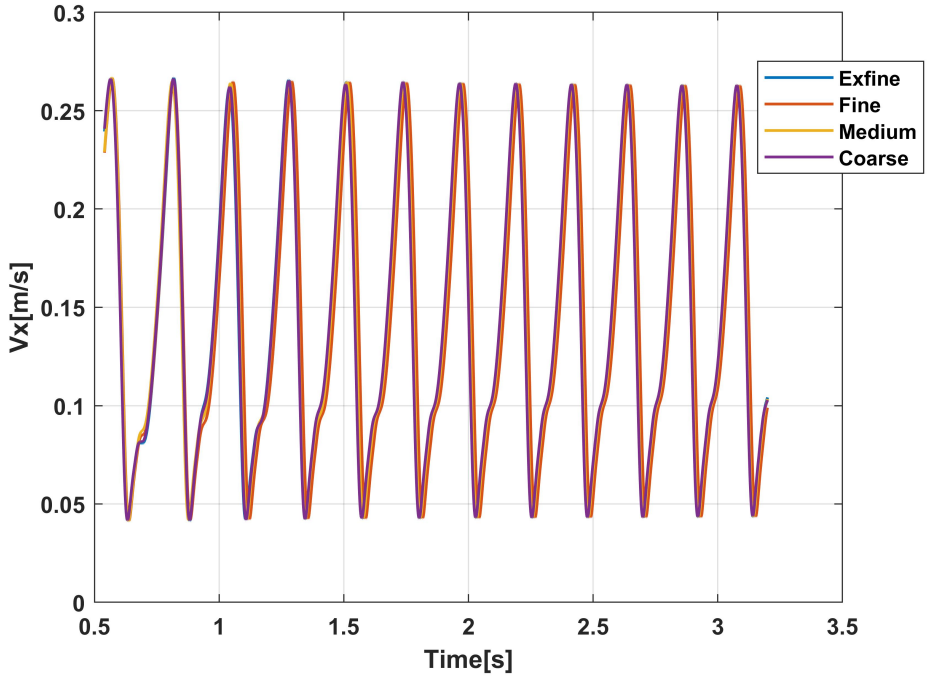

Figure 5.3: CFD mesh study simulation at 45^0 drop showing horizontal velocities (Vx) of tumbling plate at $\beta = 1/8$

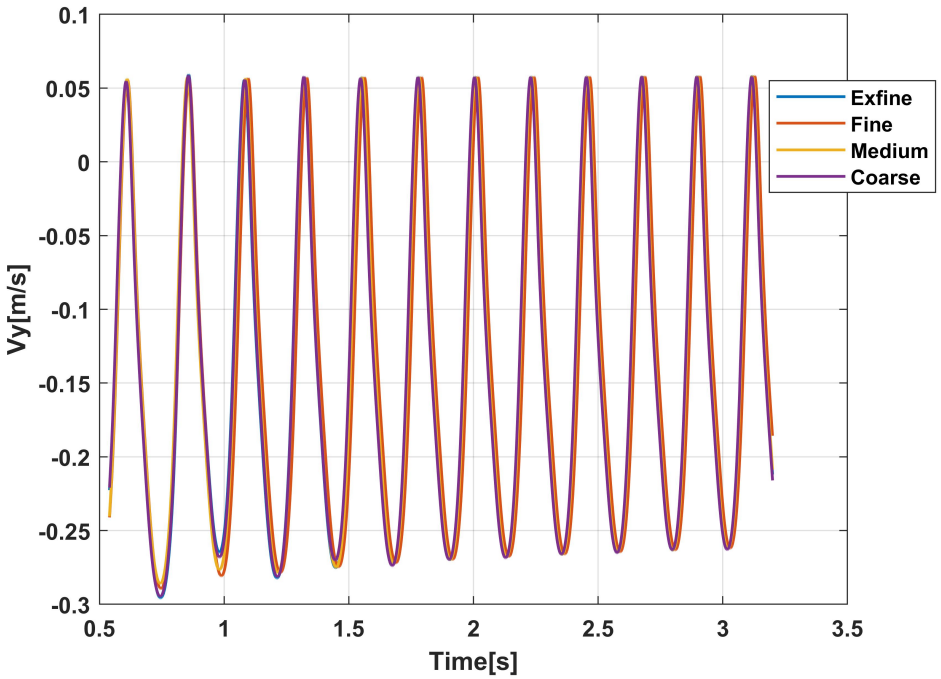

Figure 5.4: CFD mesh study simulation at 45^0 drop showing vertical velocities (Vy) of tumbling plate at $\beta = 1/8$

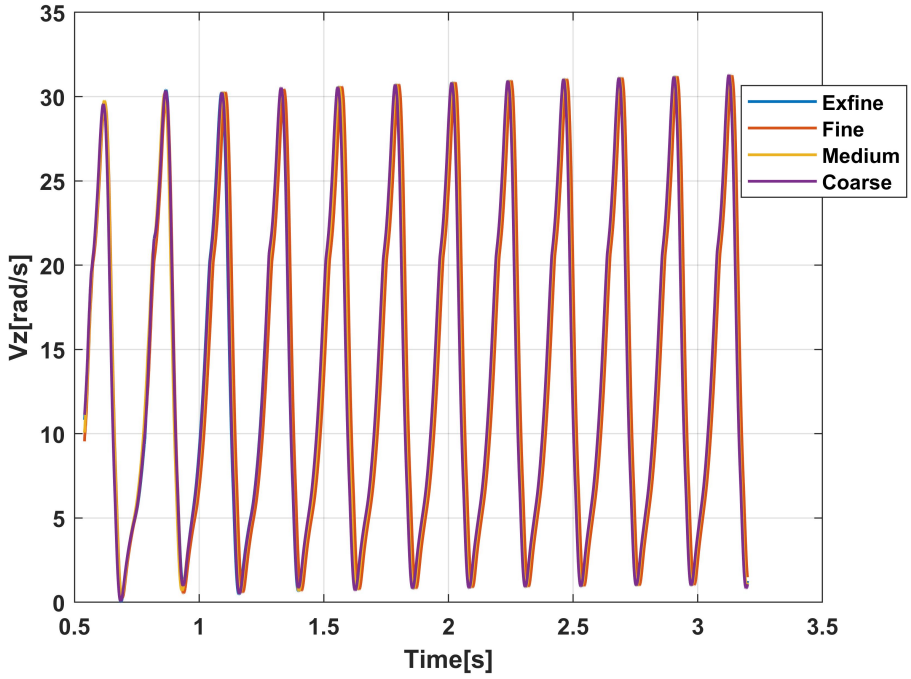

Figure 5.5: CFD mesh study simulation at 45^0 drop showing rotational velocities (Vz) of tumbling plate at $\beta = 1/8$

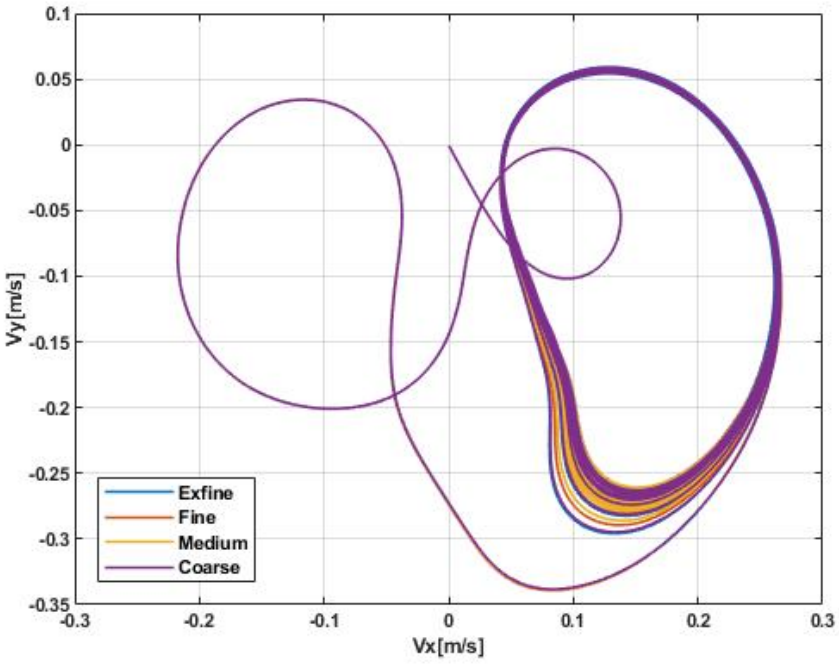

Figure 5.6: CFD mesh study simulation at 45^0 drop showing Vx versus Vy of tumbling plate at $\beta = 1/8$

5.7.2 Time Convergence Study

The accuracy of time-step was assessed using the fine mesh Figure 5.7 to Figure 5.11 shows the results of trajectories, horizontal velocities, vertical velocities and rotational velocities of the plate freely falling, using different time-step a good convergence is achieved with a time-step of $7.5E^{-4}s$. Even though an analysis with a smaller time-step could reveal slightly different results as shown Figure 5.7 to Figure 5.11.

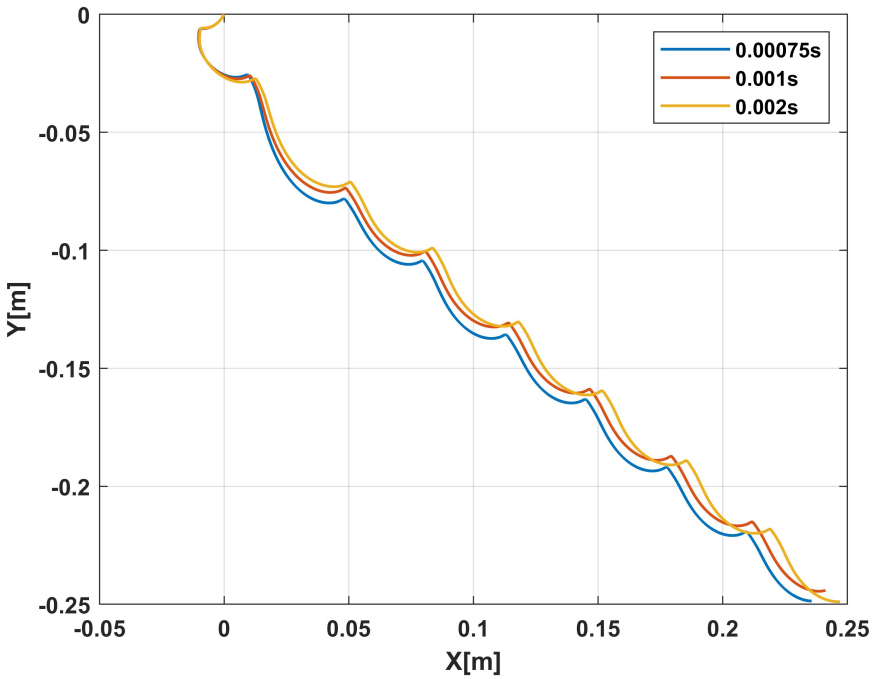

Figure 5.7: CFD time study simulation at 45^0 drop showing trajectories of tumbling plate at $\beta = 1/8$

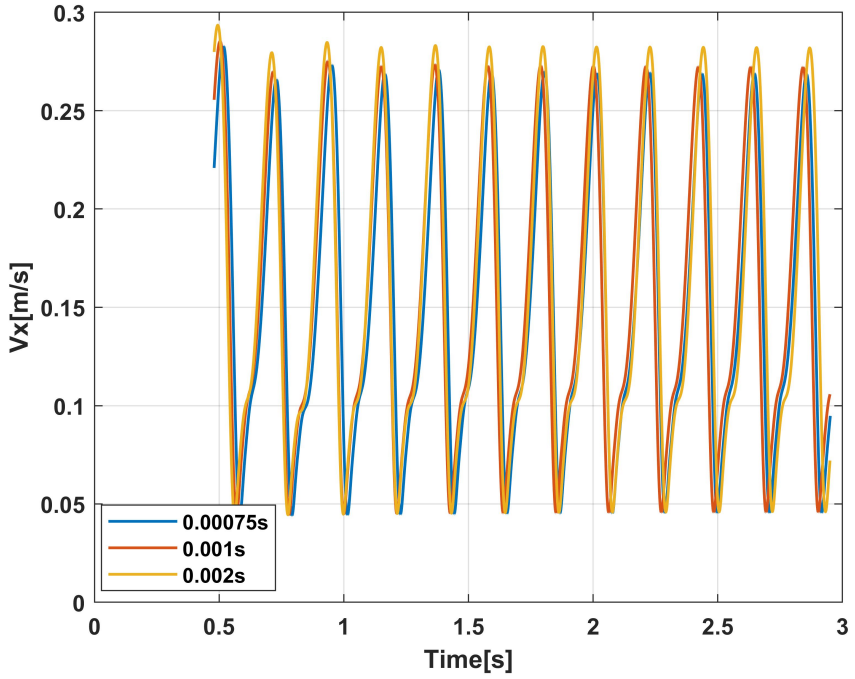

Figure 5.8: CFD time study simulation at 45^0 drop showing horizontal velocities (Vx) of tumbling plate at $\beta = 1/8$

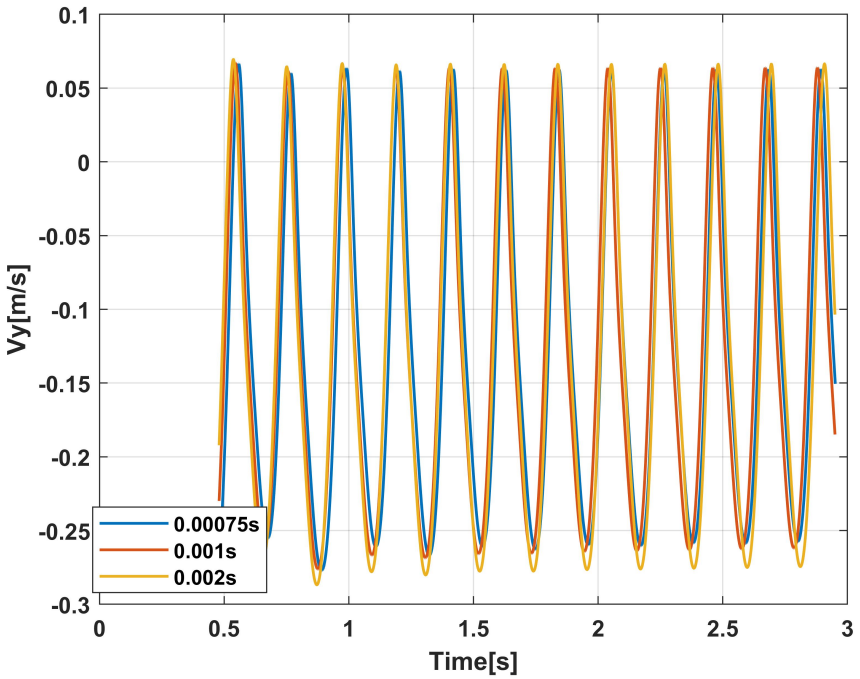

Figure 5.9: CFD time study simulation at 45^0 drop showing vertical velocities (Vy) of tumbling plate at $\beta = 1/8$

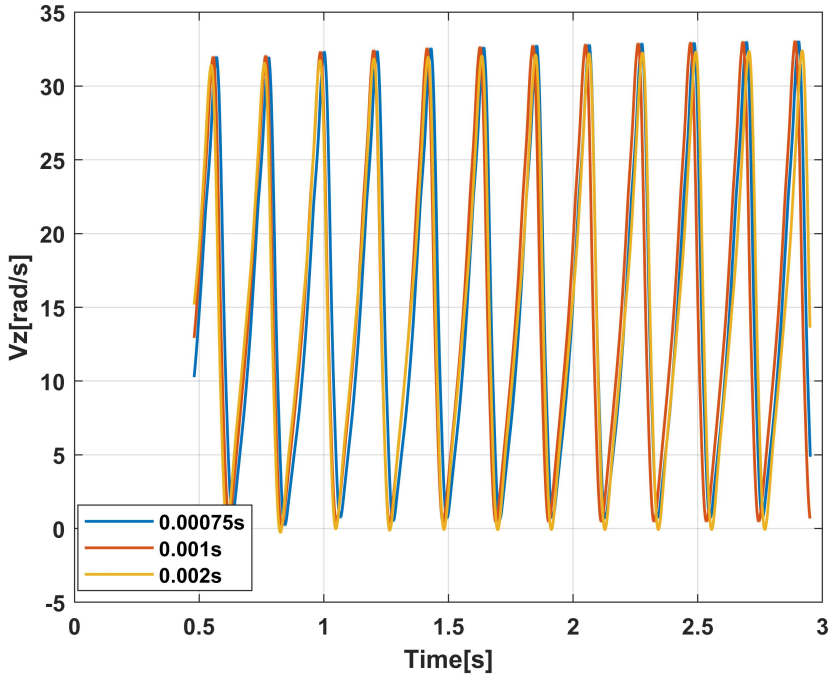

Figure 5.10: CFD time study simulation at 45^0 drop showing rotational velocities (Vz) of tumbling plate at $\beta = 1/8$

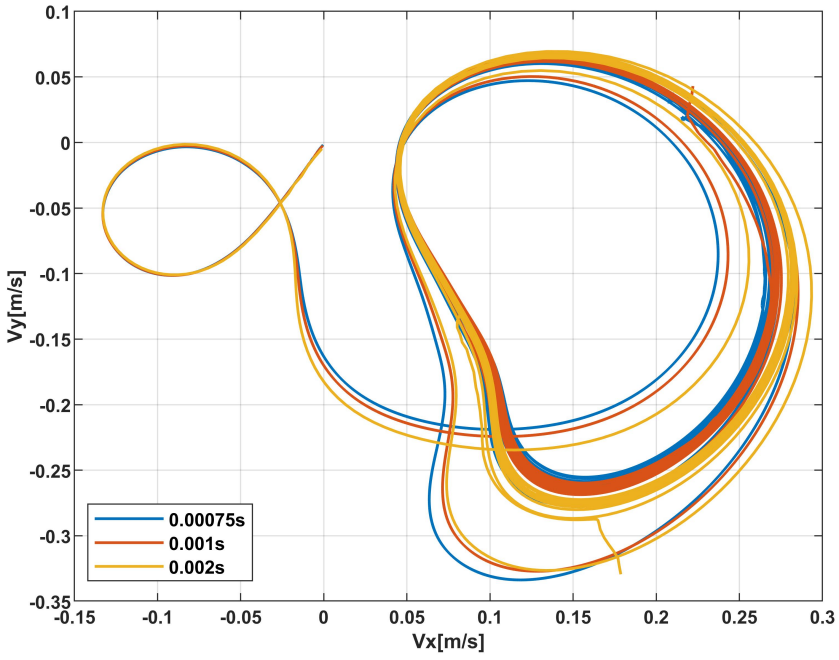

Figure 5.11: CFD time study simulation at 45^0 drop showing Vx versus Vy of tumbling plate at $\beta = 1/8$

5.7.3 Experimental and Numerical Results

Figure 5.12 to Figure 5.15 compared the present *CFD* simulation results with Jin and Xu (2008), the trajectory shows same pattern but with a phase shift compared to numerical results, the discrepancy may be expected due to Jin and Xu (2008) simulation result with initial fluttering behaviour and only the tumbling part was presented and compared with the experimental results.

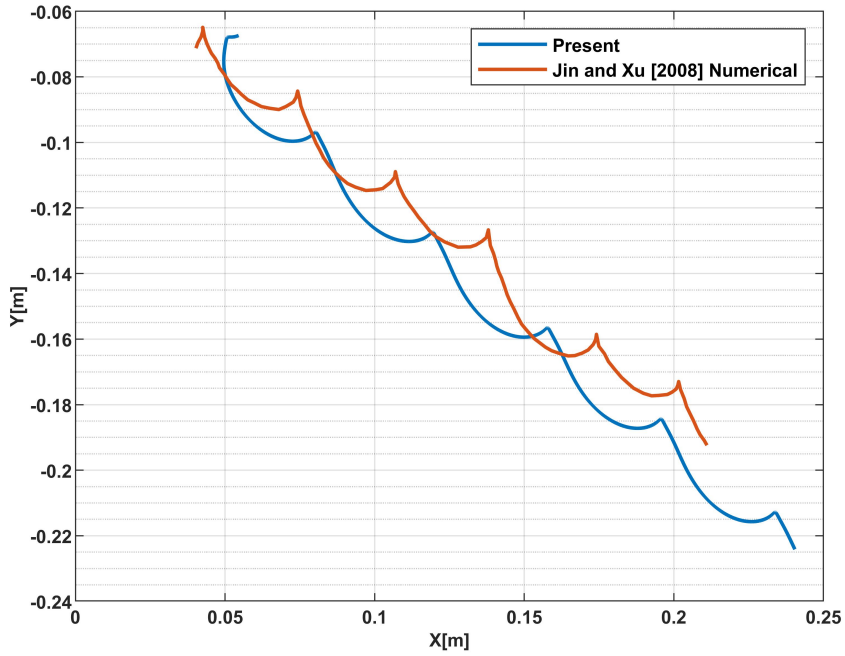

Figure 5.12: Trajectories of tumbling plate at $\beta = 1/8$ validation against previous literature

Figure 5.12 compared the present *CFD* simulation results with Jin and Xu (2008) numerical results, the trajectory shows same pattern but with a phase shift compared to numerical results, the discrepancy may be expected due to Jin and Xu (2008) simulation result with initial fluttering behaviour and only the tumbling part was presented and compared with the experimental results.

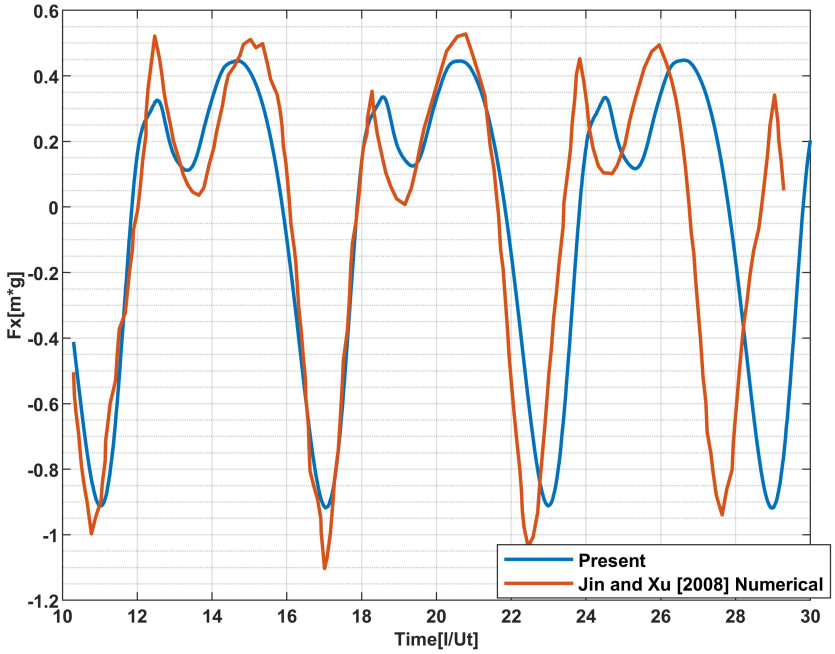

Figure 5.13: Horizontal force of tumbling plate at $\beta = 1/8$ validation against previous literature

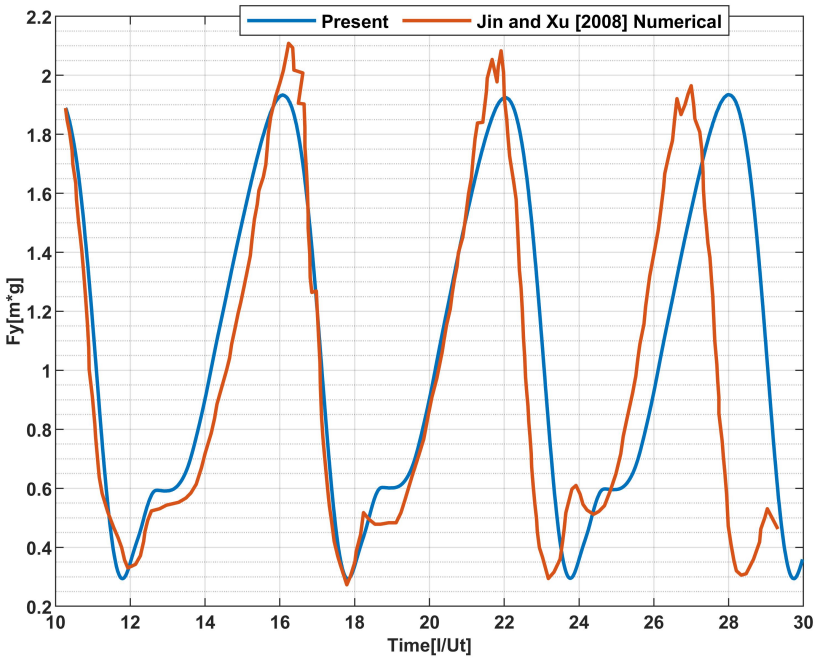

Figure 5.14: Vertical force of tumbling plate at $\beta = 1/8$ validation against previous literature

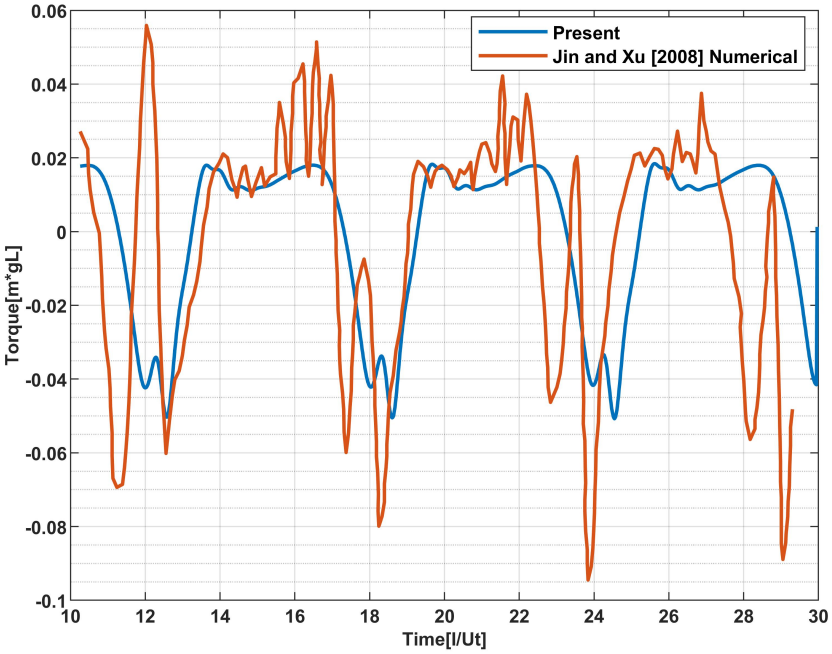

Figure 5.15: Torques of tumbling plate at $\beta = 1/8$ validation against previous literature

Table 5.1: Comparison of experimental and numerical tumbling plate average translational and angular velocities

Investigations	Vx(m/s)	Vy(m/s)	Vz(rad/s)
Andersen et al. (2005a). Experimental	0.159	-0.115	14.5
Jin and Xu (2008) Numerical	0.151	-0.118	15.0
Present numerical simulations	0.160	-0.110	14.0

Table 5.2: The error between experimental and numerical data is presented in the table

Investigations	Vx(m/s)	Vy(m/s)	Vz(rad/s)
Andersen et al. (2005a). Experimental	0.159	-0.115	14.5
Present numerical simulation	0.160	-0.110	14.0
Error	3.82%	4.44%	3.51%

Figure 5.12, Figure 5.13 and Figure 5.15 show the dimensionless fluid forces, torque and moment and compared with Jin and Xu (2008) numerical results, the

curve trend of Fx, Fy and torque with dimensionless time T^* results fit well with the previous literature, but noise was observed in the numerical results of Jin and Xu (2008) the author did not give any explanation on why the noise was observed, however, the measured Fx and Fy shows the curve trend of both top and bottom amplitude of the dynamic oscillations as a function of dimensionless time T^* the forces Fx & Fy minimum and maximum values of oscillations corresponding to validated results with the peaks showing some difference. In addition, a phase shift was observed in Figure 5.12, Figure 5.13 and Figure 5.15. Jin and Xu (2008) attributed the small phase error between experimental and numerical results due to smaller angular velocities difference between the present model and numerical model.

The error estimation against experimental results of Andersen et al. (2005a) is presented in Table 5.2 and shows that the method can predict the translational and angular velocities of the tumbling plate considering the percentage error of *3.51%* to *4.44%* which is between the acceptable margins of *5%-10%*.

5.8 Uncertainty Study of Mesh and Time Convergency

The numerical uncertainties are measured via the grid convergence index (GCI) method, since is one of the standard ways of reporting numerical uncertainties. Three grid sizes are used in determining the uncertainty of GCI method which requires systematically reducing the mesh and time-step size with a refinement ratio of $\sqrt{2}$ as recommended by Procedures (2008). The GCI method assumes that all the three solutions are close to asymptotic range, the proximity to the asymptotic range is typically determined by the convergence ratio shown in Equation (3.49).

5.8.1 Mesh Uncertainty Study

The measured numerical solution for the Mesh study local uncertainty and extrapolation of the free-falling plate trajectories and velocities are discussed with the factor of safety and the order of convergence. To obtain the uncertainty convergence of the mesh, results are summarized in Table 5.3. To obtain the solutions of the grid convergence study the smallest time step of 7.5E-4s is used while coarsening the grid with $\sqrt{2}$ as shown in Table 3.4 . The results in Figure 5.17 and Figure 5.18 shows that fine, medium and coarse mesh having oscillatory and monotonically converged nodes with negligible divergent. However, Table 5.4 shows the measured percentage convergent nodes of *90% - 99%* X and Y position with *98%* translational and rotational velocity convergence.

The factor of safety in Figure 5.19 shows the convergence study of mesh, as part of procedure for the *GCI* requirement to show whether the suggested *FS* of *1.25* agrees with Phillips and Roy (2012, 2017), none of the nodes is asymptotic base on the criteria of Equation (3.52) therefore refinement for mesh study is not required.

Table 5.3: 45^0 drop mesh study computed uncertainty of X&Y position with horizontal, vertical and rotational velocities

	X position	Y position	Vx velocity	Vy velocity	Vz velocity
Number of monotonically convergent nodes	674	3980	3487	3480	3677
Monotonically convergent nodes percentage of total	16.17%	95.49%	83.66%	83.49%	88.22%
Number of oscillatory convergent node	3114	163	616	614	440
Oscillatory convergent nodes percent of total	74.71%	3.91%	14.78%	17.73%	10.56%
Total number of convergent nodes	3788	4143	4103	4094	4117
Percentage convergent nodes	90.88%	99.40%	98.44%	98.22%	98.78%

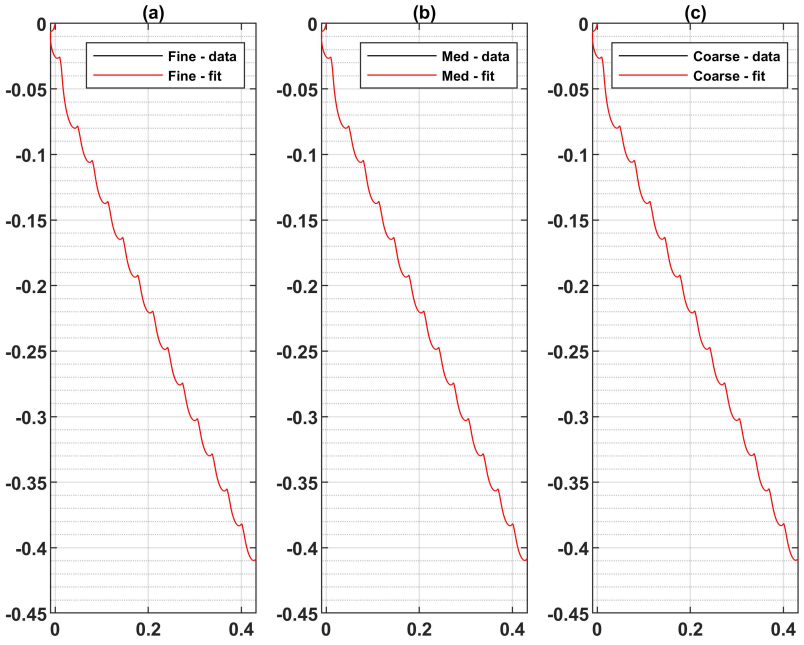

Figure 5.16: Mesh study of 45^0 drop computed uncertainty of (a) fine, (b) medium and (c) coarse mesh trajectory

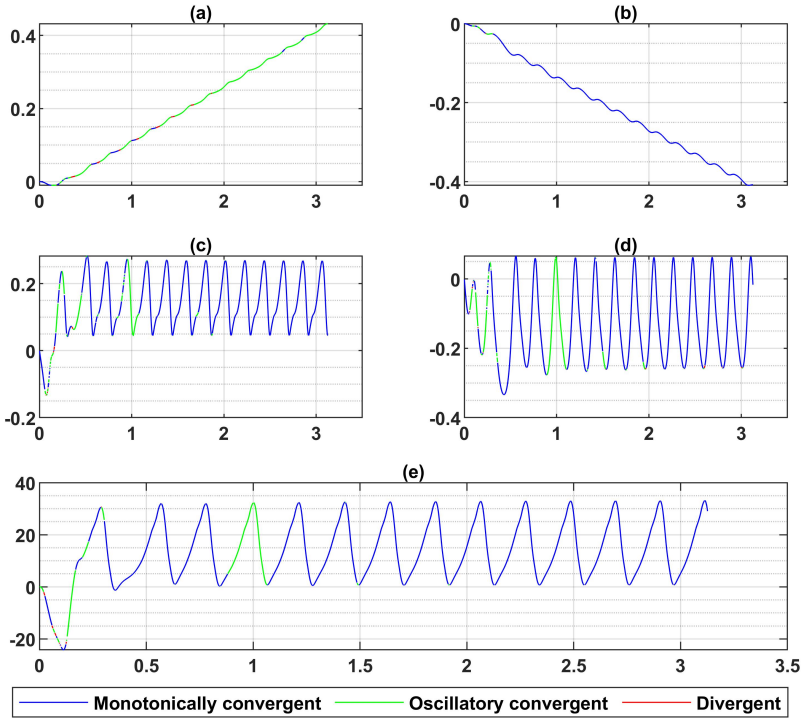

Figure 5.17: Mesh study of 45^0 drop numerical convergence computed uncertainty of (a) X position state of each node, (b) Y position state of each node, (c) Vx position state of each node, (d) Vy position state of each node, (e) Vz position state of each node

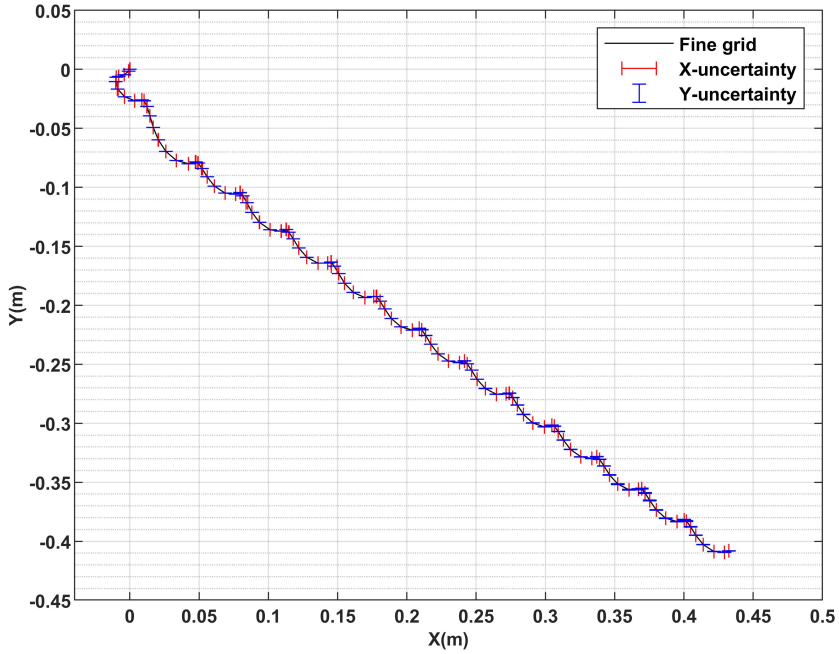

Figure 5.18: 45^0 drop computed error of trajectory of tumbling plate mesh study

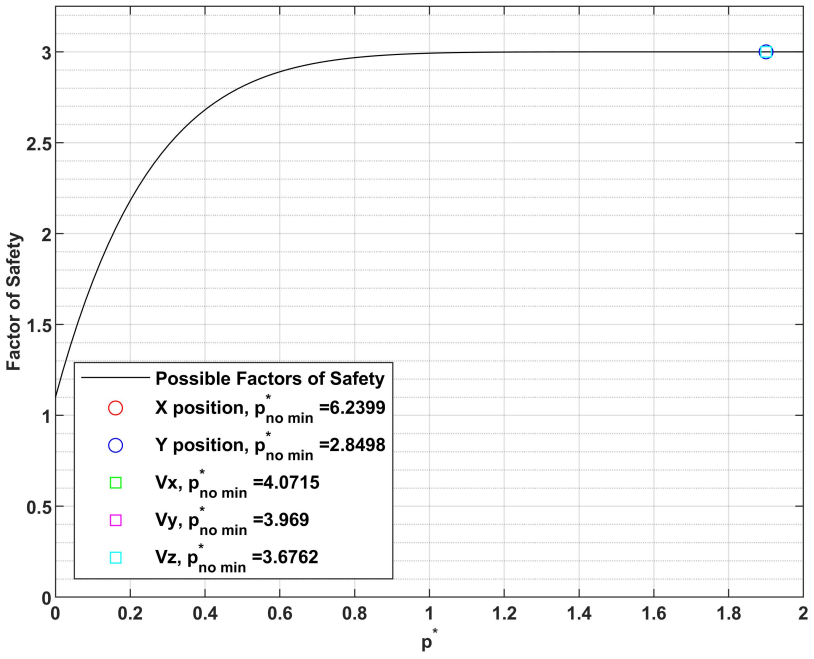

Figure 5.19: 45^0 drop mesh study computed factor of safety

5.8.2 Time Uncertainty Study

To obtain the local uncertainty and extrapolation convergence of time studies of the measured trajectories and velocities are discussed with the factor of safety and the order of convergence. To obtain the uncertainty of time the results are summarized in Table 3.5 with different time steps, the fine mesh in Table 3.4 i used to determine the time convergence. The results in Table 5.4 shows that unsteady simulation of falling plate numerically is subject to greater uncertainty with time rather than mesh study, divergent nodes from *0s - 1.2s* as shown in Figure 5.21 was observed. However, Table 5.4 shows the measured percentage convergent nodes of *75% - 84%* *X & Y* position, *73%* to *75%* translational and rotational velocity.

The factor of safety in Figure 5.23 showing less than what was recommended by Phillips and Roy (2012, 2017), therefore a smaller time step is required to achieved convergences for the trajectories *(*X & Y). in addition, due to divergent nodes in the time study high error is seen in the trajectory measurement of Figure 5.22. However, convergent is archived for horizontal, vertical and rotational velocity with *GCI* requirement showing values above *1.25* as recommended by Phillips and Roy (2012, 2017) shown in Figure 5.23.

Table 5.4: 45^0 drop time study computed uncertainty of X&Y position with horizontal, vertical and rotational velocities

	X position	Y position	Vx velocity	Vy velocity	Vz velocity
Number of monotonically convergent nodes	2313	694	348	448	349
Monotonically convergent nodes percentage of total	74.00%	22.20%	11.13%	14.33%	11.16%
Number of oscillatory convergent node	41	1947	2004	1835	2036
Oscillatory convergent nodes percent of total	1.31%	62.28%	64.10%	58.70%	65.13%
Total number of convergent nodes	2354	2641	2352	2283	2385
Percentage convergent nodes	75.30%	84.49%	75.24%	73.03%	76.30%

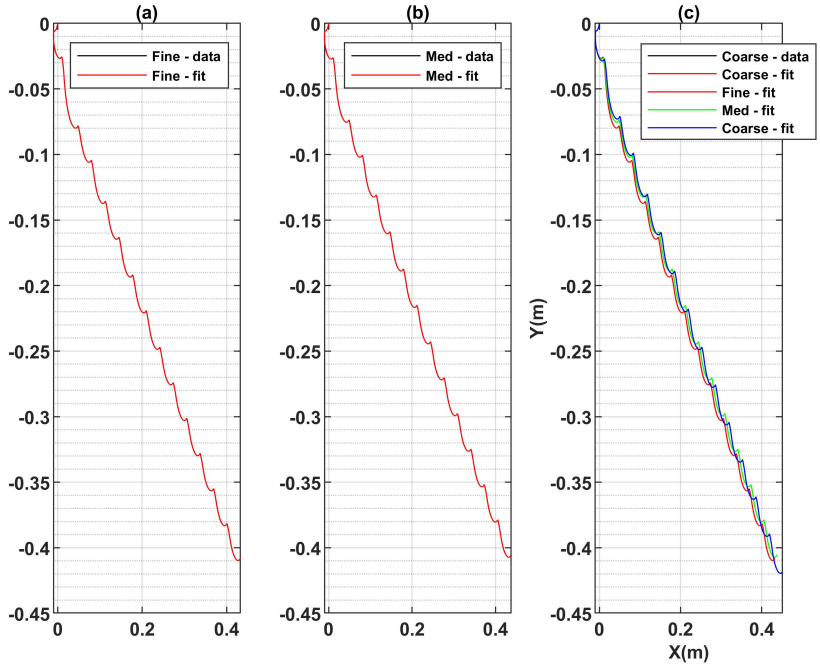

Figure 5.20: Time study of 45^0 drop computed uncertainty of (a) fine, (b) medium and (c) coarse trajectories

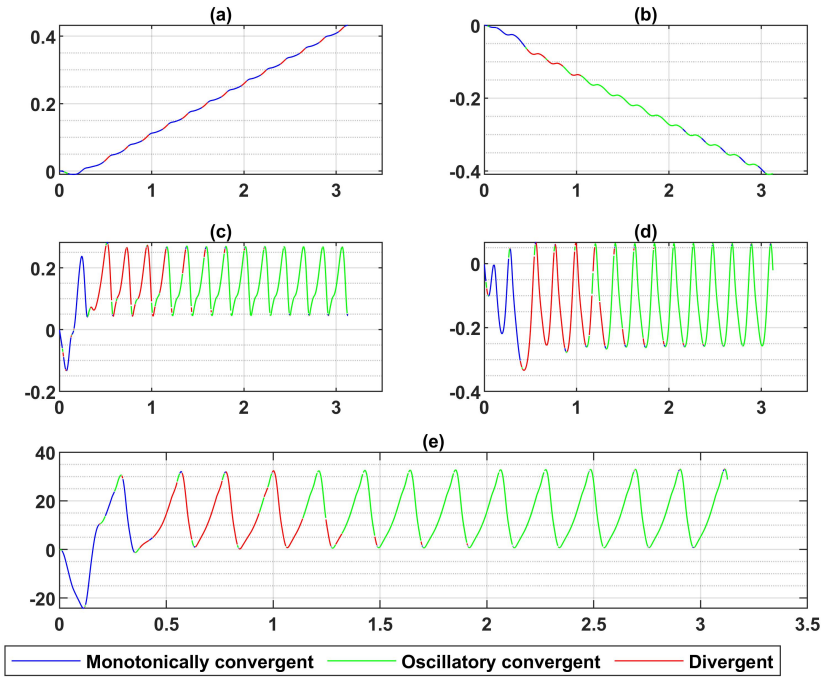

Figure 5.21: Time study of 45^0 drop numerical convergence computed uncertainty of (a) X position state of each node, (b) Y position state of each node, (c) Vx position state of each node, (d) Vy position state of each node, (e) Vz position state of each node

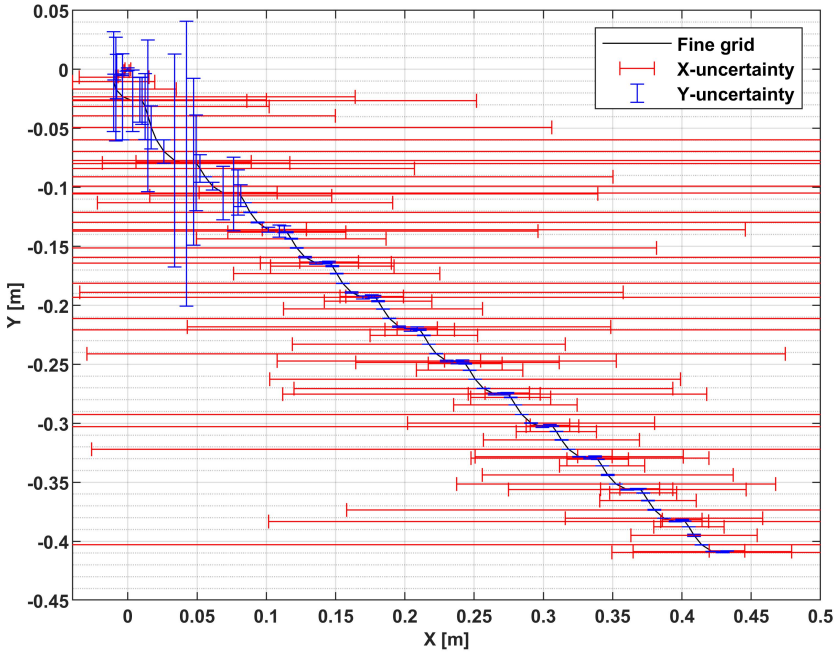

Figure 5.22: 45^0 drop computed error of trajectory of tumbling plate time study

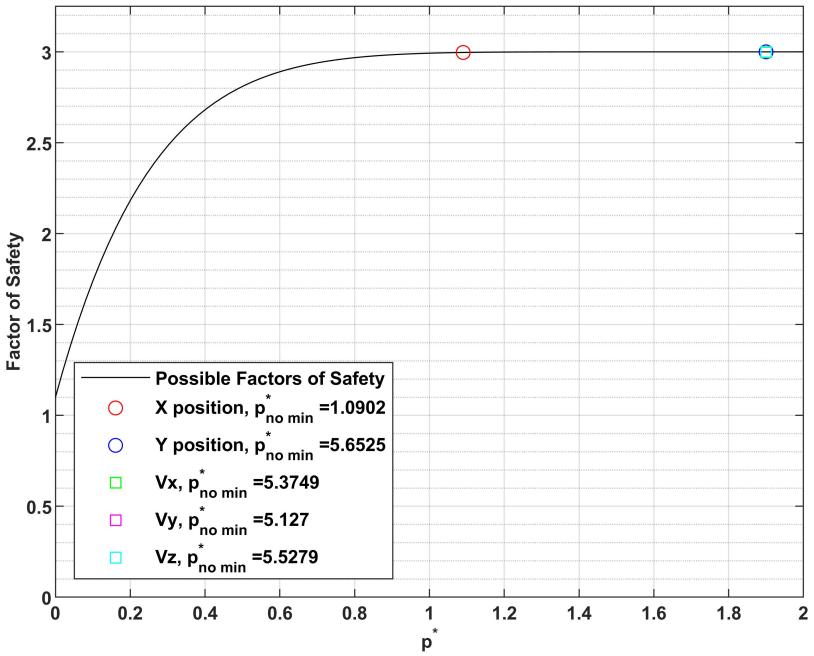

Figure 5.23: 45^0 drop time study computed factor of safety

5.9 Initial Velocity Case

5.9.1 Mesh Study 0^0 drop freely falling with No speed

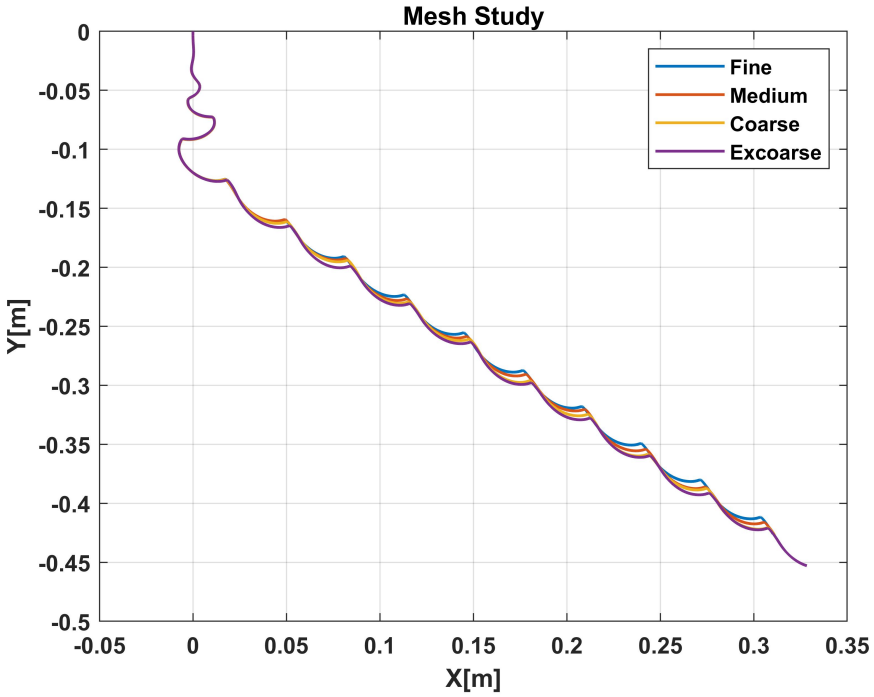

Figure 5.24: CFD mesh study simulation at 0^0 drop showing trajectories of tumbling plate at $\beta = 1/8$

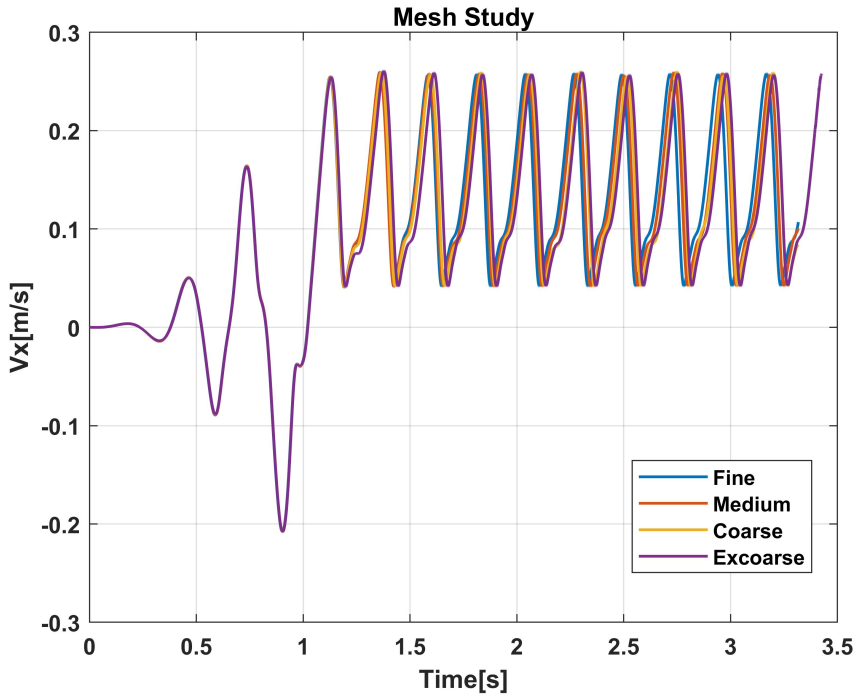

Figure 5.25: CFD mesh study simulation at 0^0 drop showing horizontal velocities (Vx) of tumbling plate at $\beta = 1/8$

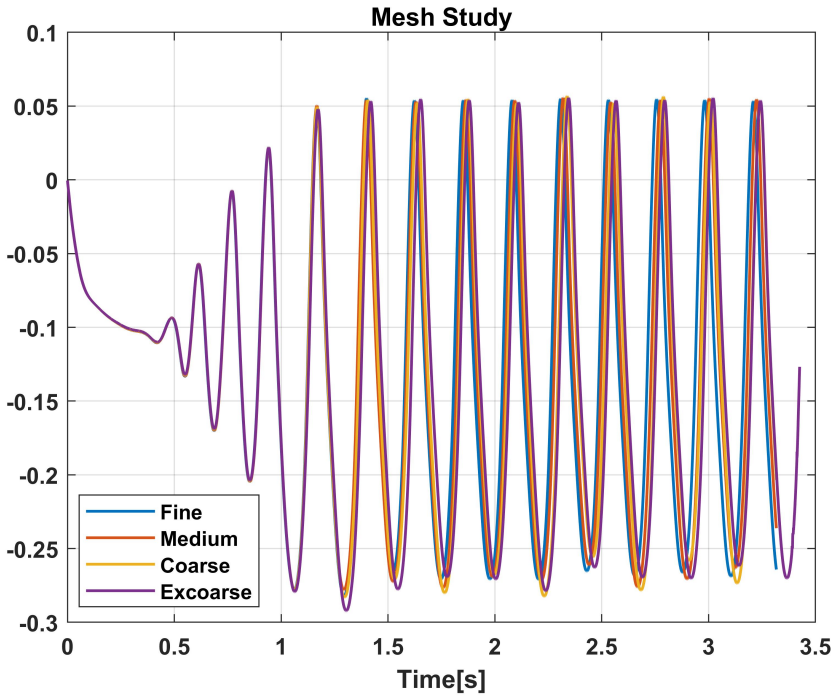

Figure 5.26: CFD mesh study simulation at 0^0 drop showing vertical velocities (Vy) of tumbling plate at $\beta = 1/8$

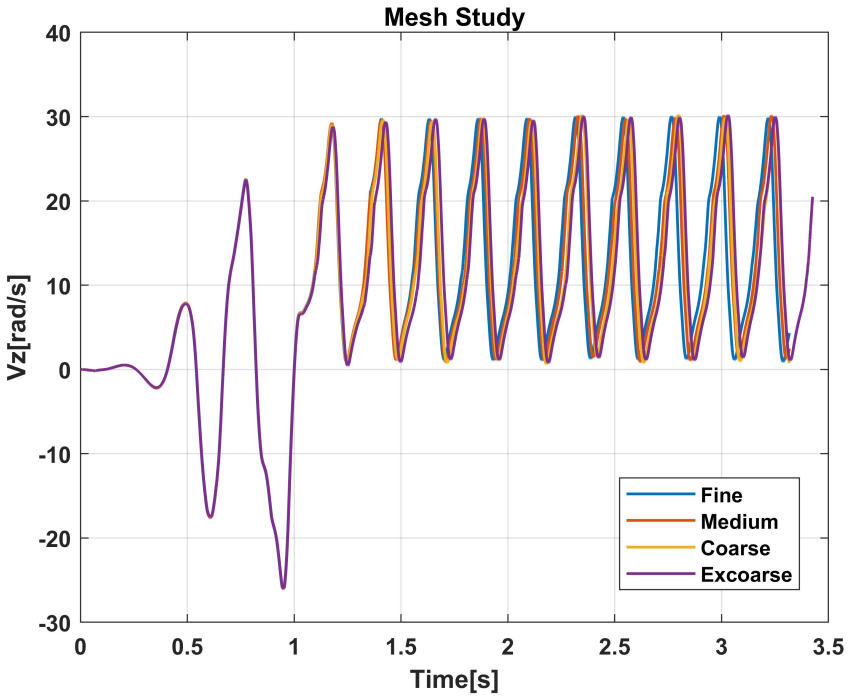

Figure 5.27: CFD mesh study simulation at 0^0 drop showing rotational velocities (Vz) of tumbling plate at $\beta = 1/8$

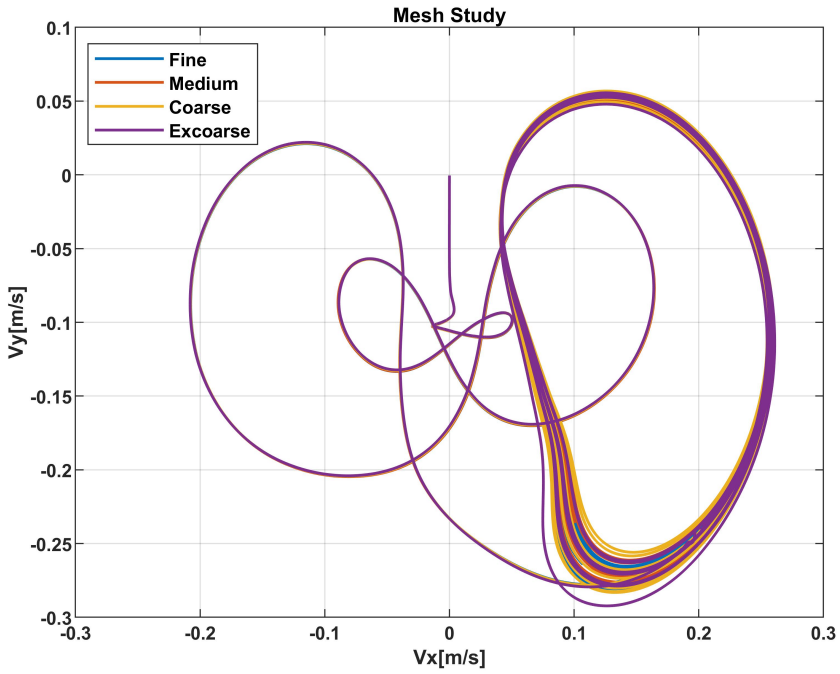

Figure 5.28: CFD mesh study simulation at 0^0 drop showing Vx versus Vy of tumbling plate at $\beta = 1/8$

In order to ensure a stable and accurate solution for the initial speed case, the time step is reduced to $2.5E^{-4}s$ to satisfy the $CLF \leq 0.5$. The mesh study dependence was performed using a finer and coarse mesh as shown in Figure 5.24 through to Figure 5.28. The medium mesh is used for the initial velocity case since from the above results for unsteady aerodynamics of falling plates is not sensitive to the mesh study and convergence is reach with medium mesh.

5.9.2 Uncertainty Measurement of Tumbling Plate at 0^0

Since experimental results for the *0* degree drop are not available to validate the numerical results, a grid convergence index *(GCI)* based on the Richardson extrapolation approach is used to estimate the solution errors as shown in Figure 5.30 with order of convergence Figure 5.31. The trajectories and velocities as shown in Figure 5.32 , with the factor of safety Figure 5.33 are performed based on three mesh levels with a refinement ratio of $\sqrt{2}$ the assume error of the grid is determined based on Equation (3.43), the order of convergence is calculated based on Equation (3.49) with the discretization error Equation (3.50). In addition, the uncertainty was estimated by replacing the observed order of accuracy, p, in the GCI from Equation (3.43). The results of the mesh sensitivity study shown in Figure 5.24 through to Figure 5.28 shows that the mesh converged with medium mesh. The uncertainty measurement in Table 5.5 shows a percentage convergent node of 61% - 75%.

The factor of safety in Figure 5.33 satisfied the procedure for the *GCI* requirement to show whether the suggested *FS* of *1.25* agrees with Phillips and Roy (2012, 2017),but in Figure 5.30 some nodes diverged with some converging, the measured order of accuracy in Figure 5.31 and Figure 5.32 showing good convergence but with high uncertainty in Y position as shown in Figure 5.34, therefore refinement for mesh study is not required.

Table 5.5: 0^0 drop time study computed uncertainty of X & Y position with horizontal, vertical and rotational velocities mesh study

	X position	Y position	Vx velocity	Vy velocity	Vz velocity
Number of monotonically convergent nodes	1421	1994	1234	1319	1238
Monotonically convergent nodes percentage of total	31.88%	44.73%	27.69%	29.59%	27.78%
Number of oscillatory convergent node	1763	883	1705	1429	1582
Oscillatory convergent nodes percent of total	39.56%	19.81%	38.25%	32.06%	35.49%
Total number of convergent nodes	3184	2877	2939	2748	2820
Percentage convergent nodes	71.44%	64.55%	65.94%	61.66%	63.27%

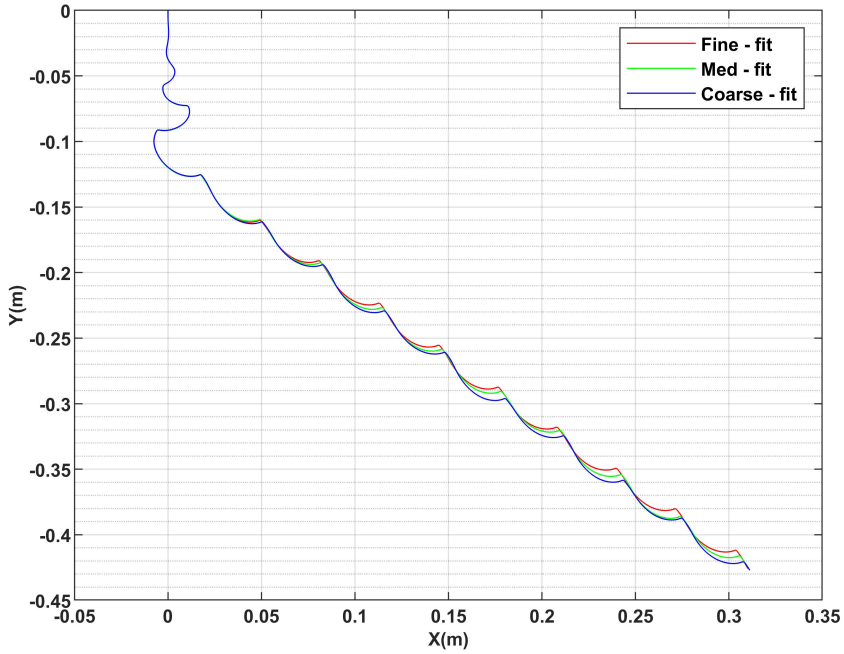

Figure 5.29: Time study of 0^0 drop uncertainty measurement of fine, medium and coarse trajectories

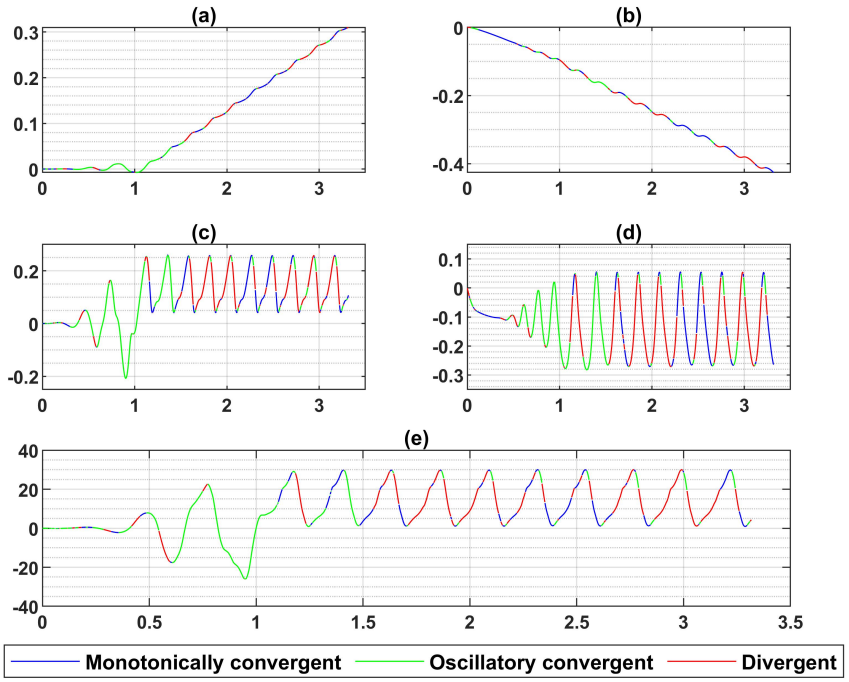

Figure 5.30: Time study of 0^0 drop numerical convergence uncertainty measurement of (a) X position state of each node, (b)Y position state of each node, (c)Vx position state of each node, (d) Vy position state of each node, (e)Vz position state of each node

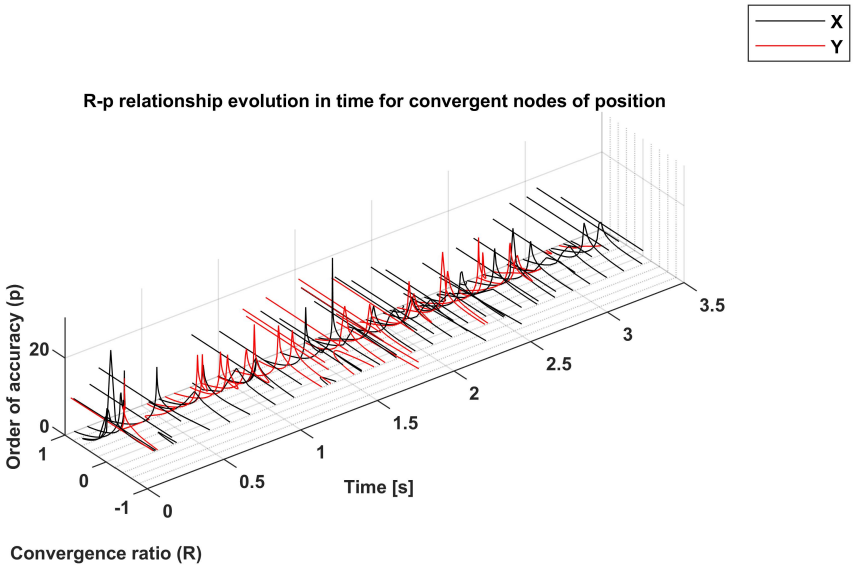

Figure 5.31: 0^0 drop order of accuracy measurement of X & Y position mesh study

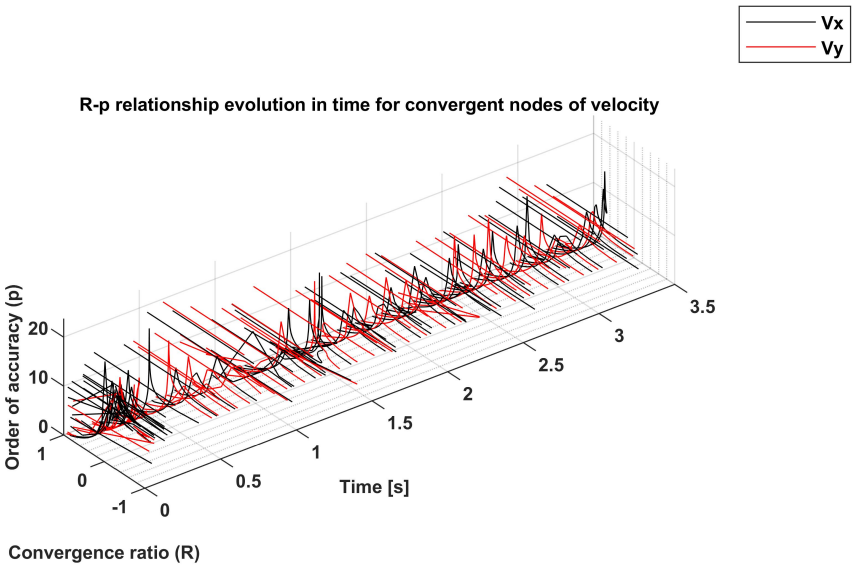

Figure 5.32: 0^0 order of accuracy measurement of Vx & Vy Velocity Mesh Study

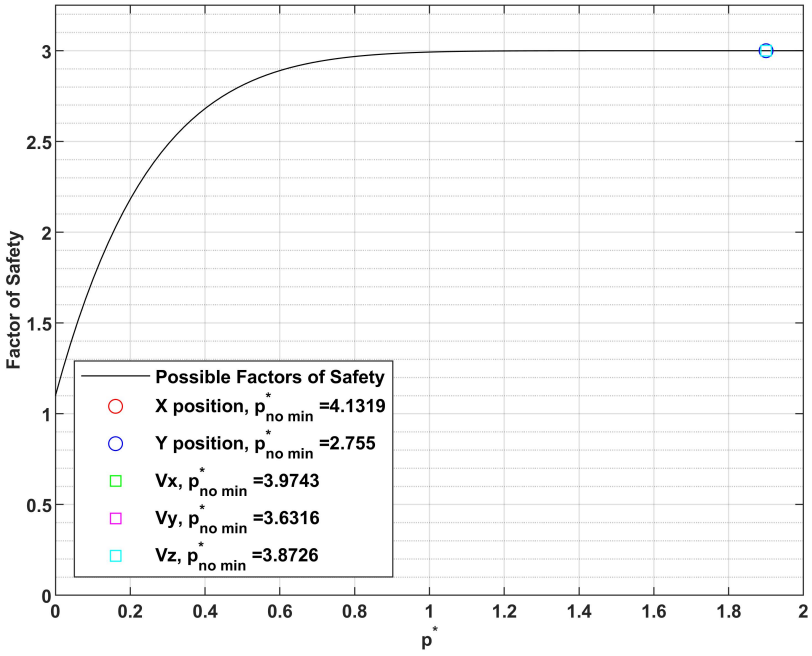

Figure 5.33: 0^0 drop time study computed factor of safety

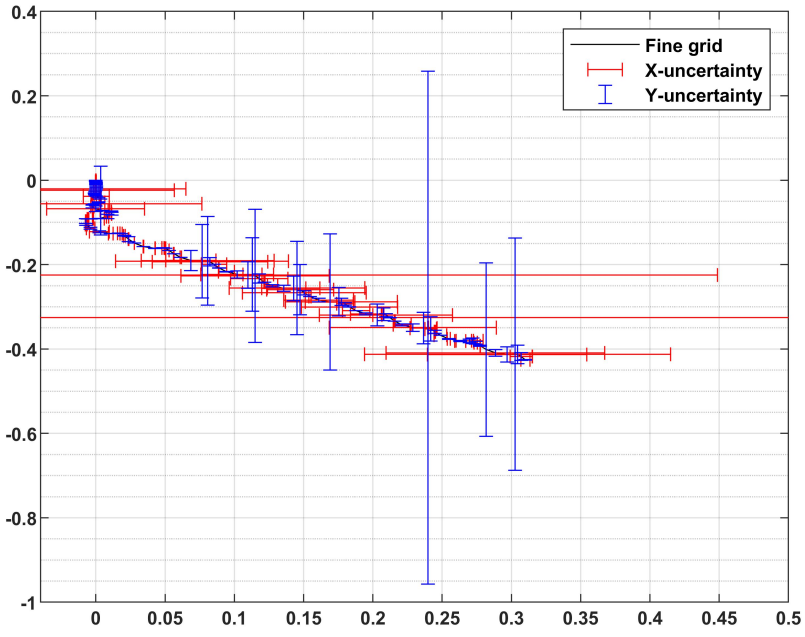

Figure 5.34: 0^0 drop error measurement of trajectory of tumbling plate time study

5.10 Initial Velocity Numerical Results

Despite the extensive work carried out on the tumbling motion of rectangular plates, discs, and leaves freely falling or fixed in quiescent fluid, little is known about the motion of tumbling plates with initial speed. The free-falling motion of a thin rectangular plate with initial speed is investigated, and the motions are classified into three phases: the initial phase, the transition phase, and the periodic tumbling oscillation phase.

Table 5.6: Measured average horizontal velocity, vertical velocity and angular velocity with different initial speed

Initial velocity (V_I(m/s))	Average horizontal velocity (Vx(m/s))	Average vertical velocity (Vy(m/s))	Average angular velocity (Vz(rad/s))
0	0.677	-0.134	11.455
1	0.875	-0.142	13.228
2	0.934	-0.133	12.709
3	0.933	-0.137	12.709
4	0.986	-0.134	13.115
5	1.002	-0.131	13.283
7	1.004	-0.138	12.598
8	1.044	-0.134	13.075
9	1.045	-0.134	13.075
10	1.050	-0.137	12.901
11	1.028	-0.127	15.269
12	1.055	-0.138	12.799
13	1.055	-0.138	12.799
14	1.047	-0.138	12.496
15	1.069	-0.133	13.080
20	1.113	-0.126	13.478
25	1.077	-0.130	13.300

Table 5.7: Measured average fluid forces X & Y, fluid torque and angle of descent with different initial speed

Initial velocity (V_I(m/s))	Average horizontal force (Fx(N))	Average vertical force (Fy(N))	Average torque (M(N.m))	Average rotational angle (θ(Deg))
0	0.002	0.001	8.602E-08	12.314
1	0.004	1.346E-06	3.991E-07	20.109
2	0.020	0.002	2.707E-07	8.298
3	0.020	0.002	2.707E-07	8.298
4	0.026	0.002	8.460E-07	8.833
5	0.032	0.002	8.992E-07	8.833
7	0.045	0.002	2.846E-07	9.722
8	0.050	0.002	7.995E-07	10.114
9	0.050	0.002	7.995E-07	10.114
10	0.056	0.002	7.945E-07	10.033
11	0.058	0.002	8.423E-07	9.112
12	0.062	0.002	8.159E-07	9.955
13	0.062	0.002	8.159E-07	9.955
14	0.086	0.003	3.112E-07	10.692
15	0.098	0.002	4.693E-08	12.379
20	0.137	0.002	8.615E-08	13.003
25	0.099	0.001	6.630E-08	12.445

Table 5.8: Measured non-dimensional average horizontal velocity, vertical velocity, fluid forces X & Y, fluid torque and frequency with different initial speed

Average initial velocity (V_I^*)	Average horizontal velocity (Vx^*)	Average vertical velocity (Vy^*)	Average horizontal force (Fx^*)	Average vertical force (Fy^*)	Average torque (M^*)	Average frequency (F^*)
0	0.591	-0.817	0.022	0.010	3014.180	0.088
6	0.875	-0.862	0.050	0.001	13985.820	0.096
12	0.513	-0.807	0.151	0.018	32853.300	0.103
18	0.461	-0.835	0.233	0.020	9483.771	0.096
24	0.486	-0.813	0.299	0.020	29642.550	0.101
30	0.463	-0.796	0.363	0.019	31505.960	0.105
43	0.416	-0.839	0.514	0.020	9971.798	0.094
49	0.448	-0.814	0.570	0.021	28013.280	0.101
55	0.448	-0.814	0.570	0.021	28013.280	0.110
61	0.441	-0.833	0.639	0.021	27847.500	0.097
67	0.401	-0.774	0.664	0.026	29512.190	0.124
73	0.433	-0.843	0.705	0.022	28587.050	0.095
79	0.433	-0.843	0.705	0.022	28587.050	0.095
85	0.368	-0.837	0.982	0.029	13004.020	0.094
91	0.953	-0.810	1.120	0.017	1644.345	0.101
122	1.008	-0.769	1.569	0.020	3018.810	0.110
152	0.962	-0.792	1.137	0.011	2323.138	0.106

Table 5.9: Measured non-dimensional average drag coefficient, lift coefficient, moment coefficient, X & Y position, dimensionless Moment of inertia and Reynolds numbers with different initial speed

Average initial velocity (V_I^*)	Average drag coefficient (C_D^*)	Average lift coefficient (C_L^*)	Average moment coefficient (C_M^*)	Average horizontal position (X^*)	Average vertical position (Y^*)	Average dimensionless moment of inertia (I^*)	Average Reynolds number (R_e)
0	1.608	19.266	5.642E+12	0.010	53.771	-9E-06	977.49
6	2.156	0.026	1.216E+02	0.000	68.690	0.893	1031.54
12	5.751	33.777	5.543E+01	0.018	12.018	1.664	965.02
18	8.914	35.591	7.434E+00	0.020	14.359	2.057	998.60
24	10.247	37.323	5.778E+00	0.020	15.847	2.278	973.05
30	12.047	36.135	9.179E+00	0.0186	17.139	2.396	952.70
43	16.965	34.721	2.022E-01	0.020	19.896	2.541	1003.69
49	17.398	39.118	6.431E-01	0.021	20.755	2.619	973.26
55	17.398	39.118	6.431E-01	0.021	20.755	2.619	973.26
61	19.329	37.453	1.543E-01	0.021	21.440	2.658	996.17
67	20.918	54.109	1.450E-01	0.026	22.891	3.914	925.71
73	21.116	38.587	1.126E-01	0.022	22.115	2.702	1007.76
79	21.116	38.587	1.126E-01	0.0222	22.115	2.702	1007.76
85	29.873	51.444	6.211E-03	0.029	25.036	2.815	1001.17
91	32.671	32.589	1.650E-03	0.017	66.904	2.844	968.75
122	42.195	40.899	2.532E-03	0.020	68.147	2.899	919.59
152	32.665	21.876	7.839E-04	0.011	66.230	2.823	946.87

Figure 5.35 measured the trajectories while Figure 5.36 through to Figure 5.39 measured the horizontal velocity, vertical velocity, angular velocity, and phase plot of a falling plate with initial speed. As the plate moves with initial speed and falls, the trajectories glide to either the left or right direction with different initial speed, but the movement is stochastic as compared to the trajectory of a falling plate with

zero speed. It was also observed that the initial steady fall with fluttering in the $0m/s$ drop changes with different initial speed. At the same time, long gliding section was observed before periodic tumbling with increased initial speed. Similarly, the slope of the gliding sections with the particle nutation angle is considered lower or higher depending on the initial speed as shown in Table 5.7 to Table 5.9 measured average descent angle, but the nutation angle is higher with $1m/s$ initial speed. In the transition phase, the plate rotates 360^0 before fluttering and then tumbles in either a left or right direction depending on the initial speed. It is also observed that the long gliding in the transition phase with different initial speeds is caused by the flow as shown in Figure 5.49 but the direction of gliding motion changes; however, this research did not investigate the effect of vorticity on the trajectory and gliding motion in the left or right direction due to the vortex formation. The measured translational distances between freely falling plates with initial speed are approximately equal to tumbling plates with different aspect ratios, as reported by Wang et al. (2013).

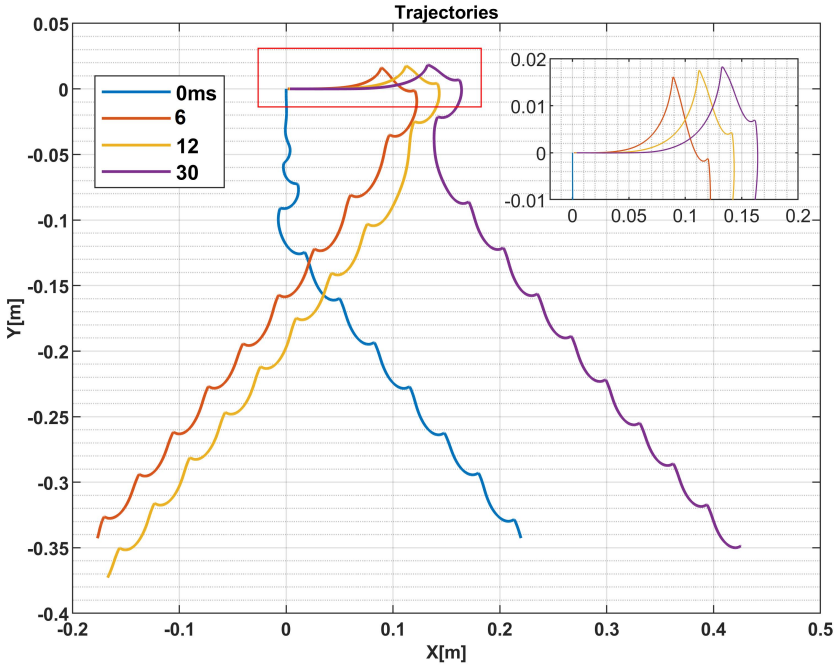

Figure 5.35: Computed trajectories of tumbling plate with different initial speed

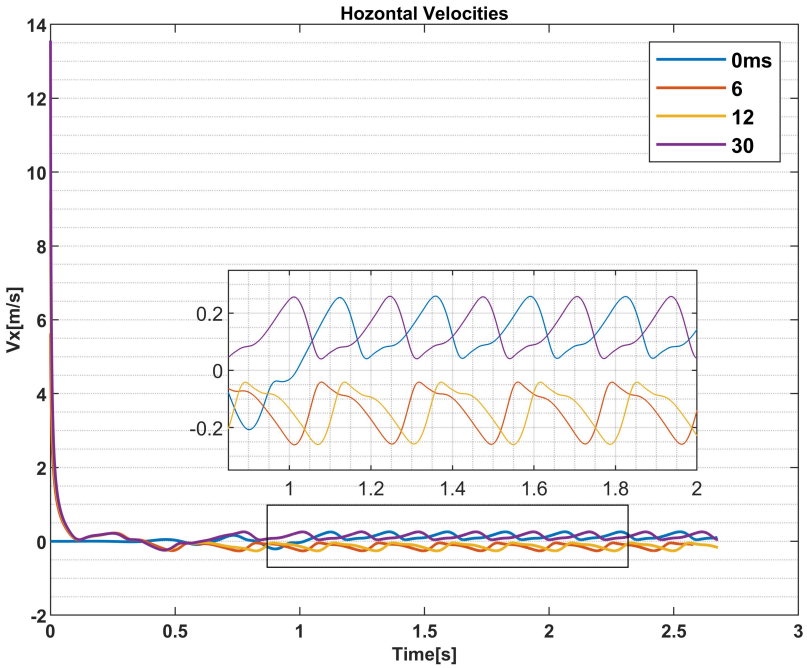

Figure 5.36: Computed horizontal velocities of tumbling plate with different initial speed

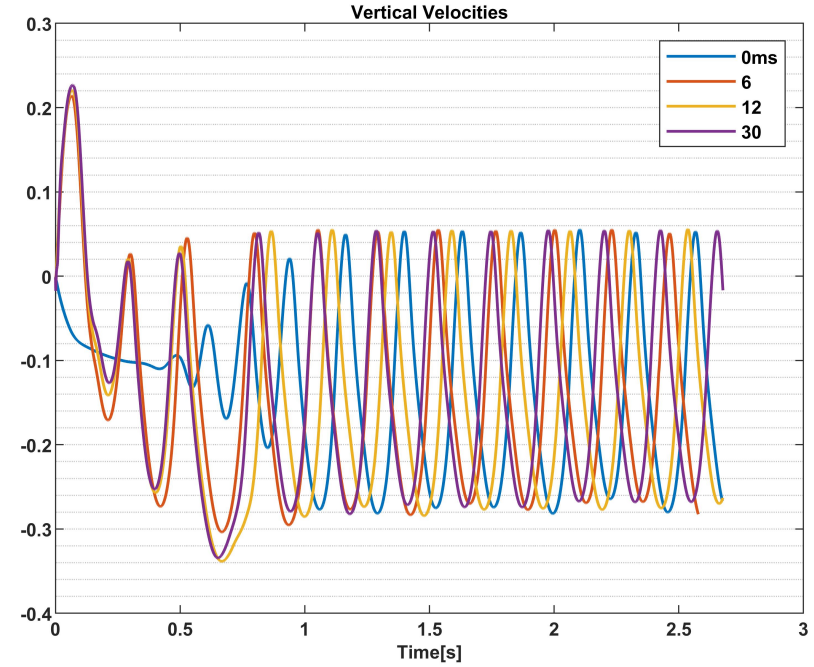

Figure 5.37: Computed vertical velocities of tumbling plate with different initial speed

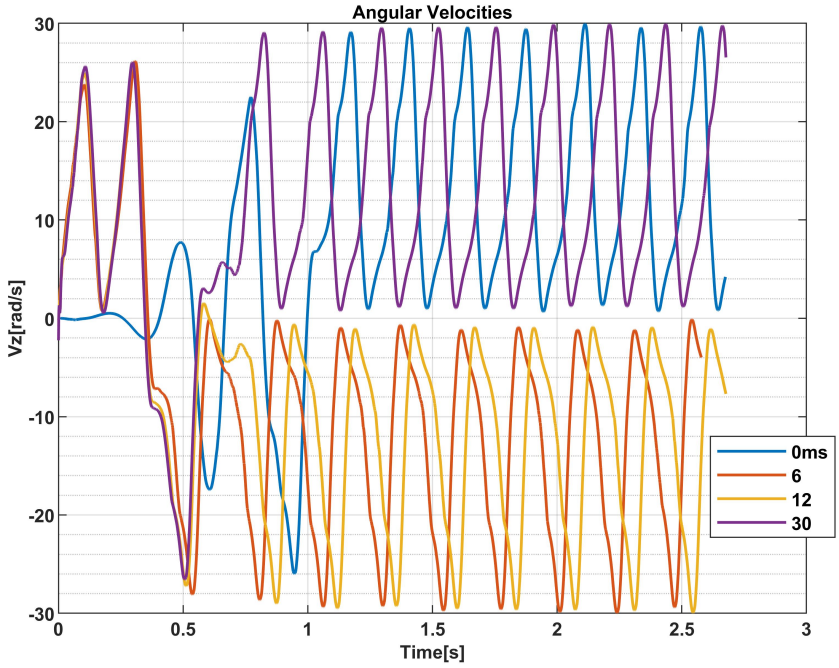

Figure 5.38: Computed angular velocities of tumbling plate with different initial speed

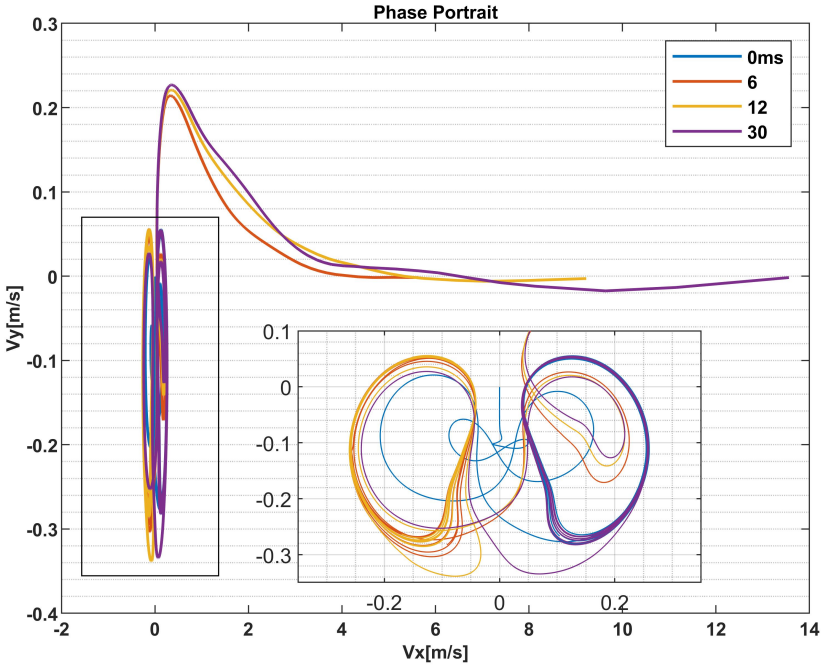

Figure 5.39: Computed Vx^* versus Vy^* of tumbling plate with different initial speed

It was observed in Figure 5.41 the measured horizontal velocity is different as the oscillation moves to the left or right with the same vertical velocity as shown in Figure 5.25 The left-gliding horizontal velocity component as a function of time looks similar to the vertical velocity component of different aspect ratio reported by Andersen et al. (2005a). In addition, Figure 5.40 shows the tumbling trajectory of the plate as it moved to the left or right. The trajectories are qualitatively similar, but the phase plot in Figure 5.39 and Figure 5.43 shows a more pronounced period-two tumble motion as the plate moves to the right; a similar phase plot was observed with an elliptical cross-section reported by Andersen et al. (2005b).

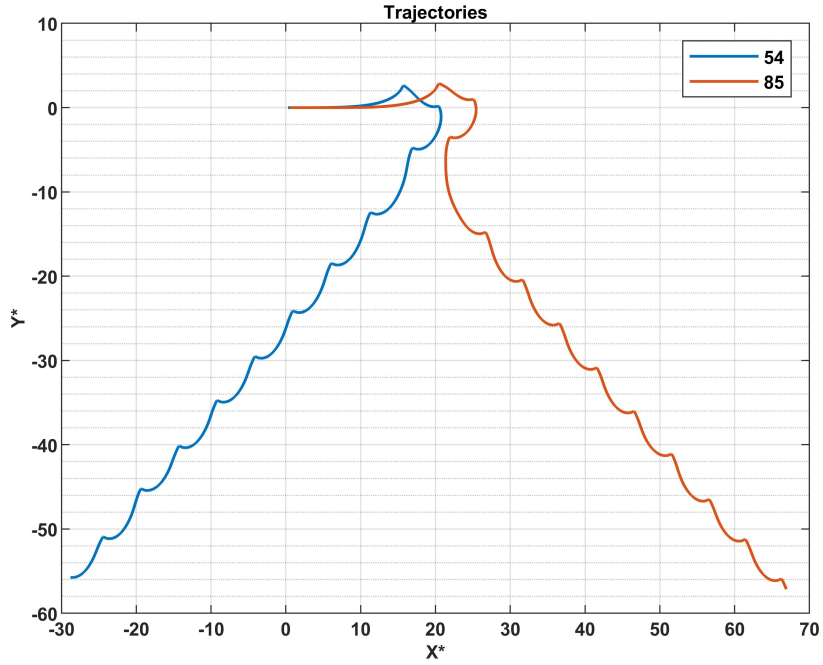

Figure 5.40: Computed left and right trajectories of tumbling plate with different initial speed

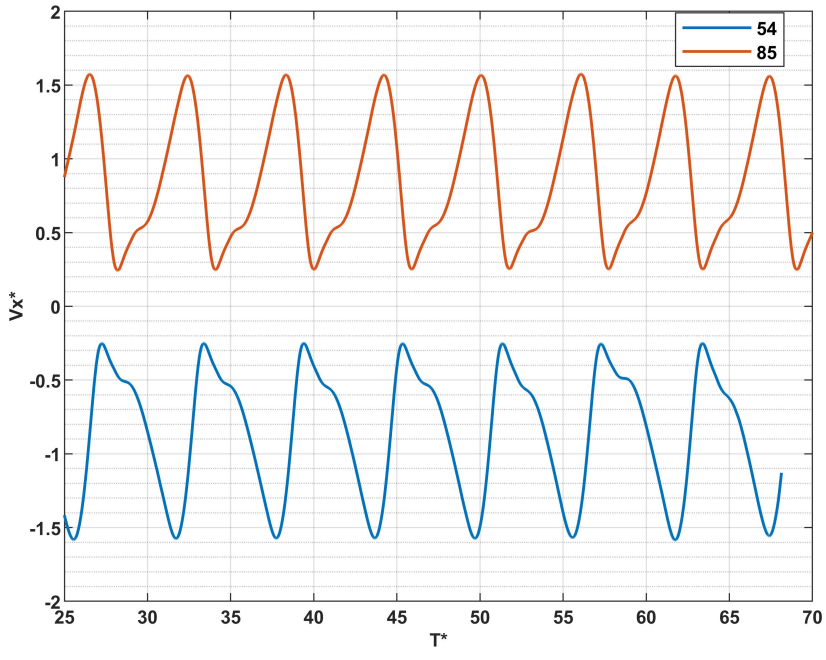

Figure 5.41: Computed left and right horizontal velocity of tumbling plate with different initial speed

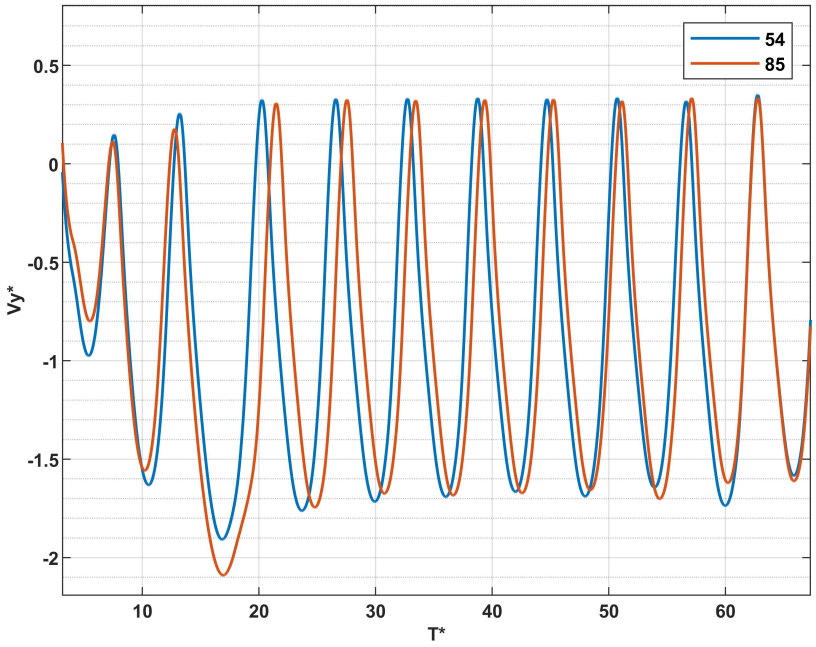

Figure 5.42: Computed left and right vertical velocity of tumbling plate with different initial speed

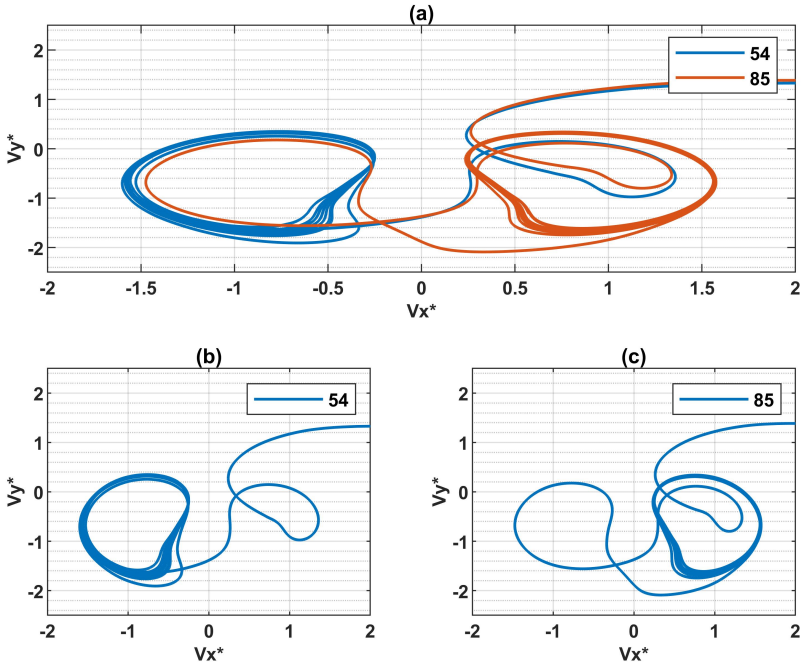

Figure 5.43: Computed (a) left and (b) right of Vx* versus Vy* of tumbling plate with different initial speed

Figure 5.44 shows a period-three tumbling motion. In previous studies, Andersen et al. (2005a,b) reported a period-two tumble motion for a large aspect ratio > 15 with fast rotational behaviour and the centre of mass fluctuating along its mean trajectory, while Wang et al. (2013) reported a different pure rotational tumbling motion with steady translational motion similar to a fixed auto-rotational plate with its centre perpendicular. In this present research, we observed a period-three tumbling motion with a fast rotational behaviour and the centre of mass fluctuating along its mean trajectory, similar to Andersen et al. (2005a,b) reported period-two tumbling motion. However, Wang et al. (2013) concluded that the distinction between the two-motion is as a result of change in I^* , as also reported by Lugt (1983) who started that if I^* is larger than 10 the motion of the tumbling plate is closer to auto-rotation. The new triple-period oscillation observed in Figure 5.44 with a high frequency and low decent angle, horizontal, and vertical velocities as shown in Table 5.7 and Table 5.8 as compared to freely falling tumbling with no speed, for an aspect ratio $\gamma^* > 15$ and $I^* < 0.5$ reported by Andersen, Andersen et al. (2005a,b).

Wang et al. (2013) reported a purely rotational tumbling motion with steady translation motion and double period rotation identified through Fourier analysis with aspect ratio $\gamma^* = 10$, the phenomenon disappeared for a smaller aspect ratio. It was also observed from Figure 5.44 a similar descent trajectory first reported by Esteban et al. (2020) where a disc laterally moves about $10D$ of the disc and falls chaotically with the influence of turbulence. Similarly, a long gliding is observed from Figure 5.35 as initial speed is applied to the plate, with an initial phase of fluttering, and then the plate tumbles to the left or right.

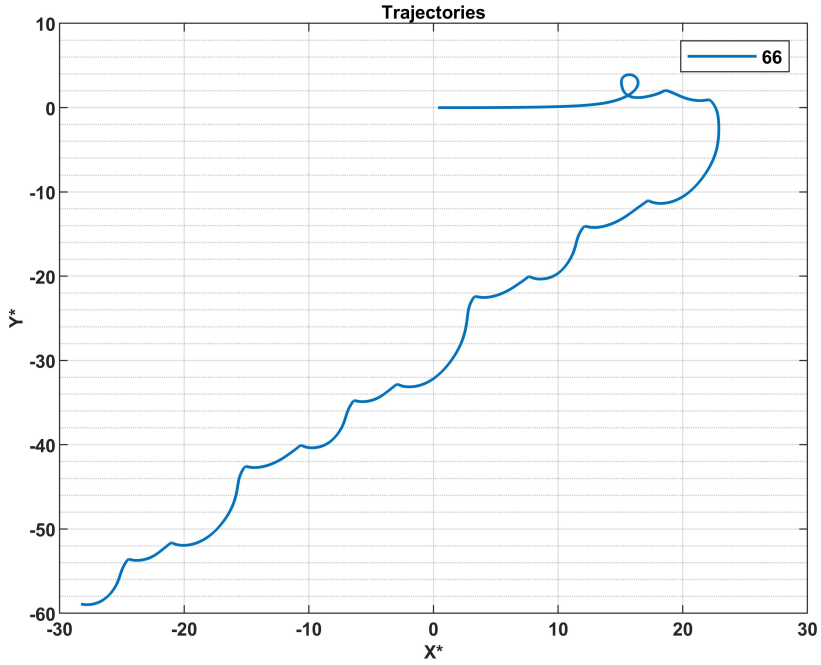

Figure 5.44: Computed trajectories of tumbling plate with triple periods

Figure 5.45 shows the measured average kinematics of a freely tumbling plate with different non-dimensional speeds. Table 5.8 and Table 5.9 present a summary of the non-dimensional parameters. The results show a higher average descent angle with a lower average rotational frequency and higher horizontal velocity and lower vertical velocity values for the plate with the same aspect ratio as reported by Wang et al. (2013), Dupleich (1949) and Hirata et al. (2009). Furthermore, Wang et al. (2013) concluded that the average vertical velocity and the descent angle decrease as a function of aspect ratio, while the average horizontal velocity increases and the angular velocity and the non-dimensional frequencies increase as aspect ratio increases. However, in the present studies, descent angles, horizontal velocities, vertical velocities, rotational frequencies, and angular velocities are stochastic for a plate with the same aspect ratio but with a different initial speed.

Figure 5.47 shows the plot of average force coefficients with different non-dimensional speeds; the average drag and lift coefficients increase with different speeds. Wang et al. (2013) also reported an increase in lift coefficient as aspect ratio increased

but a decrease in drag coefficient as aspect ratio increased. Hirata et al. (2009) also reported a decrease in drag coefficient as aspect ratio increased. In addition, the observed translational amplitude of horizontal and vertical position in Figure 5.46 shows an increase in vertical amplitude with a random probability pattern that may not be predicted precisely.

Finally, Figure 5.46 shows the measured average drag and lift coefficients with X^* & Y^* positioning varying with different speeds, the drag coefficient increases as the speed increases and reaches its maximum at an initial speed of $20m/s$ as shown in Table 5.8 and Table 5.9, from Figure 5.35 the results of the measured trajectories show a maximum speed at which a plate can reach before gliding. The increase of drag coefficients at decreasing aspect ratios was initially reported by Wang et al. (2013).

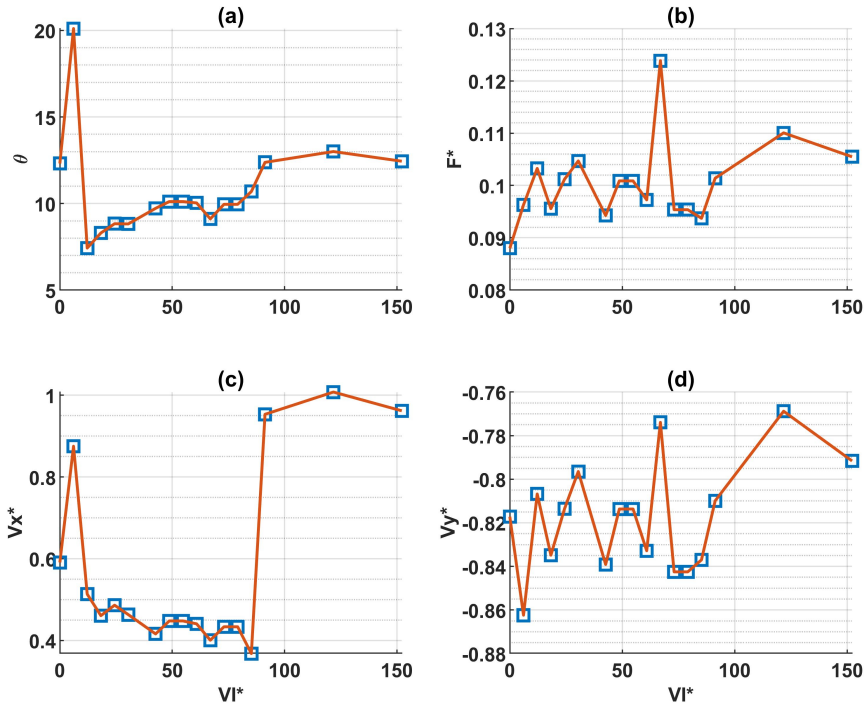

Figure 5.45: Computed average values of (a) decent angle (b) rotation frequency, (c) horizontal velocity (d) vertical velocity versus initial speed

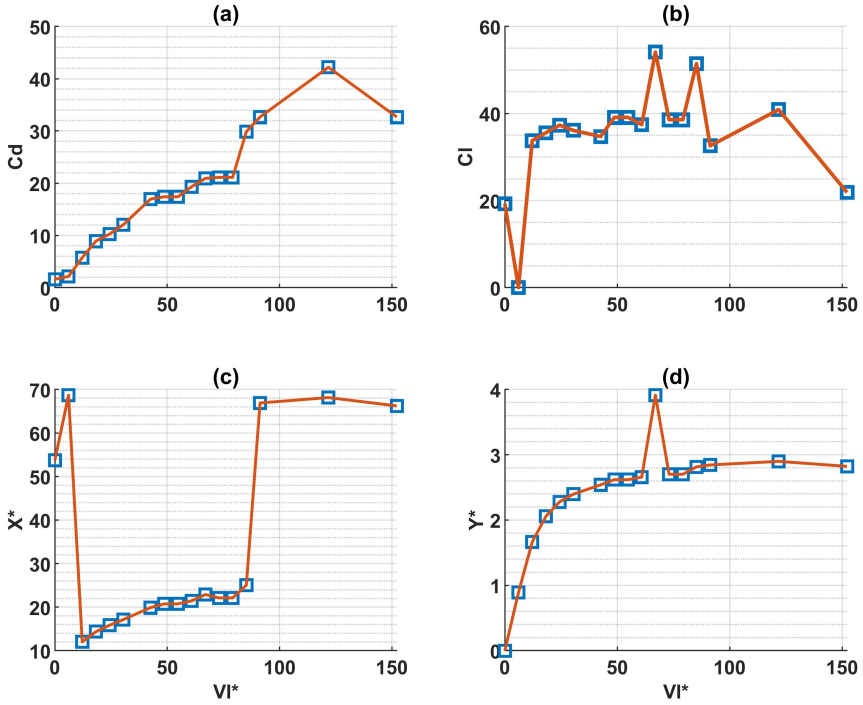

Figure 5.46: Computed average values of (a) drag coefficients (b) lift coefficients (c) X position (d) Y position versus initial speed

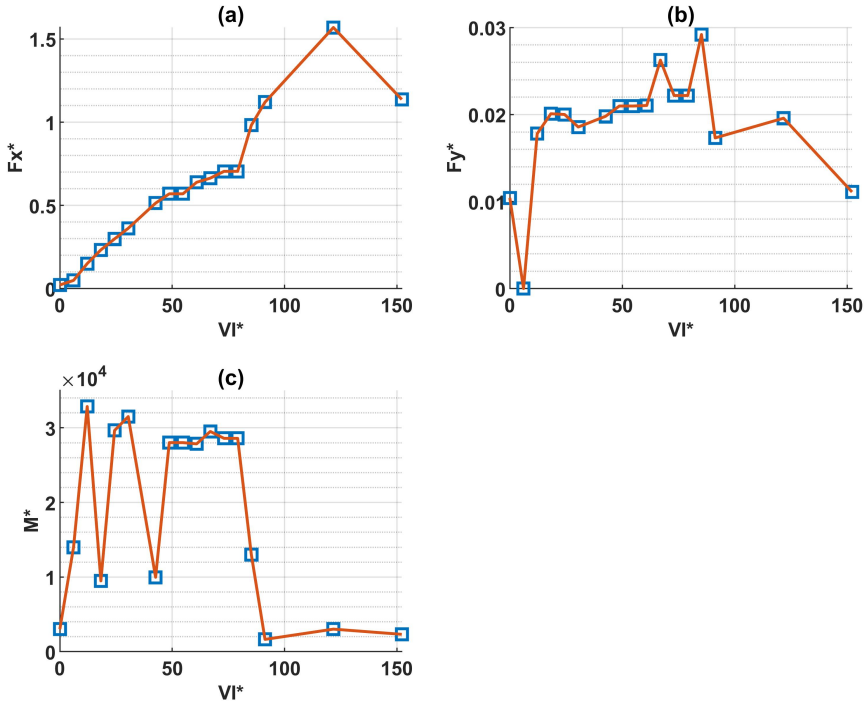

Figure 5.47: Computed average values of (a) horizontal forces (b) vertical force (c) moment versus initial speed

The phase plot in Figure 5.43 and horizontal velocity in Figure 5.41 and Figure 5.42, show a double period motion similar to motion presented by Andersen et al. (2005a) and a single periodic tumbling present by Wang et al. (2013). Also changes occur in descent angle, horizontal velocity, vertical velocity, and frequency at the range of different initial speeds as shown in Figure 5.29, but the results are not dependent on the initial speed. From the mean descent velocity of the rectangular plate falling with initial speed in Table 5.7 and the dimensionless moment of inertia and the Reynolds number in Table 5.9 with the phase diagram Figure 5.48 it was confirmed that they lie within the Re - I^* domain corresponding to a freely falling tumbling plate.

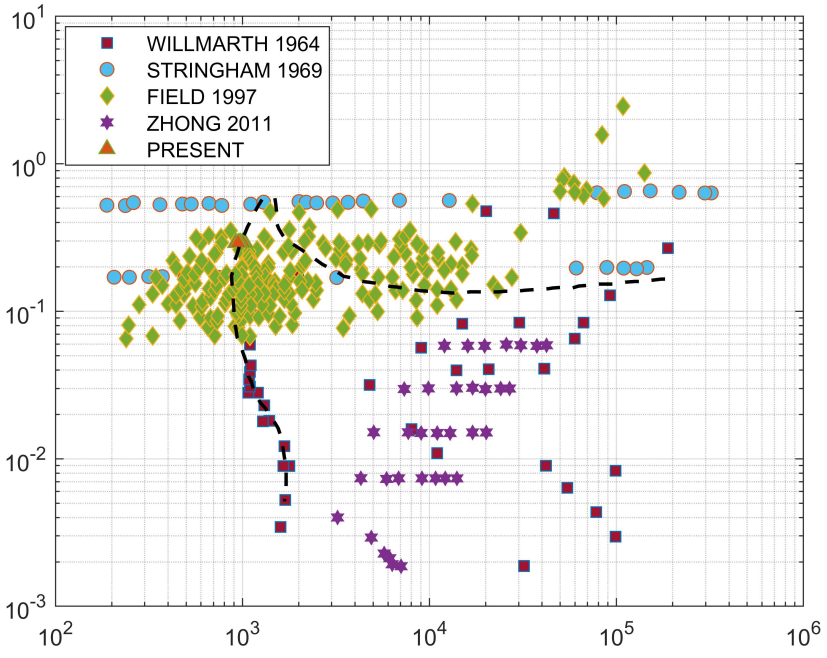

((a)) Phase diagram full

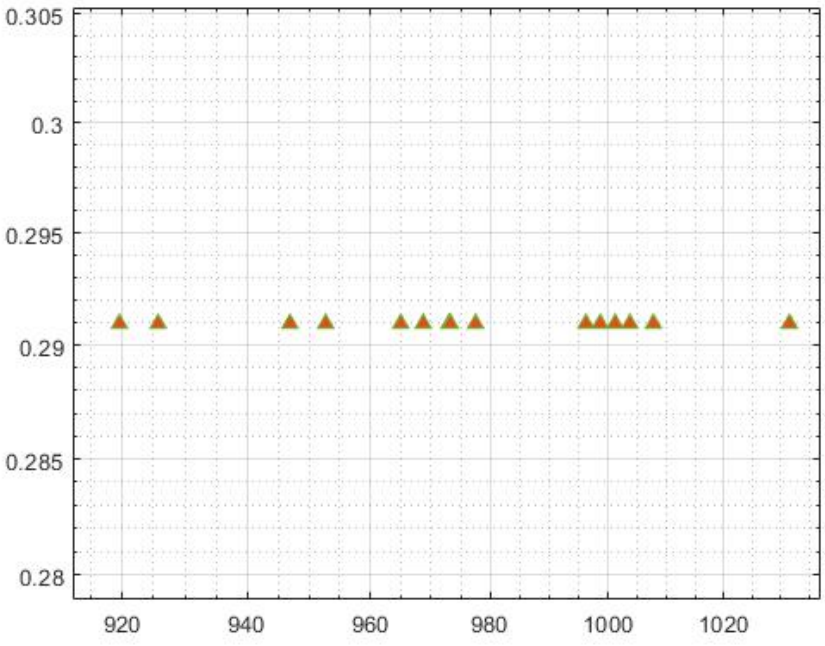

((b)) Phase diagram subplot

Figure 5.48: Phase diagram of falling tumbling plate with different initial speed

5.10.1 Vortex Formation and Wake Structure

It is observed from previous studies by Andersen et al. (2005a) and Ern et al. (2011) that the motion of a thin plate could be affected more easily by the surrounding fluid, which will lead to complex trajectories such as periodic oscillation or tumbling and will induce instantaneous vortex shedding. As plates fall in a viscous fluid, they form a vortex around which the surrounding fluid alters the forces that act on them. Andersen et al. (2005a) and Wan et al. (2012) show the vortex shedding and wake pattern of a freely falling tumbling and fluttering plates, while Ern et al. (2011) studied the lift generated from the boundary layer separation and vortex shedding of freely rising or falling bodies in a viscous fluid. Zhong et al. (2013) experimentally reported a different shedding pattern than that of kàrmàn vortex shed with a freely falling plate of Reynolds number greater than *2000*. In addition to a freely falling body, fixed plate vortex shedding was studied extensively, Figure 5.49 shows the vortex formation and wake structure of a tumbling plate with initial speed, (a) $\sim$ (c) shows the vorticity of the plate moving with initial speed before gliding, a long gliding with centre of mass elevation seen in (h), and a short gliding without centre of mass elevation in (h) $\sim$ (j). However, at the turning point seen in (e) $\sim$ (l) a vortex pair is formed by breaking up as the plate turns, glides, and forms a wake. As the plate glides and turns 360^0 wakes develops and becomes unstable, breaking up into vortices before gliding. Furthermore, movement of the plate left or right due to vortex and wake formation is not discussed.

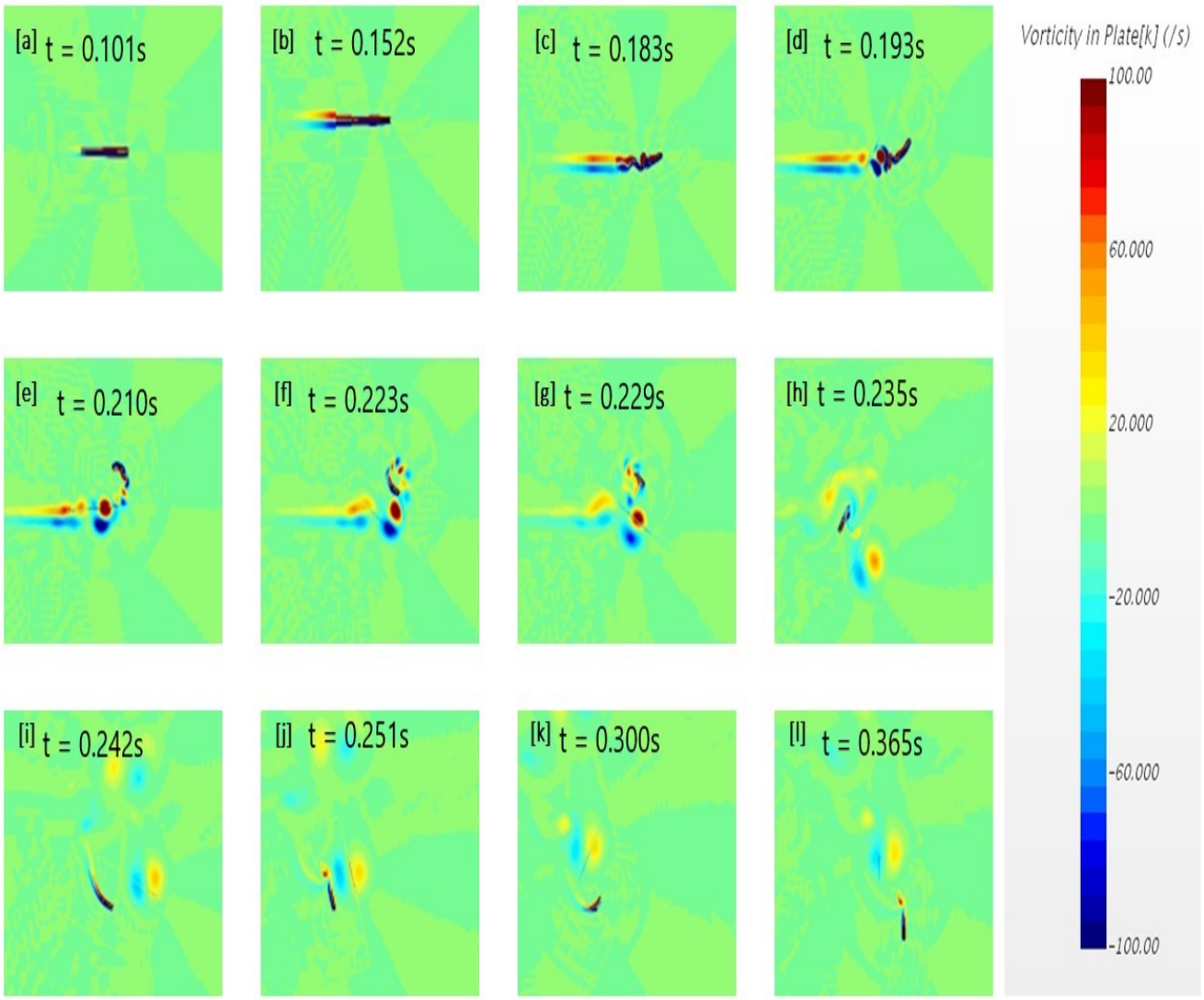

Figure 5.49: The vorticity around a tumbling plate with 11m/s initial speed

Chapter 6

ACHIEVEMENTS, CONCLUSION AND FUTURE WORK

This chapter summaries the research findings performed in this thesis. The completion of the aims and objectives is assessed and presented in chapters 4,5&6. Future work is then suggested based on the findings of the thesis.

6.1 Against the Objectives

The study of the motion of solids in fluids has always triggered interest in the scientific and research community. This rich, dynamic behaviour dates back to the foundation of modern mechanics. However, understanding dynamic behaviour has been a major issue in both engineering and scientific communities for centuries. This thesis presented an investigation into three different studies.

Objective 1. Experimental investigation of heavy plates falling freely in a *3D* viscous fluid and determined the transitions from zigzag to tumbling motions of the plates at the range of Reynolds number *270* to *23000*, dimensionless moment of inertia up to *23* and aspect ratio *5-39*. The objective is to extend the mapping of heavy plates from previous literature of Lau et al. (2018) and further understand the falling trajectories and bistability, since both experimental and numerical investigation of heavy plates at large I^*, Re and γ^* remain scarce.

- Using the state-of-the-art technique, experimentally, the transitions from zigzag

to tumbling motions of freely falling heavy plates in three-dimensional viscous fluid at the range of Reynolds number *270* to *23000*, dimensionless moment of inertia up to *23* and aspect ratio *5-39* was investigated. Because experimental and numerical studies of heavy plates at large I^*, Re and γ^* remain scarce, it is desirable to extend the mapping of heavy plates from previous literature.

The above objective was met in **Chapter 2, Chapter 3 & Chapter 4**, which presented the critical literature review of thin and heavy plates freely falling, with the experimental setup in **Chapter 3** and research findings in **Chapter 4**.

Objective 2. The accuracy of the numerical *CFD* method is of great interest in the academic community, to capture the physics of free-falling plates numerically. The objective is to develop a numerical model and validate it against experimental work of previous literature and determine numerical uncertainty since complex flow regimes during the motion of a freely falling plate and the errors generated from the computational techniques make the numerical modelling of a falling plates a challenging task. But computational models are becoming more and more important for predicting how things will behave when they are falling, staying still, or rising. However, assumptions and simplifications made in numerical simulations can lead to differences between experimental and numerical models, which can sometimes make numerical models less accurate.

- Develop a numerical model to investigate the *2D/3D* motion of a falling plate by using a CFD technique to validate the experimental model of Andersen et al. (2005a) and numerical model of Jin and Xu (2008); and estimate the numerical uncertainty and errors of tumbling rectangular plate during free-fall.

The above objectives was addressed in **Chapter 3**, first a numerical model using overset method was used and finally **Chapter 5** shows the research findings with good convergence in both mesh and time study, numerical errors were also determined and concluded with a good measured percentage convergence of nodes is achieved in both mesh and time study.

Objective 3. A number of parametric studies have been carried out previously to investigate the motion of a freely falling plate. Some authors take into account the effect of aspect ratio Wang et al. (2013), density ratio Wang et al. (2016), turbulence Esteban et al. (2020), Reynolds number Andersen et al. (2005a,b), or aerodynamics of multiple free-falling plates Kushwaha and De (2020) and Shape optimization Vincent et al. (2020). The falling plate with initial speed was never investigated. The objective is to investigate the effect of initial speed on the freely tumbling body under the influence of gravity.

- Develop a numerical model to investigate the motion of a free-falling plate numerically with an initial velocity.

The above objective is met in **Chapter 3**, by numerically modelling the dynamic of the tumbling plate using overset mesh, and **Chapter 5** analysed the motion and presented the research findings.

6.2 Conclusions

In the first part of this dissertation, the motions of heavy plates was investigated to determine the sensitivity of the initial angle of release. It was concluded that the motion is similar to the three-dimensional dynamics of freely falling bubbles with erratically wobbling behaviour and zigzag motion, but the motion changes with different oscillations of both vertical and horizontal velocity depending on the initial angle of release, but the vertical velocity is stochastic and does not depend on the initial release angle. As the Re increases, the frequency and pattern of oscillation increase with a decrease in aspect ratio and a high lift compared to previous literature. It was also observed that the initial release angle in the underwater case shows double period motion, with a zigzag and fluttering motion with a reducing vertical velocity depending on the initial angle of release. The motion is classified as periodic zigzag motion with an inclination of the axis and velocity of oscillation almost out of phase. However, in the present findings, both vertical, horizontal, and rotational

velocities are stochastic and do not depend on the initial release angle. Similarly, bistability depends on the initial angle of release from zigzag to tumbling motion, whereas the trajectory of fluttering and tumbling is independent of the initial angle of release, as reported from early findings on the aerodynamics of light plates falling in viscous fluid. In addition, early conclusions from the phase diagram of heavy plates report that plates above the upper boundary (red dot) will never tumble at any release angle, and plates below the lower boundary (red dot) will develop into tumbling and will not fall steadily. In the present research, plates fall steadily at the lower boundaries. Finally, Lau et al. (2018) reported a critical initial angle of 58^0, 75^0 , and 51^0 that will set plates from stable falling to tumbling. However, in the present study, a critical initial angle of 20^0, 30^0, 35^0 and 45^0 was reported depending on the aspect ratio.

The second part describes the validation of numerical results against experimental and numerical findings in previous literature. The numerical results adopted in this study provided realistic results of tumbling plate dynamics and correctly predicted the trajectories, forces, and torque but with phase shifts. The solution for the local uncertainty of the tumbling plate with the factor of safety and the order of convergence shows *90% - 99%* X and Y position and *98%* translational and rotational velocity convergence in the mesh study, while *75% - 84%* X & Y position, *73%* to *75%* translational and rotational velocity in the time study.

Finally, the third part investigated the motion of tumbling plates with different initial speeds and concluded that the trajectories move to either the left or right with different initial speeds, but the movement is stochastic and not dependent on initial speed. It was also observed that the measured horizontal velocity is different as the oscillation moves to the left or right with the same vertical velocity. The phase movement to the left looks similar to the double period motion in previous literature, while the phase movement to the right is a single periodic tumbling present in previous literature. However, changes occur in descent angle, horizontal velocity, vertical velocity, and frequency at a range of different speeds, and the results

are not dependent on the initial speed. It was confirmed that the I^* - Re domain corresponds to a freely falling, tumbling plate. A new triple-period oscillation was observed and reported for the first time with a high frequency, and low decent angle, horizontal, and vertical velocities. The measured average drag and lift coefficients with X^* & Y^* positioning vary with different speeds. The drag coefficient increases as the speed increases and reaches its maximum at an initial speed of *20m/s*. The results of the measured trajectories show a maximum speed at which a plate can reach before gliding.

The movement of a rigid body dropped in water and air has a wide range of scientific and industrial applications. Predicting and estimating the potential flight trajectories and impact energy of a piece of debris, such as a meteor shower falling, is frequently of scientific interest. However, a better understanding of the unsteady aerodynamic behaviour involved in falling debris flight is required, as is the development of more complete numerical models for accurately simulating debris flight trajectories in realistic conditions. Dropped objects are also a leading cause of fatalities and serious injuries in the offshore oil, gas, and renewable energy industries. Objects may be dropped during lifting or any other offshore operation, and concerns about health, safety, and the environment, as well as potential structural damage, necessitate forecasting where and how a dropped object will move underwater and in the air. The results presented above will aid in estimating potential flight trajectories and determining the impact energy of drop objects.

6.3 Future Work

To reduce the limitation and expand the capabilities, in future work, further development and more study are required for both freely falling heavy plates and thin plates with initial speed:

- Establish relationship between I^*, Re and initial speed
- Increase the drop length of the experiment to determined more oscillations,

and determine the critical angle, by increasing the initial angles of release by 0.5^0 - 1^0

- For the underwater case more camaras are needed to capture the trajectories of the moving object

  35^0 for fluttering and 0^0 for tumbling.

- Experimental and numerical determination of flow fields around the plates for the initial velocity case, to determine the effect of vorticity, velocity fields and pressure fields on the dynamics of the plate

- The effect of shape and influence of aspect ratio & density ratio on the dynamics of free-falling plate with initial speed

- Experimental validation of free-falling plate with initial speed and expanding the phase plot

- The physics of both double period and triple period needs to be investigated extensively

Bibliography

C. Lee, Z. Su, H. Zhong, S. Chen, M. Zhou, and J. Wu, Journal of Fluid Mechanics **732**, 77 (2013), ISSN 0022-1120, URL https://www.cambridge.org/core/article/experimental-investigation-of-freely-falling-thin-disks-part-2-transition-of-th A25354C84A40180790641DDF17958B0C.

A. Andersen, U. Pesavento, and Z. J. Wang, Journal of Fluid Mechanics **541**, 65 (2005a), ISSN 0022-1120, URL https://www.cambridge.org/core/article/unsteady-aerodynamics-of-fluttering-and-tumbling-plates/1FC26E817B4D5B91714C9875F070CF8D.

A. Andersen, U. Pesavento, and Z. J. Wang, Journal of Fluid Mechanics **541**, 91 (2005b), ISSN 0022-1120, URL https://www.cambridge.org/core/article/analysis-of-transitions-between-fluttering-tumbling-and-steady-descent-of-falli 7EA576F55B2B0AEC088DCD62795C1372.

W. B. Wang, R. F. Hu, S. J. Xu, and Z. N. Wu, Journal of Fluid Mechanics **733**, 650 (2013), ISSN 0022-1120, URL https://www.cambridge.org/core/article/influence-of-aspect-ratio-on-tumbling-plates/2E2591EE1BFB00E2591A246FBDE04D6F.

L. Vincent, W. S. Shambaugh, and E. Kanso, Journal of Fluid Mechanics **801**, 250 (2016), ISSN 0022-1120, URL https://www.cambridge.org/core/article/holes-stabilize-freely-falling-coins/944D40B0B3FF9D5EF0A3B796D2D27F1B.

E. Lau, J.-D. Zhang, Y. X. Jia, and W.-X. Huang, Journal of Visualization (2018).

P. C. Fernandes, F. Risso, P. Ern, and J. Magnaudet, Journal of Fluid Mechanics **573**, 479 (2007), ISSN 0022-1120, URL https://www.cambridge.org/core/article/oscillatory-motion-and-wake-instability-of-freely-rising-axisymmetric-bodies/FD292CFD0ABB825CF186B71491E51CB1.

R. Zenit and J. Magnaudet, Physics of Fluids **20**, 61702 (2008), ISSN 1070-6631, URL https://doi.org/10.1063/1.2940368.

M. Horowitz and C. H. K. Williamson, Journal of Fluid Mechanics **662**, 352 (2010), ISSN 0022-1120, URL https://www.cambridge.org/core/article/vortexinduced-vibration-of-a-rising-and-falling-cylinder/3A227A9017D663E0F49735BA510A5C7B.

E. H. Smith, Journal of Fluid Mechanics **50**, 513 (1971), ISSN 0022-1120, URL https://www.cambridge.org/core/article/autorotating-wings-an-experimental-investigation/117B6D0CDD5B4725E70A9D1E61123CAB.

J. D. Iversen, Journal of Fluid Mechanics **92**, 327 (1979), ISSN 0022-1120, URL https://www.cambridge.org/core/article/autorotating-flatplate-wings-the-effect-of-the-moment-of-inertia-geometry-and-r
D5E9AE3839FFD1D34F0DD3C2CBCC2252.

H. J. Lugt, Journal of Fluid Mechanics **99**, 817 (1980), ISSN 0022-1120, URL https://www.cambridge.org/core/article/autorotation-of-an-elliptic-cylinder-about-an-axis-perpendicular-to-the-flow/A2DF25C56EFE9AAD6227391B46CA2663.

R. Mittal, V. Seshadri, and H. S. Udaykumar, Theoretical and Computational Fluid Dynamics **17**, 165 (2004), ISSN 1432-2250, URL https://doi.org/10.1007/s00162-003-0101-5.

Nonlinearity **25**, C1 (2011), ISSN 0951-7715, URL http://dx.doi.org/10.1088/0951-7715/25/1/C1.

C. K. Augspurger, American Journal of Botany **73**, 353 (1986), ISSN 0002-9122, URL https://doi.org/10.1002/j.1537-2197.1986.tb12048.x.

J. R. L. Allen, Sedimentology **31**, 227 (1984), ISSN 0037-0746, URL https://doi.org/10.1111/j.1365-3091.1984.tb01961.x.

Z. J. Wang, Annual Review of Fluid Mechanics **37**, 183 (2004), ISSN 0066-4189, URL https://doi.org/10.1146/annurev.fluid.36.050802.121940.

H. J. Lugt, Annual Review of Fluid Mechanics **15**, 123 (1983), ISSN 0066-4189, URL https://doi.org/10.1146/annurev.fl.15.010183.001011.

C. J. Baker, Journal of Wind Engineering and Industrial Aerodynamics **95**, 329 (2007), ISSN 0167-6105, URL https://www.sciencedirect.com/science/article/pii/S0167610506001267.

A. C. Fernandes, S. M. Sefat, F. M. Coelho, and A. S. Albuquerque, *Experimental Investigation of Flow Induced Rotation of Hinged Plates With Shapes to Avoid Fluttering* (2011), URL https://doi.org/10.1115/OMAE2011-50181.

P. Ern, F. Risso, D. Fabre, and J. Magnaudet, Annual Review of Fluid Mechanics **44**, 97 (2011), ISSN 0066-4189, URL https://doi.org/10.1146/annurev-fluid-120710-101250.

A. Filella, P. Ern, and V. Roig, Journal of Fluid Mechanics **778**, 60 (2015), ISSN 0022-1120, URL https://www.cambridge.org/core/article/oscillatory-motion-and-wake-of-a-bubble-rising-in-a-thingap-cell/DAFE5D4576FF23A7E176D75178C35DEC.

W. Zhou, M. Chrust, and J. Dušek, Journal of Fluid Mechanics **833**, 445 (2017), ISSN 0022-1120, URL https://www.cambridge.

org/core/article/path-instabilities-of-oblate-spheroids/BE656F21F9BB211707AD59C067976DF1.

G. Kirchhoff, Journal für die reine und angewandte Mathematik **1869**, 289 (1869), ISSN 0075-4102.

W. W. Willmarth, N. E. Hawk, and R. L. Harvey, The Physics of Fluids **7**, 197 (1964), ISSN 0031-9171, URL https://aip.scitation.org/doi/abs/10.1063/1.1711133.

S. B. Field, M. Klaus, M. G. Moore, and F. Nori, Nature **388**, 252 (1997), ISSN 1476-4687, URL https://doi.org/10.1038/40817.

A. Belmonte, H. Eisenberg, and E. Moses, Physical Review Letters **81**, 345 (1998), URL https://link.aps.org/doi/10.1103/PhysRevLett.81.345.

L. B. Esteban, J. S. Shrimpton, and B. Ganapathisubramani, Journal of Fluid Mechanics **883**, A58 (2020), ISSN 0022-1120, URL https://www.cambridge.org/core/article/disks-settling-in-turbulence/E94325B0428B2BBC1BCC71916157B8E0.

X. . Zhou, S. . Yuan, and G. . Zhang, Physics of Fluids **33**, 33325 (2021), ISSN 1070-6631, URL https://doi.org/10.1063/5.0045163.

C. Jin and K. Xu, Communications in Computational Physics **3**, 834 (2008).

F. Auguste, J. Magnaudet, and D. Fabre, Journal of Fluid Mechanics **719**, 388 (2013), ISSN 0022-1120, URL https://www.cambridge.org/core/article/falling-styles-of-disks/AF4C39F2CEB6C01F069C6049AC352D72.

H. Zhong, S. Chen, and C. Lee, Physics of Fluids **23**, 11702 (2011), ISSN 1070-6631, URL https://doi.org/10.1063/1.3541844.

T.-W. Pan, R. Glowinski, and G. P. Galdi, Journal of Computational and Applied Mathematics **149**, 71 (2002), ISSN 0377-0427, URL https://www.sciencedirect.com/science/article/pii/S0377042702005216.

R.-J. Wu and S.-Y. Lin, Journal of Mechanics **31**, 771 (2015), ISSN 1727-7191, URL https://www.cambridge.org/core/article/flow-of-a-falling-ellipse-numerical-method-and-classification/78742F92E9280E2B815CBB88BB8A1C2C.

N. Zorzi, J. M. C. Pereira, and J. C. F. Pereira, Theoretical and Computational Fluid Dynamics **29**, 329 (2015), ISSN 1432-2250, URL https://doi.org/10.1007/s00162-015-0360-y.

L. F. Richardson and R. T. Glazebrook, Philosophical Transactions of the Royal Society of London. Series A, Containing Papers of a Mathematical or Physical Character **210**, 307 (1911), URL https://doi.org/10.1098/rsta.1911.0009.

I. Celik, U. Ghia, P. J. Roache, C. Freitas, H. Coloman, and P. Raad, J. Fluids Eng. **130**, 78001 (2008).

L. F. Richardson, Transactions of the Royal Society of London, Series A **226**, 299 (1927).

P. J. Roache, *Validation and Verification in computational science and engineering* (Hermosa Albuquerque, NM, 1998).

T. Xing and F. Stern, Journal of Fluids Engineering **132**, 061403 (2010), ISSN 00982202.

F. Stern, R. V. Wilson, H. W. Coleman, and E. G. Paterson, Journal of Fluids Engineering, Transactions of the ASME **123**, 793 (2001), ISSN 1528901X.

Y. Wang, C. Shu, C. J. Teo, and L. M. Yang, Physics of Fluids **28**, 103603 (2016), ISSN 1070-6631, URL https://doi.org/10.1063/1.4963242.

V. K. Kushwaha and A. K. De, Physics of Fluids **32**, 103603 (2020), ISSN 1070-6631, URL https://doi.org/10.1063/5.0021794.

L. Vincent, Y. Liu, and E. Kanso, Journal of Fluid Mechanics **889**, A9 (2020), ISSN 0022-1120, URL https://www.cambridge.

org/core/article/shape-optimization-of-tumbling-wings/CFC6B85876F9F212021263EE312AD6C0.

J. C. Maxwell, Camb. Dublin Math. J., **9**, 145 (1853).

J. C. Maxwell, Camb. Dublin Math. J **9**, 145 (1854).

D. P. Riabouchinsky, The Aeronautical Journal **39**, 282 (1935), ISSN 0368-3931.

V. Mathai, X. Zhu, C. Sun, and D. Lohse, Nature Communications **9**, 1792 (2018), ISSN 2041-1723, URL https://doi.org/10.1038/s41467-018-04177-w.

L. Heisinger, P. Newton, and E. Kanso, Journal of Fluid Mechanics **742**, 243 (2014), ISSN 0022-1120, URL https://www.cambridge.org/core/article/coins-falling-in-water/0685FB1496CC8882203EE119CA39C646.

L. Mahadevan, W. S. Ryu, and A. D. T. Samuel, Physics of Fluids **11**, 1 (1998), ISSN 1070-6631, URL https://doi.org/10.1063/1.869919.

Y. Xiang, S. Qin, W. Huang, F. Wang, and H. Liu, Journal of Visualization **21**, 433 (2018), ISSN 1875-8975, URL https://doi.org/10.1007/s12650-017-0469-8.

T. Yaginuma and H. Itō, Physics of Fluids **20**, 117102 (2008), ISSN 1070-6631, URL https://doi.org/10.1063/1.2980348.

C. H. J. Veldhuis and A. Biesheuvel, International Journal of Multiphase Flow **33**, 1074 (2007), ISSN 0301-9322, URL http://www.sciencedirect.com/science/article/pii/S0301932207000699.

M. Jenny, J. Dušek, and G. Bouchet, Journal of Fluid Mechanics **508**, 201 (2004), ISSN 0022-1120, URL https://www.cambridge.org/core/article/instabilities-and-transition-of-a-sphere-falling-or-ascending-freely-in-a-newto
68B3173FDB05D467F590C1A98DF6221E.

D. Bi, Y. Wei, C. Wang, and H. Xu, Science China Technological Sciences **61**, 853 (2018), ISSN 1869-1900, URL https://doi.org/10.1007/s11431-017-9218-4.

H.-J. Zhong and C.-B. Lee, Acta Mechanica Sinica **28**, 367 (2012), ISSN 1614-3116, URL https://doi.org/10.1007/s10409-012-0036-4.

P. Ern, F. Risso, P. C. Fernandes, and J. Magnaudet, Physical Review Letters **102**, 134505 (2009), URL https://link.aps.org/doi/10.1103/PhysRevLett.102.134505.

H. Zhong, C. Lee, Z. Su, S. Chen, M. Zhou, and J. Wu, Journal of Fluid Mechanics **716**, 228 (2013), ISSN 0022-1120, URL https://www.cambridge.org/core/article/experimental-investigation-of-freely-falling-thin-disks-part-1-the-flow-structu DE84982233171E61BE1D6E788F0DC64A.

H. K. Moffatt, Journal of Fluid Mechanics **720**, 1 (2013), ISSN 0022-1120, URL https://www.cambridge.org/core/article/three-coins-in-a-fountain/A0202374F6868E2415660DA46E7AC913.

L. Blay Esteban, J. Shrimpton, and B. Ganapathisubramani, Physical Review Fluids **3**, 64302 (2018), URL https://link.aps.org/doi/10.1103/PhysRevFluids.3.064302.

E. T. Whittaker, *A treatise on the analytical dynamics of particles and rigid bodies* (CUP Archive, 1937), ISBN 0521091322.

H. Aref and S. W. Jones, Physics of Fluids A: Fluid Dynamics **5**, 3026 (1993), ISSN 0899-8213, URL https://doi.org/10.1063/1.858712.

Y. Tanabe and K. Kaneko, Physical Review Letters **73**, 1372 (1994), URL https://link.aps.org/doi/10.1103/PhysRevLett.73.1372.

M. A. Jones and M. J. Shelley, Journal of Fluid Mechanics **540**, 393 (2005), ISSN 1469-7645.

U. Pesavento and Z. J. Wang, Physical Review Letters **93**, 144501 (2004), URL https://link.aps.org/doi/10.1103/PhysRevLett.93.144501.

S. Haeri and J. Shrimpton, International Journal of Multiphase Flow **40**, 38 (2012).

M. R. Maxey and B. K. Patel, International Journal of Multiphase Flow **27**, 1603 (2001), ISSN 0301-9322, URL https://www.sciencedirect.com/science/article/pii/S0301932201000143.

D. Liu, E. E. Keaveny, M. R. Maxey, and G. E. Karniadakis, Journal of Computational Physics **228**, 3559 (2009), ISSN 0021-9991, URL https://www.sciencedirect.com/science/article/pii/S0021999109000369.

H. H. Hu, International Journal of Multiphase Flow **22**, 335 (1996), ISSN 0301-9322, URL http://www.sciencedirect.com/science/article/pii/0301932295000682.

A. A. Johnson and T. E. Tezduyar, Computer Methods in Applied Mechanics and Engineering **134**, 351 (1996), ISSN 0045-7825, URL http://www.sciencedirect.com/science/article/pii/0045782595009884.

A. A. Johnson and T. E. Tezduyar, Computational Mechanics **23**, 130 (1999), ISSN 1432-0924, URL https://doi.org/10.1007/s004660050393.

M. Uhlmann, Journal of Computational Physics **209**, 448 (2005), ISSN 0021-9991, URL http://www.sciencedirect.com/science/article/pii/S0021999105001385.

F. Fonseca and H. J. Herrmann, Physica A: Statistical Mechanics and its Applications **345**, 341 (2005), ISSN 0378-4371, URL https://www.sciencedirect.com/science/article/pii/S037843710400531X.

M. A. Jones, Journal of Fluid Mechanics **496**, 405 (2003), ISSN 0022-1120, URL https://www.cambridge.org/core/article/separated-flow-of-an-inviscid-fluid-around-a-moving-flat-plate/7B9610D4EC75061767B269A7592D970E.

Y. Wang, C. Shu, C. J. Teo, and J. Wu, Journal of Fluids and Structures **54**, 440 (2015), ISSN 0889-9746, URL http://www.sciencedirect.com/science/article/pii/S0889974614002709.

D. Kolomenskiy and K. Schneider, Theoretical and Computational Fluid Dynamics **24**, 169 (2010), ISSN 1432-2250, URL https://doi.org/10.1007/s00162-009-0171-0.

S. Michelin and S. G. Llewellyn Smith, Theoretical and Computational Fluid Dynamics **23**, 127 (2009), ISSN 1432-2250, URL https://doi.org/10.1007/s00162-009-0096-7.

A. Rana, V. K. Kushwaha, and A. K. De, Sādhanā **45**, 259 (2020), ISSN 0973-7677, URL https://doi.org/10.1007/s12046-020-01487-y.

M. Chrust, G. Bouchet, and J. Dušek, Physics of Fluids **25**, 44102 (2013), ISSN 1070-6631, URL https://doi.org/10.1063/1.4799179.

J. Dušek, M. Chrust, and G. Bouchet (Springer International Publishing, Cham, 2016), pp. 105–116, ISBN 978-3-319-27386-0.

A. R. Shenoy and C. Kleinstreuer, Journal of Fluid Mechanics **653**, 463 (2010), ISSN 0022-1120, URL https://www.cambridge.org/core/article/influence-of-aspect-ratio-on-the-dynamics-of-a-freely-moving-circular-disk/BE7AED5E320E4FF13D193D19F8057126.

T. Deloze, Y. Hoarau, and J. Dušek, European Journal of Computational Mechanics **19**, 575 (2010), ISSN 1779-7179, URL https://doi.org/10.3166/ejcm.19.575-590.

S. Alben, Physics of Fluids **22**, 61901 (2010), ISSN 1070-6631, URL https://doi.org/10.1063/1.3432128.

L. Zhu, Physics of Fluids **19**, 17113 (2007), ISSN 1070-6631, URL https://doi.org/10.1063/1.2433127.

K. Ellingsen and F. Risso, Journal of Fluid Mechanics **440**, 235 (2001), ISSN 0022-1120, URL https://www.cambridge.org/core/article/on-the-rise-of-an-ellipsoidal-bubble-in-water-oscillatory-paths-and-liquidinduc C4D609D39DD664C8FE5903AD66805B63.

P. C. Fernandes, P. Ern, F. Risso, and J. Magnaudet, Physics of Fluids **17**, 98107 (2005), ISSN 1070-6631, URL https://doi.org/10.1063/1.2061609.

P. G. Saffman, Journal of Fluid Mechanics **1**, 249 (1956), ISSN 0022-1120, URL https://www.cambridge.org/core/article/on-the-rise-of-small-air-bubbles-in-water/ABCF30732DF6006591F558C96BC3BBDC.

P. Dupleich (1949).

B. W. Skews, Journal of Fluid Mechanics **217**, 33 (1990), ISSN 0022-1120, URL https://www.cambridge.org/core/article/autorotation-of-rectangular-plates/9684B8AF3E4A3A0D81B4766C4DF3CE4E.

K. Varshney, S. Chang, and Z. J. Wang, Physical review. E, Statistical, nonlinear, and soft matter physics **87**, 53021 (2013), ISSN 1550-2376 (Electronic).

Q.-n. Li, J.-t. Qin, L.-l. Zhou, and K.-q. Chen, *Numerical Calculation of Planing Boat Resistance Based on Remesh Method* (2019), URL https://doi.org/.

S. Verma and A. Hemmati, *Performance of Overset Mesh in Modeling the Wake of Sharp-Edge Bodies* (2020).

in *Guide: Guide for the Verification and Validation of Computational Fluid Dynamics Simulations (AIAA G-077-1998(2002))* (American Institute of Aeronautics and Astronautics, Inc., 1998), AIAA Standards, URL https://doi.org/10.2514/4.472855.001.

P. Casalone, O. Dell'Edera, B. Fenu, G. Giorgi, A. Sirigu, and G. Mattiazzo, Journal of Marine Science and Engineering **8**, 394 (2020).

J. Hærvig, A. L. Jensen, M. C. Pedersen, and H. Sørensen, *Numerical and Experimental Study of the Rotational Behaviour of Flat Plates Falling Freely With Periodic Oscillating Motion* (2017), URL https://doi.org/10.1115/FEDSM2017-69503.

M. Ghoreyshi, K. Bergeron, J. Seidel, A. J. Lofthouse, and R. M. Cummings, Journal of Aircraft **53**, 1087 (2015), URL https://doi.org/10.2514/1.C033391.

T. Tezdogan, A. Incecik, and O. Turan, Ocean Engineering **123**, 131 (2016), ISSN 0029-8018, URL https://www.sciencedirect.com/science/article/pii/S0029801816302372.

V. Venkatakrishnan, Journal of Computational Physics **118**, 120 (1995), ISSN 0021-9991, URL https://www.sciencedirect.com/science/article/pii/S0021999185710844.

F. J. L. Gamboa (2010).

P. Spalart and S. Allmaras, AIAA **439** (1992).

W. P. Jones and B. E. Launder, International Journal of Heat and Mass Transfer **15**, 301 (1972), ISSN 0017-9310, URL http://www.sciencedirect.com/science/article/pii/0017931072900762.

F. R. Menter, AIAA Journal **32**, 1598 (1994), ISSN 0001-1452, URL https://doi.org/10.2514/3.12149.

S. Sarkar and B. Lakshmanan, AIAA Journal **29**, 743 (1991), ISSN 0001-1452, URL https://doi.org/10.2514/3.10649.

C. L. Rumsey and P. R. Spalart, AIAA Journal **47**, 982 (2009), ISSN 0001-1452, URL https://doi.org/10.2514/1.39947.

L. Eça and M. Hoekstra, Journal of Marine Science and Technology **13**, 328 (2008), ISSN 1437-8213, URL https://doi.org/10.1007/s00773-008-0018-1.

D. C. Wilcox, *Turbulence Modeling for CFD* (DCW Industries, La Canada, 1998).

ITTC (Madrid, Spanish, 1957).

E. Schoenherr Karl, Trans SNAME **40** (1932).

P. Martín, Ashrae Journal **41**, 20 (1999).

A. Firooz and M. Gadami (2006).

N. Sørensen, Wind Energy **12**, 715 (2008).

L. Prandtl., Tech. Rep. April 1925 (1925), URL http://ufdc.ufl.edu/AA00006233/00001.

M. Terziev, T. Tezdogan, and A. Incecik, Ships and Offshore Structures **15**, 511 (2019), ISSN 1744-5302, URL https://doi.org/10.1080/17445302.2019.1661625.

D. Wilcox, *Turbulence Modeling for CFD (Third Edition) (Hardcover)* (2006).

V. Driest, Tech. Rep. (1956).

D. C. Wilcox, AIAA Journal **46**, 2823 (2008), ISSN 0001-1452, URL https://doi.org/10.2514/1.36541.

B. Baldwin and H. Lomax, in *16th Aerospace Sciences Meeting* (American Institute of Aeronautics and Astronautics, 1978), Aerospace Sciences Meetings, URL https://doi.org/10.2514/6.1978-257.

Siemens, *Star-CCM+ User Guide version 15.02.007-R8* (2020), URL file:///opt/software/CD-adapco/15.02.007-R8/STAR-CCM+15.02.007-R8/doc/en/online/index.html#page/STARCCMP%2FGUID-71E305C9-C9FB-4DBA-9D62-68CF76480A79.html%23.

K. Hirata, K. Shimizu, K. Fukuhara, K. Yamauchi, D. Kawaguchi, and J. Funaki, Journal of Fluid Science and Technology **4**, 168 (2009).

C. J. Freitas, Applied Mathematical Modelling **26**, 237 (2002), ISSN 0307-904X, URL http://www.sciencedirect.com/science/article/pii/S0307904X01000580.

S. J. Kline, H. K. Moffatt, and M. V. Morkovin, Journal of Fluid Mechanics **36**, 481 (1969), ISSN 0022-1120, URL https://www.cambridge.org/core/article/report-on-the-afosrifpstanford-conference-on-computation-of-turbulent-boundary-2064A3FAED63D6F892C1A9B90155224A.

P. J. Roache, K. N. Ghia, and F. M. White, Journal of Fluids Engineering **108**, 2 (1986), ISSN 0098-2202, URL https://doi.org/10.1115/1.3242537.

L. Eca and M. Hoekstra, Journal of Computational Physics **262**, 104 (2014), ISSN 00219991.

T. Phillips and C. J. Roy, Journal of Verification, Validation and Uncertainty Quantification **1**, 041006 (2017), ISSN 2377-2158.

M. Terziev, T. Tezdogan, and A. Incecik, Ocean Engineering **208**, 107434 (2020), ISSN 0029-8018.

T. Phillips and C. J. Roy, 49th AIAA Aerospace Sciences Meeting including the New Horizons Forum and Aerospace Exposition **Orlando, F**, 1 (2012).

J. Cadafalch, C. D. Pérez-Segarra, R. Cònsul, and A. Oliva, Journal of Fluids Engineering, Transactions of the ASME **124**, 11 (2002), ISSN 00982202.

V. Mathai, X. Zhu, C. Sun, and D. Lohse, Physical Review Letters **119**, 54501 (2017), URL https://link.aps.org/doi/10.1103/PhysRevLett.119.054501.

M. Horowitz and C. H. K. Williamson, Physics of Fluids **20**, 101701 (2008), ISSN 1070-6631, URL https://doi.org/10.1063/1.2992126.

M. Chrust, G. Bouchet, and J. A. N. Dušek, Journal of Fluid Mechanics **665**, 199 (2010), ISSN 0022-1120, URL https://www.cambridge.org/core/article/parametric-study-of-the-transition-in-the-wake-of-oblate-spheroids-and-flat-cyl E0F973F6F8228B27C11AAD85A0CF18B2.

M. Chrust, Phd thesis, Université de Strasbourg (2012).

J. Fokken, B. Krohn, R. Kapulla, B. Niceno, H.-M. Prasser, and A. Badillo, *NEA Benchmark Exercise: Computational Fluid Dynamic Prediction and Uncertainty Quantification of a GEMIX Mixing Layer Test* (2019).

D. Groen, H. Arabnejad, V. Jancauskas, W. N. Edeling, F. Jansson, R. A. Richardson, J. Lakhlili, L. Veen, B. Bosak, P. Kopta, et al., Philosophical Transactions of the Royal Society A: Mathematical, Physical and Engineering Sciences **379**, 20200221 (2021), URL https://doi.org/10.1098/rsta.2020.0221.

C. J. Roy and W. L. Oberkampf, Computer Methods in Applied Mechanics and Engineering **200**, 2131 (2011), ISSN 0045-7825, URL https://www.sciencedirect.com/science/article/pii/S0045782511001290.

S. Salvadori (Springer International Publishing, Cham, 2019), pp. 33–66, ISBN 978-3-319-92943-9, URL https://doi.org/10.1007/978-3-319-92943-9_2.

A. Baker, R. Kelso, E. Gordon, S. Roy, and E. G. Schaub, Ashrae Journal **39**, 51 (1997).

Q. Chen and J. Srebric, HVACR Research **8**, 201 (2002), ISSN 1078-9669, URL https://www.tandfonline.com/doi/abs/10.1080/10789669.2002.10391437.

L. E. Schwer (2009).

R. Procedures, in *Proceedings of the 25th International Towing Tank Conference (ITTC), Fukuoka, Japan* (2008), pp. 14–20.

K. M. Almohammadi, D. B. Ingham, L. Ma, and M. Pourkashan, Energy **58**, 483 (2013), ISSN 0360-5442, URL https://www.sciencedirect.com/science/article/pii/S0360544213005100.

H. Wan, H. Dong, and Z. Liang, in *50th AIAA Aerospace Sciences Meeting including the New Horizons Forum and Aerospace Exposition* (American Institute of Aeronautics and Astronautics, 2012), Aerospace Sciences Meetings, URL https://doi.org/10.2514/6.2012-1079.